=========== **MECHANICS** ===========

# Evolution of a Shock Wave in a Clustered Gas–Liquid Medium

## Academician V. E. Nakoryakov and V. E. Dontsov*

### Received October 3, 2003

Propagation of shock waves in a bubble liquid has been investigated in detail both theoretically and experimentally [1–4]. It has been shown that oscillating shock waves are generated in the bubble liquid, and both the evolution and structure of these waves have been studied in detail. The effect of both heterogeneity of a gas–liquid mixture and liquid compressibility on the structure of a pressure wave was investigated in [5, 6]. The structure and attenuation of moderate-amplitude pressure waves both in a liquid containing bubbles of two different gases and in stratified bubble media were studied experimentally in [7, 8]. Generation of high-power pressure pulses by spherical bubble clusters was investigated numerically in [9]. Interaction of a plane shock wave with a spherical bubble cluster in a liquid was studied experimentally in [10].

This paper concerns experimental investigation of the evolution and structure of a moderate-amplitude shock wave in a liquid containing spherical bubble clusters.

The experiments were carried out in a shock tube [10]. Its working section was a vertical thick-walled steel tube with an inner diameter of 53 mm and a length of 1 m. A thin stainless-steel wire (1 mm in diameter) was stretched along the working-section axis. The working section was partially filled with a liquid (distilled water) under vacuum conditions, which prevented the appearance of bubbles in the liquid. Water in the working section was saturated with air until equilibrium at room temperature and atmospheric static pressure. Five bubble clusters (foam-rubber balls 30 mm in diameter filled with a bubble liquid) were put on the wire through their centers. The upper end of the upper cluster was situated in the liquid at a depth of 10 mm. The centers of the other clusters were situated exactly opposite the corresponding pressure sensors $D2$–$D5$. The $D1$ sensor measured the profile of an air shock wave entering the medium. The method of preparing

the bubble clusters was described in [10]. Air bubbles in the clusters were 0.1–0.5 mm in diameter [10].

Step-shaped pressure waves were generated in air by breaking a diaphragm, which separated a high-pressure chamber and the working section, and then propagated into the liquid. Pressure-wave profiles were measured by piezoelectric pressure sensors ($D1$–$D5$). Signals generated by the sensors were transmitted to a digitizer and then processed on a computer.

Figure 1 shows the time profiles of pressure waves at different distances $X$ from the entry of the shock wave into the medium. Here, $\Delta P_0$ is the amplitude of the shock wave entering the medium, which is equal to the amplitude of the air shock wave reflected from the liquid surface (Fig. 1, $X < 0$). In addition, $\Delta P_m$ is the amplitude of the first pressure-wave oscillation in the liquid, and $P_0$ is the initial static pressure in the medium. Amplitudes of the waves and the time scale are shown above and below the profiles, respectively. One can see that the initial step-shaped wave has already been transformed into an oscillating shock wave at the second bubble cluster (Fig. 1, $X = 0.105$ m). As in a homogeneous bubble mixture [3], the amplitude of the first oscillation is as large as one and a half times the mean pressure in a small-amplitude wave. In Fig. 1 ($X = 0.205$ and $0.305$ m), the shape of the first oscillation of the shock wave (line *1*) is compared with the shape of the same-amplitude soliton (line *2*) calculated from the Boussinesq equation for the gas–liquid medium. This soliton is described by the relations [3]

$$\Delta P(t) = \Delta P_m \mathrm{sec}h^2 \frac{t}{\Delta t_B}, \quad \Delta t_B = \frac{6\beta}{B\Delta P_m}; \qquad (1)$$

where $\Delta t_B$ is the half-width of the calculated soliton, while $\beta$ and $B$ are coefficients of dispersion and nonlinearity, respectively. If the gas–liquid medium has a cluster structure and the gas temperature in the bubbles is constant, these coefficients are expressed as [11]

$$\beta = R^2 \left( 1 + \frac{0.2(1 - \varphi_c)}{3\varphi_0(1 - \varphi_0\varphi_c)} \right),$$

$$B = \frac{1 - \varphi_0\varphi_c}{(\rho_1(1 - \varphi_0) + \rho_2\varphi_0)\varphi_0\varphi_c}.$$

*Kutateladze Institute of Thermal Physics,*
*Siberian Division, Russian Academy of Sciences,*
*pr. Akademika Lavrent'eva 1, Novosibirsk, 630090 Russia*
* *e-mail: dontsov@itp.nsc.ru*

$\Delta P_0 = 0.037$ MPa

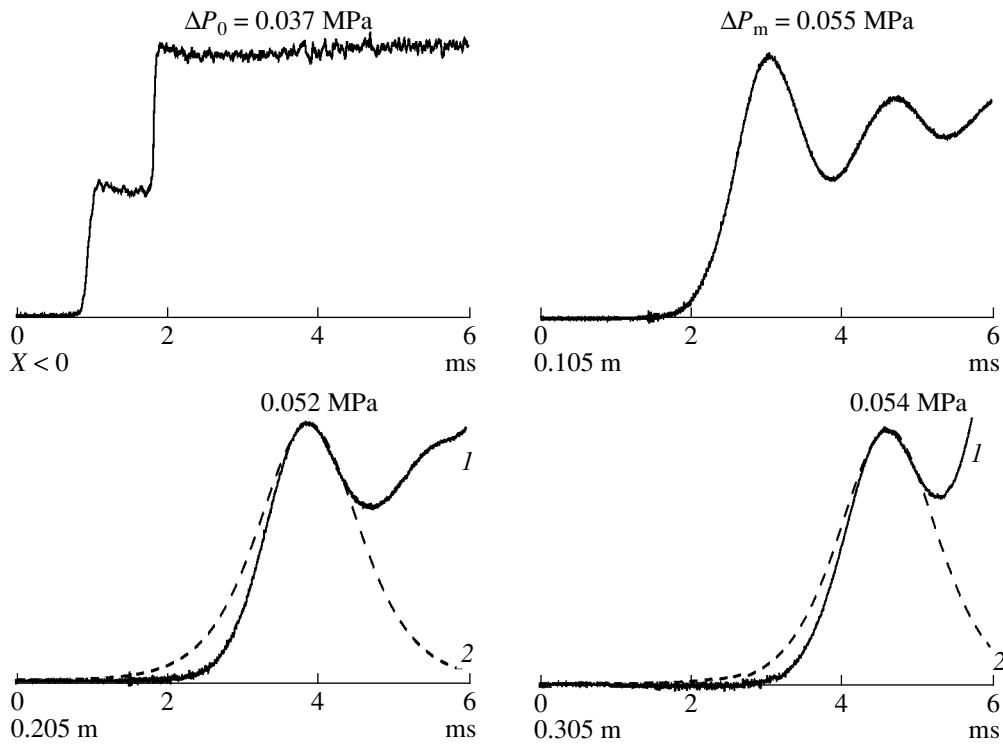$\Delta P_{\mathrm{m}} = 0.055$ MPa

0.052 MPa

0.054 MPa

**Fig. 1.** Evolution of a shock wave in a clustered gas–liquid medium according to (*1*) experimental data and (*2*) calculations by relations (1) for $P_0 = 0.101$ MPa, $\varphi_0 = 7.5\%$, and $\varphi_{\mathrm{c}} = 9.8\%$.

Here, $\varphi_{\mathrm{c}}$ is the volume fraction of the gas bubbles in a cluster, $\varphi_0$ is the volume fraction of clusters in the medium, $R$ is the cluster radius, and $\rho_1$ and $\rho_2$ are the densities of the liquid and gas, respectively.

In contrast to a homogeneous bubble medium, dispersion in a clustered gas–liquid medium is determined by both the cluster radius $R$ and volume fraction $\varphi_0$ of clusters in the medium [11]. As in homogeneous bubble media [3], the shape of the first oscillation of a small-amplitude shock wave is close to the shape of soliton (1). The difference between the experimental profile and calculated soliton shape can be attributed to two causes. First, the formation of the oscillating shock wave is possibly not completed at the distances under consideration. Second, the long-wave approximation for the Boussinesq equation describing gas–liquid media is violated under the experimental conditions. Indeed, this approximation requires that the wavelength must be much longer than both the cluster dimension and distance between the clusters.

The duration of oscillations in the oscillating shock wave decreases with both a decrease in the initial gas volume fraction in a cluster and an increase in the amplitude of a wave entering the medium. At the same time, the duration of oscillations in a homogeneous bubble medium is independent of the gas volume fraction and determined only by the bubble dimension and wave amplitude [3]. The formation of a precursor ahead

of the main signal represents a characteristic feature of large-amplitude waves. Apparently, the precursor is formed by high-frequency pulsations, which are generated by nonlinear cluster vibrations in a liquid and whose velocities are higher than that of the main wave.

The velocity of a shock wave in the clustered gas–liquid medium was measured as a function of the wave amplitude. This velocity was determined by using arrival times of the first-oscillation peak at two neighboring sensors ($D3$ and $D4$) and the distance between them. It is shown that the isothermal approximation for the velocity of a shock wave in a homogeneous bubble medium [3] agrees well with the experimental data. Indeed, the duration of the leading edge of an oscillating shock wave is much longer than the estimate $\tau_0 = \dfrac{d^2}{4\pi^2 a}$ [4] for the gas thermal relaxation time, where $a$ is the thermal diffusivity of the gas in bubbles. Consequently, the behavior of the gas in bubbles at the leading edge of the wave is close to isothermal.

Open circles and crosses in Fig. 2 show the amplitude dependence of the half-width measured for the first oscillation of the shock wave propagating in a clustered gas–liquid medium for different medium parameters.

Similar to the Boussinesq soliton, this half-width is determined as the wave duration from $0.42\Delta P_m$ to the first-oscillation pressure maximum $\Delta P_m$. The wave half-width was measured only by the sensors situated opposite the third and fourth clusters with respect to the wave entry into the medium, i.e., when the oscillating shock wave was virtually formed. Curves *2* and *5* show the soliton half-widths calculated by Eqs. (1). Both for small wave amplitudes $\left(\dfrac{\Delta P_m}{P_0} \leq 1\right)$ and for homogeneous bubble media, calculation by Eqs. (1) agrees with experimental data obtained for the corresponding parameters of the medium (open circles and curve *2*, crosses and curve *5*). As was noted above, the difference between experimental and calculated data is attributed to both unsteady wave behavior and violation of the long-wave approximation in the experiments.

As was shown in [12], the half-width of solitary waves with an amplitude of $\dfrac{\Delta P_m}{P_0} \geq 5$ in a homogeneous bubble medium is close to $0.5\Delta t_B$. The experimental points for the amplitude $\dfrac{\Delta P_m}{P_0} \geq 5$ (open circles in Fig. 2) also agree well with calculated line *3* ($\Delta t = 0.5\Delta t_B$). For comparison, experimental data [10] for the half-width of a solitary wave formed in a liquid by a single cluster with the same dimension are shown by solid circles in Fig. 2. One can see that the duration of the first oscillation of the shock wave in the clustered gas–liquid medium (open circles) is equal to the duration of the solitary wave formed by the single cluster in the liquid (solid circles) for the same parameters of the medium and wave.

As is known, in a homogeneous bubble liquid, pressure oscillations in an oscillating shock wave are damped behind its leading edge [3] due to dissipative losses in the medium. Figure 3 shows the structure of the moderate-amplitude oscillating shock wave in a clustered gas–liquid medium. Instead of damped oscillations, an increase in the amplitude of pressure oscillations is observed behind the leading edge of this wave. This effect can be caused by "resonant" cluster vibrations in the liquid. Indeed, at definite parameters of the medium and wave, three neighboring clusters oscillate, so that two extreme clusters are in phase with each other and in antiphase with the middle cluster. As a result, the amplitude of pulsations of the middle cluster and, consequently, the amplitude of shock-wave oscillations increase.

Thus, the velocity and structure of moderate-amplitude shock waves in a liquid containing spherical bubble clusters have been measured and compared with the corresponding theoretical results. The Boussinesq equation has been shown to adequately describe the
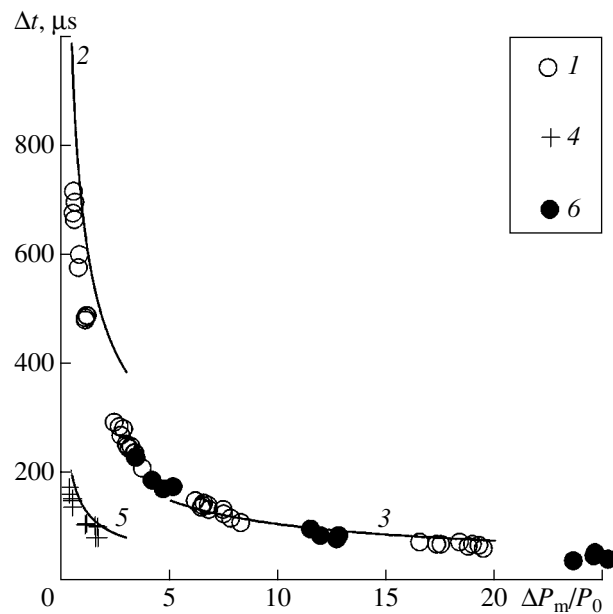


**Fig. 2.** Amplitude dependence of the half-width of the pressure wave: the experimental data for (open circles) $\varphi_0 = 7.5\%$ and $\varphi_c = (8.4\text{–}9.8)\%$, (crosses) $\varphi_0 = 7.5\%$ and $\varphi_c = 0.38\%$, and (solid circles) a single cluster with $\varphi_c = 12\%$; the calculations by relations (1) for $\varphi_c = (1)$ 9.1 and (3) 0.38% and (2) by the formula $\Delta t = 0.5\Delta t_B$.
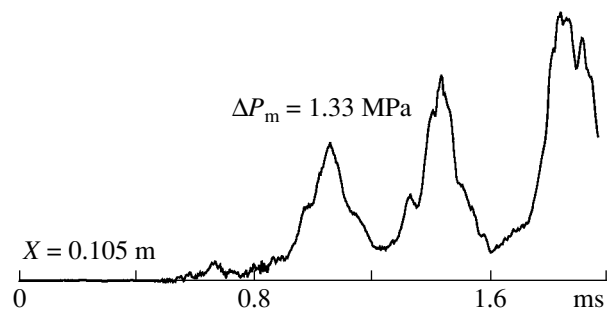


**Fig. 3.** Structure of a moderate-amplitude oscillating shock wave in a clustered gas–liquid medium for $\varphi_0 = 11.3\%$, $\varphi_c = 10.8\%$, and $\Delta P_0 = 0.81$ MPa.

structure of the leading edge of a small-amplitude oscillating shock wave. It has been found that the resonant interaction between bubble clusters in the shock wave can increase the amplitude of oscillations.

## ACKNOWLEDGMENTS

## REFERENCES

1. G. K. Batchelor, Mechanik **109** (3), 67 (1968).

2. L. van Wijngaarden, J. Fluid Mech. **33**, 465 (1968).

3. V. E. Nakoryakov, B. G. Pokusaev, and I. R. Shreĭber, *Wave Dynamics of Gas– and Vapor–Liquid Media* (Énergoatomizdat, Moscow, 1990).

4. R. I. Nigmatulin, *Dynamics of Multiphase Media* (Nauka, Moscow, 1987), Vol. 2.

5. A. E. Beylich and A. Gulhan, Phys. Fluids A **2**, 1412 (1990).

6. M. Kameda, N. Shimaura, F. Higashino, and Y. Matsumoto, Phys. Fluids **10**, 2661 (1998).

7. V. E. Nakoryakov and V. E. Dontsov, Dokl. Akad. Nauk **382**, 637 (2002) [Dokl. Phys. **47**, 153 (2002)].

8. V. E. Nakoryakov and V. E. Dontsov, Dokl. Akad. Nauk **386**, 48 (2002) [Dokl. Phys. **47**, 682 (2002)].

9. V. K. Kedrinskiĭ, Yu. I. Shokin, V. A. Vshivkov, *et al.*, Dokl. Akad. Nauk **381**, 773 (2001) [Dokl. Phys. **46**, 856 (2001)].

10. V. E. Nakoryakov and V. E. Dontsov, Dokl. Akad. Nauk **391**, 199 (2003) [Dokl. Phys. **48**, 368 (2003)].

11. S. I. Lezhnin, Doctoral Dissertation (Inst. Teplofiz. Sib. Otd. Ross. Akad. Nauk, Novosibirsk, 1994).

12. V. E. Nakoryakov, V. E. Kuznetsov, V. E. Dontsov, and P. G. Markov, Int. J. Multiphase Flow **16**, 741 (1990).

*Translated by Yu. Verevochkin*

=========================== **MECHANICS** ===========================

# Velocity-Nonequilibrium Effect in the Ignition of Coal Dust Suspended in a Gas in Shock and Detonation Waves

## A. V. Fedorov*, Corresponding Member of the RAS V. M. Fomin, and T. A. Khmel'**

We develop a mathematical model of a detonation flow of coal particles suspended in oxygen which takes into account the difference of temperatures and velocities in different phases, nonequilibrium devolatilization, and homogeneous and heterogeneous reactions of ignition and combustion. The model is verified by experimental data on both the steady-state detonation velocity as a function of the concentration of suspended particles and the delay time of particle ignition as a function of the Mach number of a passing shock wave. The ignition of bituminized coal in shock waves is analyzed in this model. It is shown that the ignition stage proceeds completely under the conditions of both temperature and velocity nonequilibrium in the mixture. We reveal the considerable effect of heating of particles due to deceleration temperature, which determines the dynamics of devolatilization and, therefore, ignition delay time. Calculation of flow structures behind shock and detonation waves is exemplified.

## INTRODUCTION

Study of shock wave processes in a gas with suspended coal dust is of both theoretical and practical interest in connection with the catastrophic consequences of explosion and detonation phenomena in coal mines. As was experimentally shown in [1], heterogeneous detonation waves can be initiated and propagate in mixtures of coal dust with air and oxygen. The mechanics of heterogeneous media including devolatilization and oxidation of volatiles and combustion of a coke residue was theoretically analyzed in [2] in the one-velocity two-temperature approximation. That analysis agrees with experimental data [1] on the dependence of the detonation velocity on the initial concentration of coal particles in a mixture. Analysis of nonequilibrium processes in steady-state detonation waves reveals a large difference between the characteristic times of pyrolysis and the combustion of volatiles, the thermal relaxation of phases, and surface combustion of particles. At the same time, devolatilization duration is comparable with the characteristic time of velocity relaxation.

To obtain detonation initiation criteria, it is necessary to correctly take into account ignition conditions for particles. In high-velocity gas flows behind detonation waves, these conditions differ from both static conditions of slow heating and conditions behind reflected shock waves. Experimental ignition delay times of coal dust particles 50–70 μm in size in passing shock waves [3] show that the ignition delay stage proceeds completely in the velocity-nonequilibrium mixture. Blowing of a particle by a flow affects the thermal dynamics of the particle due to both intensification of convective heat transfer (increase in the Nusselt number) and an increase in gas temperature in the boundary layer of the particle when the flow is decelerated. On the other hand, emitted volatiles under blowing burn beyond a "reduced" film adjacent to the particle [4]. Therefore, the heat flux from combustion of volatiles to the particle decreases, and combustion products are carried away by the flow and do not impede the inflow of an oxidant to the particle surface. A strong decrease in experimental ignition delay times in coal dust clouds (1–40 μm) in passing shock waves with respect to ignition in reflected shock waves was observed in [5].

To investigate the fine detonation structure of gases with suspended coal dust, including factors determining ignition, a semiempirical physical–mathematical model is developed by using the two-velocity two-temperature approximation of the mechanics of heterogeneous media.

---

*Institute of Theoretical and Applied Mechanics, Siberian Division, Russian Academy of Sciences, ul. Institutskaya 4/1, Novosibirsk, 630090 Russia*
* *e-mail: fedorov@itam.nsc.ru*
** *e-mail: khmel@itam.nsc.ru*

## CONSISTENT PHYSICAL–MATHEMATICAL MODEL OF THE IGNITION AND DETONATION OF COAL DUST SUSPENDED IN A GAS

Basic equations describing the flow behind the front of a stationary shock wave in the comoving coordinate

system are as follows. The expressions of conservation laws have the form

$$\rho_1 u_1 + (\rho_2 + \rho_3) u_2 = C_1,$$
$$p + \rho_1 u_1^2 + (\rho_2 + \rho_3) u_2^2 = C_2, \qquad (1)$$
$$E_1 \rho_1 u_1 + p u_1 + E_2 \rho_2 u_2 + E_3 \rho_3 u_2 = C_3,$$

where subscripts 1, 2, and 3 correspond to the gas, solid volatiles bound in the particle, and coke component of the particle, respectively; and the constants $C_1$, $C_2$, and $C_3$ are determined from the initial state of the mixture and front velocity $u_0$, which is specified for the shock wave or is determined for Chapman–Jouguet detonation by a procedure described in [2]. Master equations and equation of particle heat transfer have the form

$$\frac{d\rho_2 u_2}{dx} = -J_2, \quad \frac{d\rho_3 u_2}{dx} = -J_3, \quad (\rho_2 + \rho_3) u_2 \frac{du_2}{dx} = f,$$

$$(\rho_2 c_2 + \rho_3 c_3) u_2 \frac{dT_2}{dx} = q + (1 - \vartheta_3) J_3 Q_3 \qquad (2)$$

$$- J_2 Q_{Dev} + (1 - \vartheta_2) \xi_{12}^* J_2 Q_{12},$$

where $J_2$ and $J_3$ characterizing change in the masses of components are different at the ignition and combustion stages; $Q_{Dev}$, $Q_2$, and $Q_3$ are the heats of pyrolysis, combustion of volatiles, and coke combustion, respectively; and $\vartheta_1$ and $\vartheta_2$ are the accommodation coefficients. The equation of state has the form

$$E_1 = \frac{u_1^2}{2} + e_1, \quad E_2 = \frac{u_2^2}{2} + c_2 T_2 + \xi_{12}^* Q_{12} - Q_{Dev},$$

$$E_3 = \frac{u_2^2}{2} + c_3 T_2 + Q_3, \qquad (3)$$

$$p = \rho_{11} (\gamma - 1) e_1, \quad \gamma = \gamma(e_1), \quad T_1 = \frac{(\gamma - 1) e_1}{R}.$$

Finally, closing relations have the form

$$f = \frac{3 m_2 \rho_{11}}{4d} c_D |u_1 - u_2| (u_1 - u_2),$$

$$q = \frac{6 m_2 \lambda_1}{d^2} \mathrm{Nu} (T_d - T_2),$$

$$c_D(\mathrm{Re}, \mathrm{M}_{12}) = \left(1 + \exp\left(-\frac{0.43}{M_{12}^{4.67}}\right)\right)\left(0.38 + \frac{24}{\mathrm{Re}} + \frac{4}{\sqrt{\mathrm{Re}}}\right),$$

$$\mathrm{Re} = \frac{\rho_{11} d |u_1 - u_2|}{\mu}, \qquad (4)$$

$$\mathrm{M}_{12} = \frac{|u_1 - u_2| \sqrt{\rho_{11}}}{\sqrt{\gamma p}}, \quad \rho_{11} = \frac{\rho_1}{1 - m_2}, \quad m_2 = \frac{\rho_2 + \rho_3}{\rho_{23}},$$

$$\mathrm{Nu} = 2 + 0.6 \mathrm{Re}^{1/2} \mathrm{Pr}^{1/3},$$

$$T_d = T_1 [1 + 0.5 \mathrm{Pr}^{1/3} (\gamma - 1) \mathrm{M}_{12}^2].$$

These equations represent a generalization of the model proposed in [2], which involves the minimum number of chemical reactions, and are written in the same notation. A more detailed model of the combustion of coal dust in shock and detonation waves was developed in [6]. Analysis of the data in [7] and conclusions in [2] shows that the presence of combustible volatiles in the gas can be disregarded. In Eqs. (4), $T_d$ is the temperature of flow deceleration in the boundary layer on the particle surface [8]. The thermodynamic properties of the gas mixture behind the shock wave are assumed to be similar to those of the original gas. The concentration of gaseous volatiles consisting primarily of combustible hydrocarbons is very low, and determining components are oxygen, carbon oxide, carbon dioxide, and a small amount of water vapor. Since the molecular weight of the mixture with the content $\xi_{O_2} = \alpha$, $\xi_{CO_2} = 0.5(1 - \alpha)$, $\xi_{CO} = 0.4(1 - \alpha)$, and $\xi_{H_2O} = 0.1(1 - \alpha)$ $(0 < \alpha < 1)$ coincides with the molecular weight of oxygen, and the specific heats of the components are close to each other in a wide temperature range, the thermodynamic properties of this mixture are close to those of oxygen. In the equation of state of the gas, change in $\gamma$ on the shock wave is taken into account in a form similar to [9]:

$$\gamma = \begin{cases} \gamma_0 - \alpha_1 \left(\dfrac{e_1}{e_*}\right)^\beta, & e_1 \le e_* \\[2ex] \gamma_\infty + (\gamma_* - \gamma_\infty) \exp\left(\alpha_2 \left(1 - \dfrac{e_1}{e_*}\right)\right), & e_1 > e_* \end{cases} \qquad (5)$$

where constants $e_* = 0.7$ MJ/kg, $\gamma_0 = 1.41$, $\gamma_\infty = 1.234$, $\gamma_* = 1.32$, $\alpha_1 = 0.09$, $\alpha_2 = 0.32$, and $\beta = 1.5$ were determined for oxygen in [2]. The temperature dependence of gas thermal conductivity $\lambda_1(T) = \lambda_1(300) \left(\dfrac{T}{300}\right)^{0.5}$ is taken into account.

The initial conditions for the system of Eqs. (1)–(4) correspond to the state on the frozen shock wave, which is determined from Eqs. (1) under the conditions

$$\rho_2 = \rho_{20}, \quad \rho_{12} = 0, \quad \rho_3 = \rho_{30},$$
$$u_2 = u_0, \text{ and } T_2 = T_0.$$

Similarly, the final equilibrium detonation state is determined from Eqs. (1) under the conditions $\rho_{12} = 0$, $\rho_2 = 0$, $\rho_3 = \rho_k$, $u_2 = u_1$, and $T_2 = T_1$.

Relations for $J_2$ and $J_3$ represent the devolatilization and combustion of coke residue. At the combustion stage, we take $J_2 = \tilde{J}_2(T_2)$, $J_3 = \tilde{J}_3(T_2)$, $\theta_2 = 1$, and $\theta_3 = 0.5$. The following master equation of devolatilization

from dusted bituminized coal (Pittsburgh bed) under fast heating [10] is used for $\tilde{J}_2$:

$$\tilde{J}_2(T) = \rho_2\left(\frac{1}{\tau_{21}}\exp\left(-\frac{E_{a21}}{RT}\right) + \frac{1}{\tau_{22}}\exp\left(-\frac{E_{a22}}{RT}\right)\right),$$

Surface combustion is described by the following Arrhenius-type equation for $\tilde{J}_3$ with allowance for incomplete combustion attributed both to the presence of incombustible slag (ash) and to deficit in oxidant for coal dust concentrations exceeding the stoichiometric limit [2]:

$$\tilde{J}_3(T) = \frac{\rho_3 - \rho_k}{\tau_3}\exp\left(-\frac{E_{a3}}{RT}\right).$$

According to the data in [3], ignition delay times for 50-$\mu$m coal particles in passing shock waves are comparable to the characteristic time of particle heating even under blowing. Taking into account temperature inhomogeneity, Sichel *et al.* [3] attained agreement between experimental and calculation data on ignition delay for a single particle. The step temperature distribution over the particle is taken as an approximation in the two-temperature mechanics of heterogeneous media. It is accepted that the thin surface layer of the particle has temperature $T_f$, whereas the remaining particle volume has temperature $T_2$. Then, at the ignition stage, we have

$$
\begin{aligned}
J_2 &= k_f\tilde{J}_2(T_f) + (1 - k_f)\tilde{J}_2(T_2), \\
J_3 &= k_{\text{por}}k_f\tilde{J}_3(T_f) + (1 - k_f)\tilde{J}_3(T_2),
\end{aligned}
\tag{6}
$$

where $k_f$ is the relative mass of the layer and $k_{\text{por}}$ is the coefficient representing particle porosity. The coefficient $k_f$ is determined by fitting calculations to experimental data on ignition delay. According to the assumption that heat in carbon oxidation in pores is released in the particle, and heat in the oxidation of volatiles is equally divided between the particle and gas, we take $\theta_2 = 0.5$ and $\theta_3 = 0$ at the ignition stage.

## ANALYSIS OF IGNITION
## IN A BITUMINIZED COAL SUSPENDED GAS

Calculations were carried out for 50-$\mu$m coal particles, where the concentrations of volatiles and ash were equal to 32 and 10%, respectively, according to experiments [1]. Similar particles belonging to bituminized coals of the Pittsburgh bed both in size (53–74 $\mu$m) and in the content of volatiles were considered in [3]. Reaction constants were taken in accordance with the data in [11–13] for the given coal type.

Experimental data [3] are represented as the ignition delay time for coal particles after the passage of the shock-wave front as a function of the Mach number of
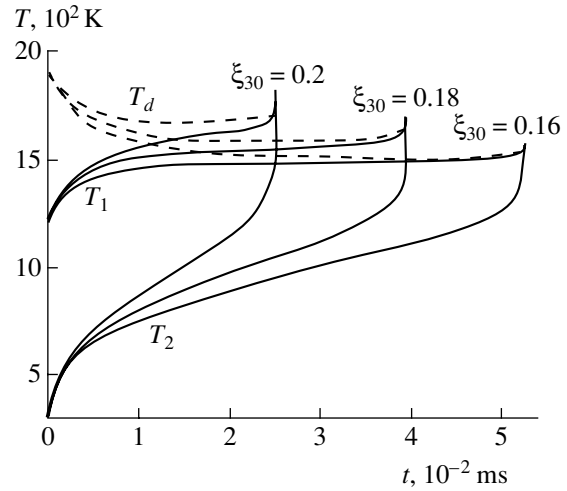
**Fig. 1.** Temperature characteristics of the ignition stage.

the shock wave $M_0$ and gas temperature on the front. The velocity of the shock-wave front is measured, and temperature is determined from the known relations on the shock jump [the same values are obtained from Eqs. (1), (3) for $\rho_{30} = 0$ and $\gamma = 1.4$]. Calculation is carried out with the inclusion of Eq. (5) and $T_f = T_d$ from Eqs. (4). The approximation

$$k_f(T_1^*) = 1.948 \times 10^{-8}\exp\left(\frac{19\,203}{T_1^*}\right),$$

where $T_1^*$ ($M_0$) is the maximum gas temperature in the velocity relaxation zone for a given Mach number in the absence of combustion, provides agreement with experimental dependence of the ignition delay time on the Mach number in [3] for $\xi_{30} = 0.2$.

The particle-concentration effect on heating dynamics for $M_0 = 4.58$ ($u_0 = 1.511$ km/s) is seen in Fig. 1, where the solid and dashed lines are the time dependence of the phase temperature and deceleration temperature, respectively. It is seen that an increase in $T_2$ during the first microseconds after the front passage is attributed to convective heat transfer determined by high $T_d$ value. In the velocity-relaxation process, gas temperature beyond the boundary layer approaches deceleration temperature. With an increase in the particle concentration, an increase in $T_1$ due to heat released in deceleration of particles in the flow becomes more pronounced and a decrease in deceleration temperature becomes less pronounced. It is seen that, in this model, thermal equilibrium in the particle breaks, which gives rise to the unlimited increase in temperature.

Figure 2 shows both calculations of ignition delays for various particle concentration and experimental data of [3]. We note that the results are well approxi-
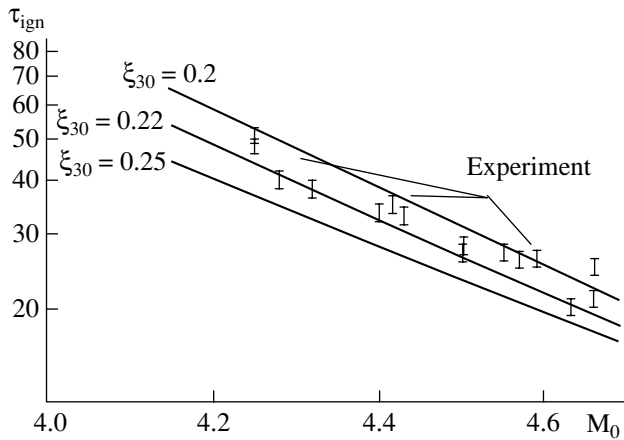
**Fig. 2.** Ignition delay time for various shock wave amplitudes and particle concentrations. Points with error bars are experimental data.

model is based on analysis of the dynamics of the parameters of the two-phase mixture. As is seen in Fig. 3a, the gas pressure distribution has the maximum point, after which pressure drop, along with an unlimited increase in temperature, is accompanied by the acceleration of devolatilization and, correspondingly, combustion of volatiles. The interval from the maximum pressure point to the limiting time of the existence of a solution in the ignition model is small (5% of the total ignition delay time). In view of this, when describing the dynamics of coal dust suspended in the gas in shock and detonation waves, the maximum pressure point will be conventionally treated as the point of thermal equilibrium breaking or the point of transition from the ignition stage to the combustion stage.

## DETONATION WAVES IN A GAS WITH SUSPENDED COAL PARTICLES

Propagation of steady-state detonation waves is characterized by a certain dependence of the detonation velocity on the mixture composition (initial particle concentration). For coal dust suspended in oxygen, this dependence was experimentally obtained in [1] (including bituminized coal with 32% of volatiles and 53–74-μm size of particles) and was used in [2] to verify the model. Figure 4 shows the experimental data for the detonation velocity as a function of the coal concentration and corresponding calculations for (solid line) 50- and (dashed line) 25-μm particles and $\lambda^* = \dfrac{\rho_{30} + \rho_{20}}{\rho_{10}}$. For the Chapman–Jouguet regime, the final state is sonic with respect to the equilibrium speed of sound. The frozen speed of sound (velocity of propagation of small perturbations in the gas phase) and the speed of sound that is equilibrium in velocity and frozen in temperature, which is equal to the frozen speed of sound in the one-velocity model, are also determined
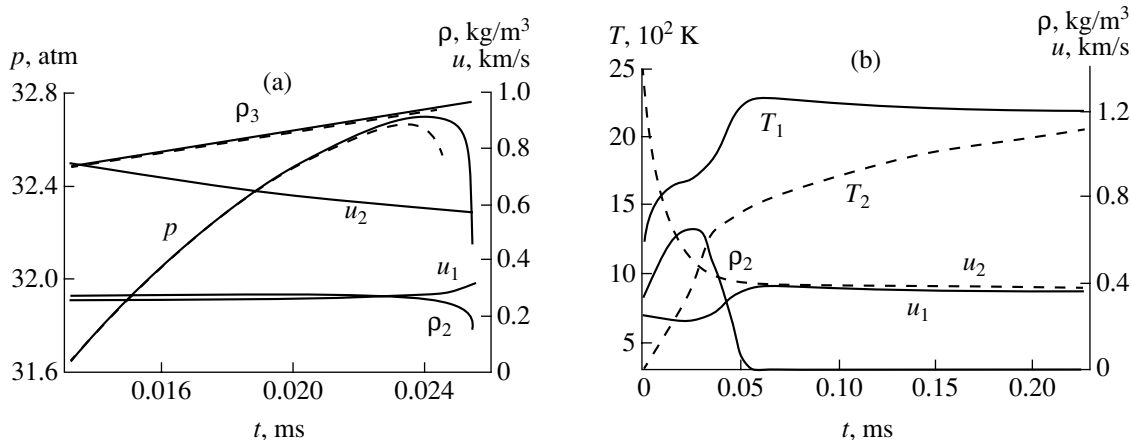
mated by straight lines in the semilogarithmic scale, which presents the Arrhenius character of processes determining the ignition stage.

Figure 3a shows the time dependences of the parameters behind the shock wave ($M_0 = 4.58$) in the mixture with concentration $\xi_{30} = 0.2$, where a considerable difference between $u_1$ and $u_2$ at the ignition stage is seen. Variation of the parameter $k_{por}$ from (solid lines) 1 to (dashed lines) 3600 [3] shows that porosity only slightly affects the ignition delay time. Therefore, coke oxidation plays a minor role in the ignition process. According to the classification in [14], bituminized coal is characterized by a mixed (homogeneous–heterogeneous) ignition type, where the dynamics of devolatilization and combustion of volatiles determines the breakdown of thermal equilibrium in the particle.

The determination of the point of breakdown and onset of ignition is an important problem in the theory of combustion and detonation. A criterion taken in this



**Fig. 3.** Flow structure at the ignition stage (a) behind the passing shock wave and (b) at the onset of combustion in the detonation wave.
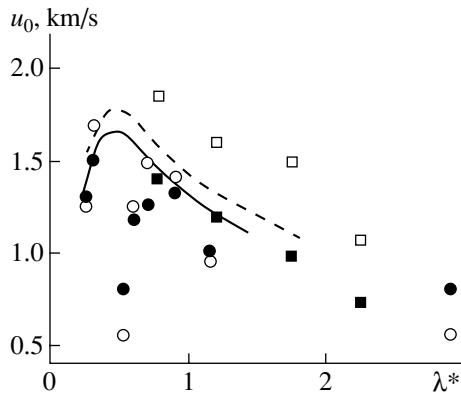
**Fig. 4.** Detonation velocity measured as a function of the coal concentration for (circles) 54- and (squares) 25-μm particles. Corresponding calculations for 50- and 25-μm particles are shown by the solid and dashed lines, respectively.

in the mixture. In view of Eqs. (5), they are represented as

$$c_e^2 = \frac{\gamma_e p}{\rho}, \quad c_{ef}^2 = \left(\gamma + e_1 \frac{d\gamma}{de_1}\right)\frac{p}{\rho},$$

$$\rho = \rho_1 + \rho_2 + \rho_3,$$

$$c_f^2 = \left(\gamma + e_1 \frac{d\gamma}{de_1}\right)\frac{p}{\rho_1}, \tag{7}$$

$$\gamma_e = \frac{R\gamma\xi_1 + (\gamma - 1)\omega + (\omega + \xi_1 R)e_1\dfrac{d\gamma}{de_1}}{R\xi_1 + (\gamma - 1)\omega + \omega e_1\dfrac{d\gamma}{de_1}},$$

$$\omega = \xi_2 c_2 + \xi_3 c_3.$$

Expressions (7) for $\gamma = $ const reduce to known dependences [15]. It is easy to show that the thermodynamic stability condition $c_e < c_{ef} < c_f$ is satisfied. Figure 3b shows an example of the Chapman–Jouguet detonation structure for $\xi_{30} = 0.3$ and $u_0 = 1.45$ [2]. The ignition point is characterized by the bend in the particle temperature distribution, because, in chemical reactions proceeding in the combustion regime, heat is released only in the gas phase. The behavior of the mixture parameters is similar to that for ignition in a passing shock wave (Fig. 3a). At the next stage of surface com-

bustion of the particle, which is two orders of magnitude longer than the ignition delay time, processes proceed under the conditions of velocity equilibrium between the phases.

## REFERENCES

1. D. H. Edwards, P. J. Fearnley, and M. A. Nettleton, Fiz. Goreniya Vzryva **23** (2), 129 (1987) [Combust., Explos. Shock Waves **23** (2), 239 (1987)].

2. A. V. Fedorov and T. A. Khmel', Fiz. Goreniya Vzryva **38** (6), 103 (2002) [Combust., Explos. Shock Waves **38** (6), 700 (2002)].

3. M. Sichel, S. W. Baek, C. W. Kauffman, *et al.*, AIAA J. **23**, 1374 (1985).

4. Yu. A. Gosteev and A. V. Fedorov, Fiz. Goreniya Vzryva **39** (2), 67 (2003) [Combust., Explos. Shock Waves **39** (2), 177 (2003)].

5. V. M. Boĭko, A. N. Papyrin, and S. V. Poplavskiĭ, Fiz. Goreniya Vzryva **29** (3), 143 (1993) [Combust., Explos. Shock Waves **29** (3), 389 (1993)].

6. V. A. Levin and Yu. V. Tunik, Dokl. Akad. Nauk SSSR **276**, 834 (1984) [Sov. Phys. Dokl. **29**, 446 (1984)].

7. L. D. Smoot, M. D. Horton, and G. A. Williams, in *Proceedings of the 16th International Symposium on Combustion, Pittsburgh, 1977*, p. 375.

8. S. A. Zhdan and E. S. Prokhorov, Fiz. Goreniya Vzryva **35** (4), 79 (1999) [Combust., Explos. Shock Waves **35** (4), 422 (1999)].

9. V. V. Koren'kov and V. N. Okhitin, Prikl. Mekh. Tekh. Fiz., No. 3, 127 (1983) [J. Appl. Mech. Tech. Phys. **24**, 403 (1983)].

10. S. K. Ubhayakar, D. B. Stickler, C. W. von Rosenberg, and R. E. Gannon, in *Proceedings of the 16th International Symposium on Combustion, Pittsburgh, 1976*, p. 427.

11. T. W. Lester, W. R. Seeker, and J. F. Merklin, in *Proceedings of the 18th International Symposium on Combustion, Pittsburgh, 1981*, p. 1257.

12. I. W. Smith, in *Proceedings of the 19th International Symposium on Combustion, Pittsburgh, 1982*, p. 1045.

13. P. A. Libby and T. A. Blake, Combust. Flame **36**, 139 (1979).

14. Yu. A. Gosteev and A. V. Fedorov, Fiz. Goreniya Vzryva **37** (6), 36 (2001) [Combust., Explos. Shock Waves **37** (6), 446 (2001)].

15. A. V. Fedorov and T. A. Khmel', Fiz. Goreniya Vzryva **33** (6), 80 (1997) [Combust., Explos. Shock Waves **33** (6), 495 (1997)].

*Translated by R. Tyapaev*

$=$ **MECHANICS** $=$

# On the Equations of Axisymmetric Motion
# of a Viscous Incompressible Fluid

**S. N. Aristov\* and** Corresponding Member of the RAS **V. V. Pukhnachev\*\***

**1.** In the cylindrical coordinate system $(r, \theta, z)$, the equations of axisymmetric motion of a viscous incompressible fluid in the absence of external forces have the form

$$u_t + uu_r + wu_z - \frac{v^2}{r} = -p_r + \nu\left(u_{rr} + \frac{1}{r}u_r - \frac{1}{r^2}u + u_{zz}\right),$$

$$v_t + uv_r + wv_z + \frac{uv}{r} = \nu\left(v_{rr} + \frac{1}{r}v_r - \frac{1}{r^2}v + v_{zz}\right),$$

$$w_t + uw_r + ww_z = -p_z + \nu\left(w_{rr} + \frac{1}{r}w_r + w_{zz}\right),$$

$$u_r + \frac{u}{r} + w_z = 0,$$

(1)

where $u$, $v$, and $w$ are the radial, azimuthal, and axial velocity components, respectively; $p$ is the fluid pressure; and $\nu$ is the kinematical viscosity. Without restriction of generality, the fluid density is taken to be equal to unity, and the fluid is subjected to potential external forces. In this case, $p$ is the modified pressure that is equal to the sum of the original pressure and external-force potential.

As is known [1], system (1) reduces to two equations relating the azimuthal velocity $v$ component to the current function $\psi$ defined by the expressions

$$u = -\frac{1}{r}\psi_z, \quad v = \frac{1}{r}\psi_r.$$

(2)

Below, we will propose another form of the equations under investigation, which is based on the following

property. The substitution of Eqs. (2) into the third of Eqs. (1) provides

$$\frac{\partial}{\partial r}\left(\psi_t - \frac{1}{r}\psi_r\psi_z - \nu E\psi\right) + \frac{\partial}{\partial z}\left(rp + \frac{1}{r}\psi_r^2\right) = 0,$$

where

$$E = \frac{\partial^2}{\partial r^2} - \frac{1}{r}\frac{\partial}{\partial r} + \frac{\partial^2}{\partial z^2}$$

is the Stokes operator. Therefore, there is a function $\Phi$ satisfying the relations

$$p = -\frac{1}{r^2}\psi_r^2 + \frac{1}{r}\Phi_r,$$

(3)

$$\psi_t - \frac{1}{r}\psi_r\psi_z + \Phi_z = \nu E\psi.$$

(4)

The substitution of Eqs. (2) into the second of Eqs. (1) provides

$$J_t - \frac{1}{r}\psi_z J_r + \frac{1}{r}\psi_r J_z = \nu EJ,$$

(5)

where $J = rv$. Differentiating Eqs. (3) and (4) with respect to $r$ and $z$, respectively, and substituting the resulting expressions into the first of Eqs. (1), where $u$ and $w$ are expressed in terms of $\psi$, we obtain

$$E\Phi = \frac{1}{r^2}(J^2 + \psi_z^2) + \frac{2}{r}\psi_r E\psi.$$

(6)

We will analyze the system of Eqs. (4)–(6).

**2.** Then, $R^+$ is the $r > 0$ half-plane of the $(r, z)$ plane, $\Omega$ is the bounded domain in $R^+$, $\Sigma$ is the boundary of $\Omega$, $Q_T = \Omega \times (0, T)$, and $S_T = \Sigma \times (0, T)$. For simplicity, we assume that the closure $\Omega$ of the domain $\Omega$ does not contain points lying on the $z$ axis. For the natural statement of the initial boundary value problem for system (1), the functions $u$, $v$, and $w$ are specified on the lower base of $\Omega$ and on the lateral surface $S_T$ of the cyl-

\* *Institute of Mechanics of Continua, Ural Division,*
 *Russian Academy of Sciences,*
 *ul. Akademika Koroleva 1, Perm, 614013 Russia*
 *e-mail: asn@icmm.ru*
\*\* *Lavrent'ev Institute of Hydrodynamics, Siberian Division,*
 *Russian Academy of Sciences,*
 *pr. Akademika Lavrent'eva 15,*
 *Novosibirsk, 630090 Russia*
 *e-mail: pukh@hydro.nsc.ru*

inder $Q_T$. It is known that this problem with sufficiently smooth input data has the unique classical solution for any $T > 0$ [2].

Below, we will consider only the case where the adhesion conditions $u = v = w = 0$ are satisfied at the boundary of the flow domain. In terms of the functions $\psi$ and $J$, these conditions are represented in the form

$$\frac{\partial \psi}{\partial n} = 0, \quad (r, z, t) \in S_T, \qquad (7)$$

$$\psi = 0, \quad J = 0, \quad (r, z, t) \in S_T, \qquad (8)$$

where $\dfrac{\partial}{\partial n}$ means differentiation with respect to the normal to the $\Sigma$ line. To close the formulation of the problem for the system of Eqs. (4)–(6), it is necessary to specify the initial conditions

$$\psi = \psi_0(r, z), \quad (r, z) \in \overline{\Omega}, \quad t = 0, \qquad (9)$$

$$J = J_0(r, z), \quad (r, z) \in \overline{\Omega}, \quad t = 0, \qquad (10)$$

and boundary conditions for the function $\Phi$ by using condition (7), which is redundant for Eq. (4). To this end, we transform Eq. (6) into a fourth-order equation by applying the operator $E$:

$$E^2\Phi = E\left[\frac{1}{r^2}(J^2 + \psi_z^2) + \frac{2}{r}\psi_r E\psi\right]. \qquad (11)$$

One boundary condition for Eq. (11) follows immediately from Eqs. (6)–(8):

$$E\Phi = 0, \quad (r, z, t) \in S_T. \qquad (12)$$

Applying the operator $\dfrac{\partial}{\partial n}$ to Eq. (6) and using Eqs. (7) and (8), we arrive at the second condition

$$\frac{\partial}{\partial n}E\Phi = \frac{2}{r}\frac{\partial \psi_r}{\partial n}E\psi, \quad (r, z, t) \in S_T. \qquad (13)$$

The problem of determining $\psi$, $J$, and $\Phi$ is finally formulated as follows: to find those solutions of the system of Eqs. (4), (5), and (11) which satisfy conditions (8)–(10), (12), and (13).

Equations (4), (5), and (11) form a weakly coupled system of two parabolic second-order equations, for which the first initial boundary value problem is stated, and one linear elliptic fourth-order equation, for which a Neumann-type problem is stated. In this respect, it is similar to the traditional system of equations of axisymmetric motion that is written in terms of $\psi$, $v$, and $\omega = r^{-1}E\psi$. The advantage of the new form of the equations is that the boundary conditions for the functions $\psi$, $J$, and $\Phi$ are uncoupled, in contrast to the traditional approach, where the determination of the boundary values of the function $\omega$ is a serious computation problem.

Concluding this section, we note that Eq. (7) follows from Eqs. (6) and (13) under the additional condition

$$\frac{1}{r^2}\frac{\partial \psi_z}{\partial n}\cos\varphi + \frac{\partial}{\partial n}\left(\frac{1}{r}E\psi\right)\sin\varphi \neq 0, \quad (r, z, t) \in S_T,$$

where $\varphi$ is the angle between the $z$ axis and the normal to the $\Sigma$ line. If the last condition is valid for $t = 0$, it is satisfied at least for small $T > 0$.

**3.** The general Navier–Stokes equations, as well as the equations of axisymmetric motion, have a rich symmetry group [3, 4]. Since the transition from Eqs. (1) to the system of Eqs. (4)–(6) involves nonlocal transformations, groups admitted by both systems are not isomorphic. The widest transformation group admitted by Eqs. (4)–(6) was found by S.V. Golovin. The basis of the corresponding Lie algebra is formed by the operators

$$X_1 = \partial_t, \quad X_2 = 2t\partial_t + r\partial_r + z\partial_z + \psi\partial_\psi,$$

$$X_3 = 2\alpha\partial_z + r^2\dot{\alpha}\partial_\psi + (4\dot{\alpha} - r^2 z\ddot{\alpha})\partial_\Phi,$$

$$X_4 = \beta\partial_\psi - z\dot{\beta}\partial_\Phi, \quad X_5 = \gamma\partial_\Phi, \quad X_6 = r^2\delta\partial_\Phi,$$

where $\alpha$, $\beta$, $\gamma$, and $\delta$ are arbitrary functions (belonging to $C^\infty$) of $t$ and the dot means differentiation with respect to $t$.

Since the symmetry group of the system of Eqs. (4)–(6) involves transformations depending on arbitrary functions of time, invariant solutions of this system can be constructed with *a priori* functional arbitrariness. One example of such solutions is as follows. We consider a group generated by the operator $X_3 + X_4$. The solution invariant under this group has the general form

$$\psi = \frac{z}{2\alpha}(r^2\dot{\alpha} + 2\beta) + f(r, t), \quad J = g(r, t),$$

$$\Phi = \frac{z^2}{2\alpha^2}\left[r^2\left(\dot{\alpha}^2 - \frac{\alpha\ddot{\alpha}}{2}\right) + 2\dot{\alpha}\beta - \alpha\dot{\beta}\right] + \frac{2\dot{\alpha}z}{\alpha}f + h(r, t). \qquad (14)$$

The functions $f$, $g$, and $h$ satisfy the recurrence system of the linear equations

$$f_t - \frac{r^2\dot{\alpha} + 2\beta}{2\alpha r}f_r + 2\frac{\dot{\alpha}}{\alpha}f = \nu\left(f_{rr} - \frac{1}{r}f_r\right),$$

$$g_t - \frac{r^2\dot{\alpha} + 2\beta}{2\alpha r}g_r = \nu\left(g_{rr} - \frac{1}{r}g_r\right),$$

$$h_{rr} - \frac{1}{r}h_r + \frac{1}{\alpha^2}\left[r^2\left(\dot{\alpha}^2 - \frac{\alpha\ddot{\alpha}}{2}\right) + 2\dot{\alpha}\beta - \alpha\dot{\beta}\right]$$

$$= \frac{1}{r^2}\left[g^2 + \frac{(r^2\dot{\alpha} + 2\beta)^2}{4\dot{\alpha}}\right] + \frac{2}{r}f_r\left(f_{rr} - \frac{1}{r}f_r\right).$$

Solution (14) generalizes the well-known Burgers vortex [5]. First, it describes nonstationary motion.

Second, the velocity field for $\beta \neq 0$ has a singularity that lies on the symmetry axis and is generated by uniformly distributed source with linear density $-\dfrac{\beta}{4\pi\alpha}$ arbitrarily time-dependent. We emphasize that the classical Burgers solution has a nontrivial group-theoretical origin: it is not an invariant solution to system (1) but can be obtained as an invariant solution of a certain partially invariant submodel of this system. At the same time, the use of Eqs. (4)–(6) enables one to easily obtain the Burgers solution and its generalizations.

**4.** Exact solutions of the system of Eqs. (4)–(6) are not exhausted by its invariant solutions. One of them (stationary cylindrical vortex) was constructed in [6]. In this solution, the velocity components $v$ and $w$ are proportional to $z$ and the component $u$ is independent of $z$. The group-theoretical origin of this solution was revealed in [7]. Based on Eqs. (4)–(6), it is easy to generalize solutions found in [6] to the nonstationary case and for inhomogeneous functions $v$ and $w$ of $z$. To this end, it is sufficient to set

$$\psi = Az + B, \quad J = Cz + D, \quad \Phi = Fz^2 + Gz + H,$$

where $A$, $B$, $C$, $D$, $F$, $G$, $H$ are the functions of $r$ and $t$ and $A$, $C$, and $F$ satisfy the closed quasilinear system of equations

$$A_t - \frac{1}{r}AA_r + 2F = \nu\left(A_{rr} - \frac{1}{r}A_r\right),$$

$$C_t - \frac{1}{r}AC_r + \frac{1}{r}A_r C = \nu\left(C_{rr} - \frac{1}{r}C_r\right), \qquad (15)$$

$$F_{rr} - \frac{1}{r}F_r = \frac{1}{r^2}C^2 + \frac{2}{r}A_r\left(A_{rr} - \frac{1}{r}A_r\right).$$

With known $A$, $C$, and $F$, the functions $B$, $D$, $G$, and $H$ are determined from the system of linear equations omitted here. We note that the latter system always has a solution in which the functions $B$, $D$, and $G$ are equal to zero, and the equation for the function $H$ is solved in quadratures.

It is important that system (15) inherits some properties of the generating system of Eqs. (4)–(6). In particular, it admits the extension operator

$$X_7 = 2t\partial_t + r\partial_r - C\partial_c - 2F\partial_F.$$

The solution of system (15) that is invariant under the operator $X_7$ corresponds to the new self-similar solution

$$u = \frac{1}{\sqrt{t}}\bar{u}(\xi), \quad v = \frac{z}{t}\bar{v}(\xi), \quad w = \frac{z}{t}\bar{w}(\xi),$$

$$p = \frac{z^2}{t^2}\bar{p}(\xi) + \frac{1}{t}\bar{q}(\xi) \qquad (16)$$

to Eqs. (1), where $\xi = r(\nu t)^{-1/2}$. Analysis of solution (16) is beyond the scope of this paper.

**5.** We assume that the solution to the system of Eqs. (4)–(6) is defined in the domain $\Pi_T = R^+ \times (0, T)$ and satisfies the conditions $\psi \to 0$ for $\rho = \sqrt{r^2 + z^2} \to \infty$ and

$$\frac{|\nabla\psi|}{r}, \ |E\psi|, \ \frac{|J|}{r} \leq C_1(1 + \rho)^{-m} \qquad (17)$$

with certain constants $2 < m \leq 4$ and $C_1 = C_1(T) > 0$. Using the results from [8, 9] (see also the references cited therein) and the axial symmetry of the velocity field, one can show that inequalities (17) are satisfied in the domain $\overline{\Pi}_T$ for a certain $T > 0$ if they are valid for $t = 0$ with a certain constant $C_0 > 0$.

Owing to estimates (17), the solution $\Phi$ to Eq. (6) that is regular on the $z$ axis and its derivatives can be represented as

$$\Phi = \frac{C_2 r^2}{\rho^3} + O\left(\frac{r^2}{\rho^4}\right), \quad \Phi_z = -\frac{3C_2 r^2 z}{\rho^5} + O\left(\frac{r^2}{\rho^5}\right),$$

$$\Phi_r = \frac{C_2 r(2z^2 - r^2)}{\rho^5} + O\left(\frac{r}{\rho^4}\right), \qquad (18)$$

where $C_2 = \text{const} > 0$. Expressions (18) mean that the solution to inhomogeneous equation (6) with the rapidly decreasing right-hand side behaves for large $\rho$ values as the fundamental solution $-r^2(4\pi\rho^3)^{-1}$ to the equation $E\Phi = 0$ with a singularity at the origin. We apply inequalities (17) and (18) to obtain integral identities for the velocity field of axisymmetric motion of the fluid filling the entire space.

Equation (6) can be represented in the equivalent form

$$\frac{\partial}{\partial r}(r\Phi_r - 2\Phi + \psi_z^2 - \psi_r^2) + \frac{\partial}{\partial z}(r\Phi_z - 2\psi_z\psi_r)$$

$$= r(u^2 + v^2 - 2w^2),$$

where the velocity components $u$ and $w$ are expressed in terms of $\psi_r$ and $\psi_z$ by Eqs. (2) and $v = r^{-1}J$. Integrating this equation over the domain $R^+$ and using estimates (17) and (18), we arrive at the identity

$$\int_{R^+} (u^2 + v^2 - 2w^2)r\,dr\,dz = 0, \quad 0 < t \leq T. \qquad (19)$$

This identity is a particular case of identities obtained in [10] by means of rather complex manipulations.

Multiplication of Eq. (4) by $r$ and integration of the result over the disk $\rho < N$, $r > 0$ provide one more interesting identity. Under the assumption that the exponent $m$ in inequalities (17) lies in the range (3, 4], a limit of

the mentioned identity for $N \to \infty$ exists. The limiting relation has the form

$$\frac{d}{dt}\int_{R^+} r\psi\,dr\,dz = -\int_{R^+} r^2 uw\,dr\,dz. \qquad (20)$$

Identities (19) and (20) do not involve the "superfluous" function $\Phi$, whose physical sense is unclear. They are remarkable because they do not explicitly involve the viscosity $\nu$ and are valid in the limit $\nu \to 0$.

## ACKNOWLEDGMENTS

## REFERENCES

1. V. I. Polezhaev, A. V. Buné, N. A. Verezub, *et al.*, *Mathematical Modeling of Convective Heat and Mass Transfer Using the Navier–Stokes Equations* (Nauka, Moscow, 1987).

2. O. A. Ladyzhenskaya, *Mathematical Problems of the Dynamics of Viscous Incompressible Fluid* (Nauka, Moscow, 1970).

3. V. K. Andreev, O. V. Kaptsov, V. V. Pukhnachev, and A. A. Rodionov, *Group-Theoretical Methods: Application for Thermodynamics* (Nauka, Novosibirsk, 1994).

4. L. V. Kapitanskiĭ, Dokl. Akad. Nauk SSSR **243**, 901 (1978) [Sov. Phys. Dokl. **23**, 896 (1978)].

5. J. M. Burgers, Adv. Appl. Mech. **1**, 171 (1948).

6. S. N. Aristov, Dokl. Akad. Nauk **377**, 477 (2001) [Dokl. Phys. **46**, 251 (2001)].

7. S. V. Golovin, in *Proceedings of the International Conference on Symmetry and Differential Equations, Krasnoyarsk, 2001*, p. 177.

8. T. Miyakava, Funkc. Ekvacioj. **43**, 542 (2000).

9. L. Brandolese, C. R. Acad. Sci., Ser. I: Math. **332**, 125 (2001).

10. S. Yu. Dobrokhotov and A. I. Shafarevich, Izv. Ross. Akad. Nauk, Mekh. Zhidk. Gaza, No. 4, 38 (1996).

*Translated by R. Tyapaev*

=========== **MECHANICS** ===========

# Stream Function of the Two-Dimensional Flow Problem, Robin Potential, and the Exterior Dirichlet Problem

## V. G. Lezhnev

For the stream function of the plane-parallel flow around an airfoil $S$, a constructive representation is given involving the Robin potential, which alone determines circulation. Algorithms for the approximate solution of, in particular, the exterior Dirichlet problem are also developed.

Let $Q^+ = R^2 \backslash \overline{Q}$, where $Q$ is a bounded, simply connected domain in the $Ox_1x_2$ plane, and $S = \partial Q$. For the flow around the airfoil in $Q^+$, it is necessary to determine the velocity field $w(x) = \{u, v\}$ satisfying the following main conditions:

(a) $\operatorname{div} w(x) = 0$, $\operatorname{curl} w(x) = 0$, $x = (x_1, x_2) \in Q^+$;

(b) $w(\infty) = \{u_0, v_0\}$;

(c) $S$ is a streamline of the $\overline{w}(x)$ field.

**1.** The function $f_1(z) = u - iv$, where $z = x_1 + ix_2$, called the complex velocity, is analytic in $Q^+$ and, in the vicinity of the point $z = \infty$, can be expanded as

$$f_1(z) = (u_0 - iv_0) + c_1 z^{-1} + c_2 z^{-2} + \ldots, \quad |z| \gg 1.$$

The function $f(z) = \varphi(x) + i\psi(x)$ such that $f'(z) = f_1(z)$ is called the complex potential of the flow $w(x)$, $\operatorname{grad}\varphi = \{\partial_{x_2}\psi, -\partial_{x_1}\psi\} = \{u, v\}$, $x \in Q^+$,

$$f(z) = (u_0 - iv_0)z + B\ln z + b_0 + b_1 z^{-1} + b_2 z^{-2} + \ldots,$$
$$|z| \gg 1.$$

The function $\psi(x) = \operatorname{Im} f(z)$ is harmonic in $Q^+$, constant on the streamlines, because $\nabla\psi(x)$ is orthogonal to $w(x)$,

$$\psi(x) = \text{const}, \quad x \in S \qquad (1)$$

and is called the stream function. In the vicinity of an infinitely distant point, the function $\psi(x)$ has the expansion

$$\psi(x) = (u_0 x_2 - v_0 x_1) + b\ln|x| + \psi_0(x), \quad |x| \gg 1, \quad (2)$$

*Kuban State University,*
*ul. Karla Libknekhta 149, Krasnodar, 350640 Russia*
*e-mail: lzhnv@mail.kubsu.ru*

where $\psi_0(x)$ is a bounded function harmonic in $Q^+$.

Any stream function of the flow under consideration satisfies conditions (1) and (2). These conditions with given $u_0$, $v_0$, and $b$ determine $\psi(x)$ up to an additive constant. The constants $u_0$ and $v_0$ determine the velocity at infinity, while $b$ determines the field circulation around the point $z = \infty$ and on the airfoil $S$.

We will determine the general form of the stream function for given $u_0$, $v_0$, and $b$. For the contour $S$, which is assumed to be a piecewise Lyapunov contour, we will consider the Robin potential $\psi_R(x)$

$$\psi_R(x) = \frac{1}{\pi}\int_S g^*(y)\ln\frac{1}{|x - y|}ds,$$

where the Robin potential density $g^*(x)$ is such that the function $\psi_R(x)$ is identically constant in $Q$ [1]. We will denote the scalar product and norm in the $L_2(S)$ space by $(\,,\,)$ and $\|\cdot\|$, respectively, and $E(x) = (2\pi)^{-1}\ln|x|$ is the fundamental solution of the Laplace equation.

**Lemma 1.** *In the problem of the flow around the airfoil $S$, the stream function $\psi(x)$ that satisfies conditions* (a)–(c) *and has the circulation $\Gamma$ can be represented in the form*

$$\psi(x) = (u_0 x_2 - v_0 x_1) + \psi_0(x) + C\psi_R(x),$$
$$x \in Q^+,$$

*where $\psi_R(x)$ is the Robin potential, $C = -\dfrac{1}{2}(g^*, 1)^{-1}\Gamma$, and $\psi_0(x)$ is a solution (bounded in $Q^+$) of the Dirichlet problem*

$$\Delta\psi_0(x) = 0 \quad (x \in Q^+),$$

$$\psi_0(x) = -u_0 x_2 + v_0 x_1 \quad (x \in S).$$

Indeed, $\psi(x)$ is constant on $S$ and harmonic in $Q^+$ by design, the vector field $w(x) = \{\partial_{x_2}\psi, -\partial_{x_1}\psi\}$ is tangent to the boundary $S$, and $\overline{w}(\infty) = \{u_0, v_0\}$. Thus, the main

conditions (a)–(c), together with condition (2), are fulfilled. The first two terms of the function $\psi(x)$ determine the velocity field of the irrotational flow around the airfoil, because the first term determines a constant vector field, while the gradient of the second term vanishes at infinity as $|x|^{-2}$. The circulation $\gamma$ of the vector field $\{\partial_{x_2}\psi_R, -\partial_{x_1}\psi_R\}$ is calculated by the formula

$$\gamma = -2\int_S g^*(y)ds = -2(g^*, 1),$$

i.e., the circulation of the vector field $w(x)$ on $S$ is equal to $\Gamma = -2C(g^*, 1)$.

The formulation of Lemma 1, together with conditions (1) and (2), necessarily indicates that the circulation of the velocity field in the incompressible potential flow around a single airfoil is determined by the Robin potential $C\psi_R(x)$. Its density $g^*(x)$ is the vortex density at the boundary $S$. From the electrostatic treatment of the problem, it follows that $g^*(x)$ increases at corner points.

**2.** We will now consider algorithms for the approximate calculation of the functions $\psi_R(x)$ and $\psi_0(x)$. In the unbounded domain $Q^+$, the solution $\psi_0(x)$ to the first boundary value problem for the Laplace equation is determined by the methods of potential theory in the form [1]

$$\psi_0(x) = \int_S g(y)\partial_{n(y)}E(x-y)ds + a, \quad x \in Q^+.$$

Passage to the boundary when $x \to x' \in S$ results in the integral equation

$$(I + K)g = -\frac{1}{2}(\psi_0(x)|_S - a)$$

for the required density $g(y)$. The unknown constant $a$ is determined from the condition that the right-hand side of the equation is orthogonal to the eigenfunction $g^*(x)$ of the conjugate operator $K^*$ for the eigenvalue $\lambda = -1$ (the eigenfunction $g^*(x)$ coincides with the Robin potential density; it is also known that $(g^*, 1) \neq 0$) [1].

Let a bounded sequence of points $x^m$, $m = 1, 2, \ldots,$ in $Q$ be separated from the boundary and satisfy the condition of uniqueness of harmonic functions in $R^2$[2], $L_2(S) = \{g^*\} \oplus L_2^g$, and

$$\delta_m(x) = E(x^{m+1} - x) - E(x^m - x), \quad x \in S.$$

**Lemma 2.** *The sequence of functions* $\delta_m(x)$, $m = 1$, $2, \ldots,$ *is complete and linearly independent in* $L_2^g$ [2].

Let $h_g$ and $h_0$ be the projections of a certain function $h(x)$ onto the subspaces $\{g^*\}$ and $L_2^g$ and $h_0^N$ be the pro-
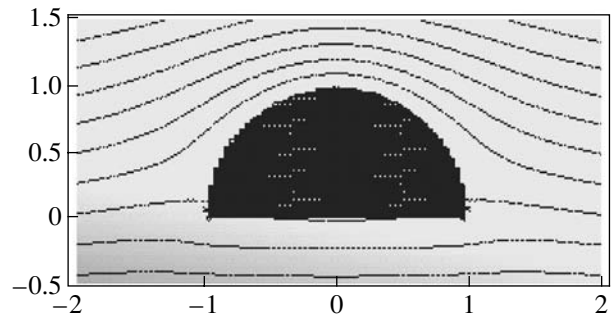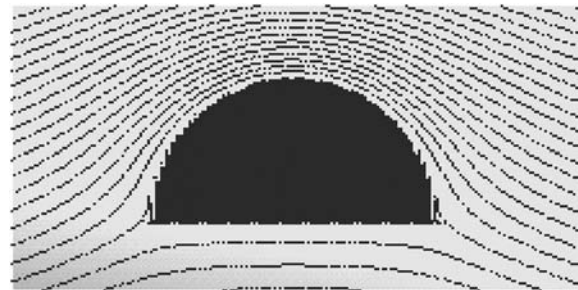


**Fig. 1.** Irrotational flow for $C = 0$.



**Fig. 2.** Flow for $C = -0.047$.



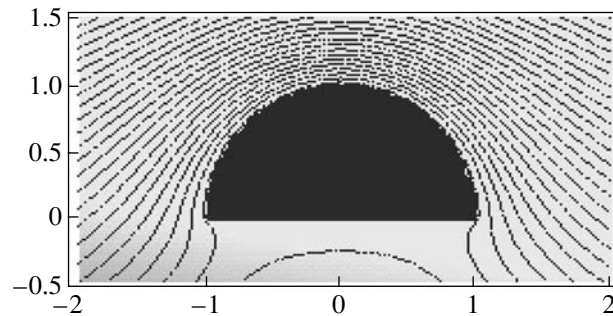**Fig. 3.** Flow for $C = -0.1$.

jection onto the subspace $\{\delta_m(x)\}_1^N$, $h_g \neq 0$. Then, $h_0^N \to h_0$ when $N \to \infty$, and the eigenfunction $g^*(x)$ and the constant $a$ satisfy the approximate equalities $h - h_0^N \approx Ag^*$, where $A$ is a constant, and

$$a \approx (\psi_0, h - h_0^N)/(1, h - h_0^N).$$

The function $h_0^N$ can be determined as a solution to the problem of minimizing the function $F(c) = F(c_1, c_2, \ldots, c_N)$

$$F(c) = \left\| h(x) - \sum_1^N c_m\delta_m(x) \right\|^2.$$

The approximate solution of the Dirichlet problem noted in Lemma 1 will be sought in the form

$$\psi_0^M(x) = a + \sum_1^M b_k \delta_k(x), \quad x \in Q^+,$$

where the last sum for $x \in S$ is determined as the approximation of the function $u_0 x_2 - v_0 x_1 - a$ belonging to $L_2^g$ in $L_2(S)$. The function $\psi_0^M(x)$ is bounded when $x \to \infty$.

**3.** In the numerical experiment for the flow around a semicircle presented in Figs. 1–3, we determined the Robin potential density as the eigenfunction of the operator $K^*$ on $S$ (for $N = 200$) for $\lambda = -1$, the solution of the exterior Dirichlet problem (for $M = 100$), and the streamline patterns for the flows with zero and nonzero circulations.

## REFERENCES

1. V. S. Vladimirov, *Equations of Mathematical Physics*, 2nd ed. (Nauka, Moscow, 1971; Dekker, New York, 1971).

2. V. G. Lezhnev and E. A. Danilov, *Two-Dimensional Hydrodynamic Problems* (Kubansk. Gos. Univ., Krasnodar, 2000).

*Translated by M. Lebedev*

=== **MECHANICS** ===

# Rise of a Near-Wall Liquid Film over the Outer Surface of a Nozzle Accompanying Supersonic Gas Flow into Vacuum

## V. G. Prikhodko, S. F. Chekmarev, V. N. Yarygin*, and I. V. Yarygin

Presented by Academician A.K. Rebrov September 1, 2003

Received September 22, 2003

## 1. INTRODUCTION

This study was initiated by the problem of external contamination of the surfaces of space vehicles (including the International Space Station) by jets of orientation and control thrusters, where a fuel film is used for cooling nozzle walls [1]. Although jet gas expansion into vacuum has been studied in numerous experimental and theoretical works (see, e.g., recent review [2]), the problem of joint gas flow with a near-wall liquid film has not yet been systematically investigated. Experimental modeling of such a flow [3, 4] shows that a near-wall liquid film flowing down on an inner surface of the nozzle not only breaks up into droplets at the output edge of the nozzle but also emerges onto the external surface of the nozzle, moving backwards on it, even opposite to gravity.

## 2. EXPERIMENT

Experiments were carried out on a VIKING vacuum gas-dynamic setup of the Kutateladze Institute of Thermal Physics [5]. The large volume of the working chamber (~150 m$^3$) provided operation in the pulse mode with high flow rates of a gas and liquid. The injected liquid was completely evaporated and evacuated by normal vacuum pumps.

The gas and liquid were fed from a gas-dynamic source, which made it possible to vary their flow rates and to change output head–nozzles. As such nozzles, we investigated a cylindrical tube 5 mm in diameter and a conic supersonic nozzle, which had a semiangle of $\alpha = 7°$; radii of critical and output sections of 5 and 10 mm, respectively; and a cylindrical external surface. In both cases, the thickness of the output section edge

*Kutateladze Institute of Thermophysics,*
*Siberian Division, Russian Academy of Sciences,*
*pr. Akademika Lavrent'eva 1, Novosibirsk, 630090 Russia*
* *e-mail: yarygin@itp.nsc.ru*

was equal to $l = 1$ mm. The nozzles were arranged vertically with the output section facing downwards.

The liquid entered through a circular gap in the stagnation chamber of the nozzle and flew down the nozzle walls as a film. Simultaneously, a gas was blown through the nozzle. At the nozzle exit, a supersonic freely expanding jet of vapor–gas mixture with dispersed liquid droplets was formed. We used air as the working gas and ethanol as the working liquid. The structure of the formed flow depended on the parameters of gas and liquid in the stagnation chamber and pressure $p_\infty$ in the vacuum chamber. The flow was recorded by video and photography.

Photographs of the cylindrical nozzle (Fig. 1) show how the structure of the flow changes with a decrease in pressure in the vacuum chamber. Figures 1a and 1b refer to the flows into space with atmospheric and low ($p_\infty \leq 10$ Pa) pressure, respectively. It is seen that the flow into vacuum is accompanied by the appearance of a 1-mm-thick liquid film on the outer surface of the nozzle. The same pattern is also observed in the case of the supersonic nozzle.

Figures 2 and 3 show the film rise height measured at various pressures in the vacuum chamber for the tube and supersonic nozzle, respectively. The stagnation pressure $p_0$ was equal to about $1.3 \times 10^5$ and $10^5$ Pa in the first and second cases, respectively. The stagnation temperature was equal to 300 K in both cases. The mass flow rate of the liquid was equal to about 10% of that of the gas.

## 3. DISCUSSION OF THE RESULTS

The analysis of the experimental data leads to the following scheme of the formation of the steady flow. As the gas and liquid are fed, a liquid film is formed on the inner wall of the nozzle. Under the action of the gas stream and gravity (predominantly, due to the first factor), this film moves to the edge of the nozzle. At this edge, the film turns around and emerges onto the outer surface of the nozzle. The turn of the film is caused by adhesion forces and, possibly, by the Coanda effect,
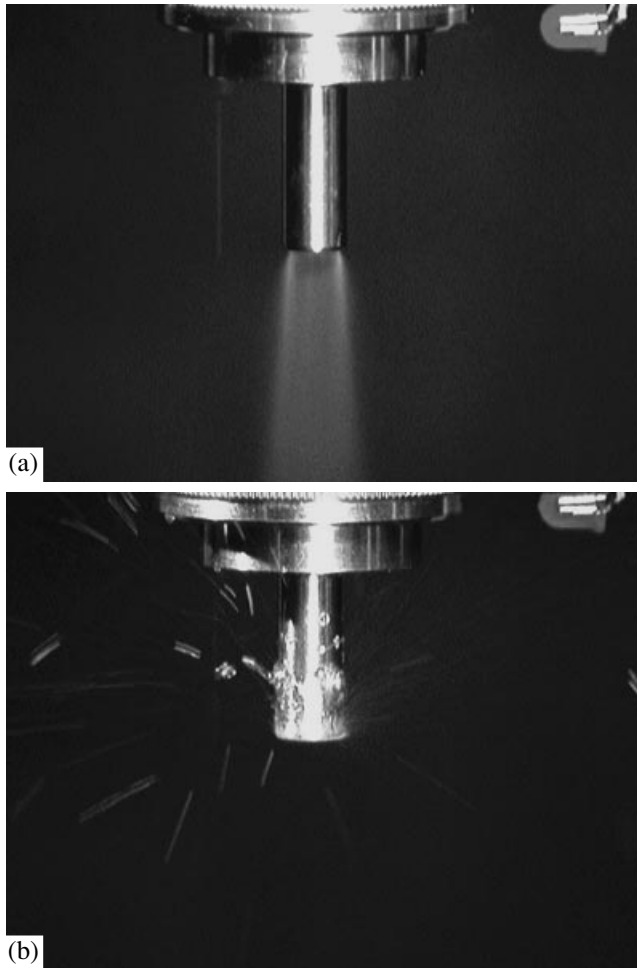
**Fig. 1.** Effect of ambient pressure on the structure of the flow into (a) the atmosphere and (b) vacuum.



**Fig. 2.** Film rise height over the outer surface of the tube. The circle is calculation and crosses are experimental data.

while the rise of the film is induced by its interaction with the gas flow. In this case, the maximum height $h_m$ of the film rise depends on the parameters of the gas flow and the liquid. Correspondingly, there is a certain critical amount of the liquid that can be contained in the film. As this amount of the liquid is gained in the film, the steady flow is formed: the film of a height of $h_m$ is formed on the outer surface of the nozzle, and newly fed liquid is completely carried away from the bottom edge of the nozzle by the flow in the form of droplets. The film is broken into droplets due to the Rayleigh–Taylor instability of the film under the action of both the gas flow and gravity.

The real process is certainly much more complicated. The surface of the film inside the nozzle can undergo perturbations, which result in tearing-off of droplets and/or disintegration of the film and stimulate the Rayleigh–Taylor instability of the film at the bottom edge. When reaching the edge and the outer surface of the nozzle, the liquid can explosively boil and/or actively evaporate. Viscosity effects can be significant for certain liquids, and adhesion forces can be substan-
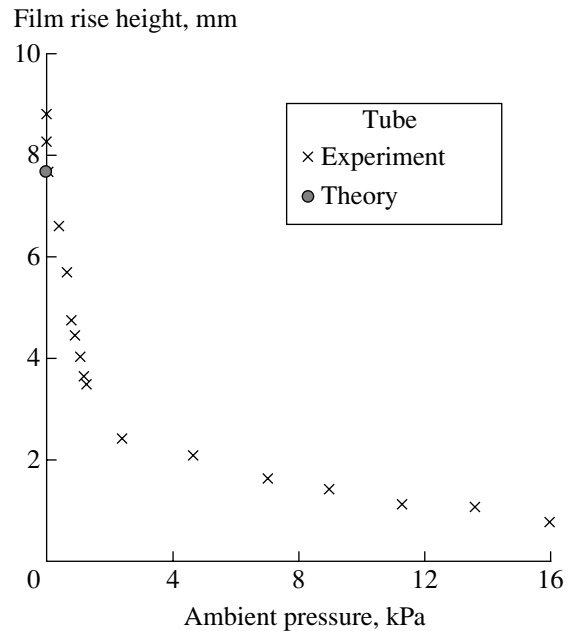
tial for certain combinations of the liquid and nozzle material.

Nevertheless, the proposed scheme enables us to construct a model providing estimates in satisfactory agreement with experiments.

To fit the experimental conditions (the nozzle is arranged vertically with the output section facing downwards), the film rise height can be estimated from the balance of forces at the film

$$\rho_l g h_m = p_{g1} - p_{g2} + p_L. \qquad (1)$$

Here, $\rho_l$ is the density of the liquid; $g$ is the gravitational acceleration; $p_{g1}$ and $p_{g2}$ are the pressures in the gas at the bottom and top edges of the film, respectively; and $p_L$ is the Laplace pressure at the bottom edge of the film, which is equal to $\dfrac{\sigma}{r}$ in this case, where $\sigma$ is the surface tension in the liquid and $r$ is the radius of curvature of the film surface. For ethanol, $\rho_l = 0.79$ g/cm$^3$ and $\sigma = 0.022$ N/m.

Taking into account that the characteristic thickness of the film inside the nozzle (~0.1 mm) is much less than the edge thickness $l$ and the thickness of the film at the outer surface is comparable with $l$, we can set $r = l$ for the calculation of the Laplace pressure. This gives $p_L = 22$ Pa for both cylindrical and conic nozzles.

For the cylindrical nozzle, $p_{g1}$ can be taken as the pressure reached at the 90° turn in the Prandtl–Mayer wave for a gas flow with the Mach number $M_C = 1$ at the nozzle section and adiabatic index $\gamma = 1.4$. In this
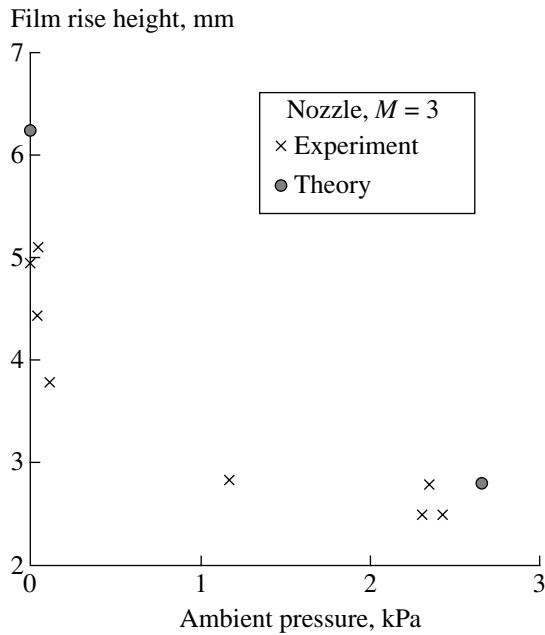
Film rise height, mm



**Fig. 3.** Same as in Fig. 2 but for the supersonic nozzle with $M = 3$.

case, $\dfrac{p_{g1}}{p_0} \approx 2.9 \times 10^{-4}$, and we obtain $p_{g1} \approx 39$ Pa for the conditions of experiments shown in Fig. 2. The same value of $\dfrac{p_{g1}}{p_0}$ can also be accepted for the conic nozzle, taking into account that there is a boundary layer inside the nozzle, so that the value M = 1 rather than the "geometric" value $M_C = 3$ is characteristic near the nozzle edge. In this case, we have $p_{g1} \approx 29$ Pa.

Pressure at the top boundary of the film depends on a number of factors (degree of jet underexpansion, its rarefaction, etc.) and generally requires numerical cal-culation of the flow field. However, estimates in two cases can be made without numerical simulation. The first case is expansion into virtually vacuum ($p_\infty \approx 0$), when $p_{g2}$ can be neglected. As a result, formula (1) provides $h_m \approx 7.7$ and $6.6$ mm for cylindrical and conic nozzles, respectively. The second case is design jet regime $p_C = p_\infty$ in experiments for the conic nozzle. Here, $p_{g1} = p_{g2}$, and Eq. (1) gives $h_m \approx 2.8$ mm. As is seen in Figs. 2 and 3, the theoretical estimates of $h_m$ shown by circles agree well with the experimental data. This agreement provides hope that the proposed simple model takes into account the principal factors determin-ing the formation of the film on the outer surface of the nozzle.

## ACKNOWLEDGMENTS

## REFERENCES

1. V. N. Yarygin, V. G. Prikhodko, I. V. Yarygin, *et al.*, Teplofiz. Aéromekh. **10**, 279 (2003).

2. A. K. Rebrov, J. Vac. Sci. Technol. A **19**, 1679 (2001).

3. V. N. Yarygin, V. G. Prikhodko, and Yu. I. Gerasimov, in *Proceedings of the 10th International Conference on the Methods of Aerophysical Research, Novosibirsk, 2000*, Part 3, p. 146.

4. V. G. Prikhodko and V. N. Yarygin, Teplofiz. Aéromekh. **7**, 459 (2000).

5. V. G. Prikhodko, G. A. Khramov, and V. N. Yarygin, Prib. Tekh. Éksp., No. 2, 162 (1996).

*Translated by V. Bukhanov*

═══════════ **MECHANICS** ═══════════

# Generation of Three-Dimensional Periodic Internal Waves by Compact Sources

## Yu. D. Chashechkin and A. Yu. Vasil'ev

Presented by Academician D.M. Klimov September 3, 2003

Approximate methods [1] for calculating internal-wave generation include certain empirical parameters. These parameters are not universal [2] and have to be determined experimentally. In this case, approximate solutions can differ rather considerably from exact ones when the parameters of model sources and sinks are found in the framework of the viscous-fluid theory [3] or of the conventional perfect-fluid theory [1, 4]. In [3], a more exact method was proposed for constructing a solution satisfying both the equations and boundary conditions on a radiating surface. The method allows us to calculate internal waves and complementary boundary layers. In the case of two-dimensional periodic internal waves generated by a strip oscillating in its own plane, calculated results based on the linear radiation theory are in satisfactory agreement with the experimental data of [5].

Similar calculations for three-dimensional waves are of practical interest. The linearized problem of generation of the three-dimensional periodic internal waves is simplified in the particular case of a wave source in the form of a vertical cylinder. This is associated with the correlation of symmetries intrinsic to both a source and the radiation field [6]. In this paper, we present an exact solution of a more general problem on three-dimensional periodic internal waves generated by a part of a plane inclined at an arbitrary angle $\varphi$ to the horizon.

We analyze the periodic motion of exponentially stratified incompressible viscous fluid whose density decreases as its height increases:

$$\rho_0(z) = \rho_{00}\exp\left(-\frac{z}{\Lambda}\right).$$

Here, $\Lambda$ is the buoyancy scale, $N = \sqrt{\dfrac{g}{\Lambda}}$ is the buoyancy frequency (the $z$ axis is opposite to the gravity acceler-

ation vector **g**), and $\nu$ is the kinematic viscosity assumed to be constant. We consider steady-state oscillations, with the velocity amplitude of the moving source being $u_0$. The time dependence of all the variables is taken as harmonic, and the common factor $\exp(-i\omega t)$ below is omitted.

In the case that toroidal-poloidal decomposition [7] is used and in the Boussinesq approximation, the equations of motion are reduced to the following equations for the scalar functions $\Phi$ and $\Psi$ related to the three-dimensional fluid velocity $\mathbf{v} = \nabla \times \mathbf{e}_z\Psi + \nabla \times (\nabla \times \mathbf{e}_z\Phi)$:

$$(\omega^2\Delta - N^2\Delta_\perp - i\omega\nu\Delta^2)\Phi = 0,$$
$$(\omega - i\nu\Delta)\Psi = 0. \tag{1}$$

Here, $\mathbf{e}_z$ is the unit vector of the $z$ axis and $\Delta$ is the Laplace operator; i.e., $\Delta_\perp = \partial_{xx}^2 + \partial_{yy}^2$. In Eqs. (1), additional solutions and factors corresponding to them are omitted.

The geometry of the problem and the relevant coordinate systems are shown in the figure. The gravity direction defines the laboratory $(x, y, z)$ coordinate system. The local coordinate system $(\xi, \eta, \zeta)$ associated with the radiating surface is obtained by rotating the coordinate system $(x, y, z)$ through the angle $\varphi$ about the $y$ axis. In this case, the $\xi$ axis and $\eta$ axis are located in the source plane, while the $\zeta$ axis is perpendicular to this plane. The comoving $(q, p, \alpha)$ coordinate system is attached to the wave cone inclined at an angle $\theta = \arcsin\dfrac{\omega}{N}$ to the horizon, the $q$ axis ($p$ axis) is oriented along (crosswise) the wave propagation direction, and $\alpha$ is the angular variable. The auxiliary cylindrical coordinate system $(r, \alpha, z)$, also attached to the wave cone, is given by the equations

$$\xi = x\cos\varphi + z\sin\varphi, \quad \eta = y,$$
$$\zeta = -x\sin\varphi + z\cos\varphi,$$
$$x = r\cos\alpha, \quad y = r\sin\alpha, \quad z = z, \tag{2}$$
$$p = r\sin\theta - z\cos\theta, \quad q = r\cos\theta + z\sin\theta.$$

*Institute of Problems in Mechanics,*
*Russian Academy of Sciences,*
*pr. Vernadskogo 101, Moscow, 117526 Russia*
*e-mail: chakin@ipmnet.ru; corwin@ipmnet.ru*

The no-slip conditions at the moving and quiescent parts of the $O\xi\eta$ plane serve as boundary conditions. All perturbations in viscous fluid attenuate at infinity. The unperturbed fluid is assumed to be at rest.

We seek a solution to system (1) in the form of the Fourier integral

$$\Phi = \int_{-\infty}^{+\infty} [A(k_\xi, k_\eta)\exp(ik_1(k_\xi, k_\eta)\zeta) + B(k_\xi, k_\eta)$$

$$\times \exp(ik_2(k_\xi, k_\eta)\zeta)]\exp(ik_\xi\xi + ik_\eta\eta)dk_\xi dk_\eta,$$

$$\Psi = \int_{-\infty}^{+\infty} C(k_\xi, k_\eta)\exp(ik_3(k_\xi, k_\eta)\zeta \qquad (3)$$

$$+ ik_\xi\xi + ik_\eta\eta)dk_\xi dk_\eta.$$

The components of the wave vector **k** are found from the dispersion equation presented here in the multiplicative form

$$\omega^2(k_{1,2}^2 + k_\xi^2 + k_\eta^2) - N^2[(k_\xi\cos\varphi - k_{1,2}\sin\varphi)^2$$

$$+ k_\eta^2] + i\omega\nu(k_{1,2}^2 + k_\xi^2 + k_\eta^2)^2 = 0, \qquad (4)$$

$$k_3^2 = -\frac{\omega}{i\nu} - k_\xi^2 - k_\eta^2.$$

The roots of this dispersion equation are found by conventional methods with due regard to the small viscosity and weak stratification [8]. The roots are chosen from the condition of perturbation attenuation at infinity:

$$\text{Im}k_1 > 0, \quad \text{Im}k_2 > 0, \quad \text{Im}k_3 > 0.$$

The coefficients $A$, $B$, and $C$ are determined from the linear equations obtained by the substitution of Eq. (3) into the boundary conditions:
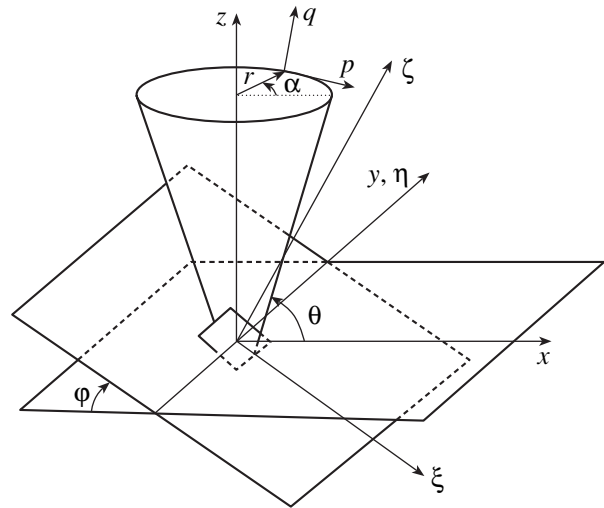
$$A(k_\eta^2\sin\varphi + k_1\beta_1) + B(k_\eta^2\sin\varphi + k_2\beta_2)$$

$$+ iCk_\eta\cos\varphi = U_\xi, \quad -Ak_\eta\gamma_1 - Bk_\eta\gamma_2 + iC\gamma_3 = U_\eta,$$

$$A(k_\eta^2\cos\varphi - k_\xi\beta_1) + B(k_\eta^2\cos\varphi - k_\xi\beta_2) \qquad (5)$$

$$- iCk_\eta\sin\varphi = U_\zeta.$$

Here,

$$\mathbf{U} = \frac{1}{4\pi^2}\int_{-\infty}^{+\infty} \mathbf{u}(\xi, \eta)\exp(-ik_\xi\xi - ik_\eta\eta)d\xi d\eta,$$

$$\beta_i = k_i\sin\varphi - k_\xi\cos\varphi, \quad \gamma_i = k_i\cos\varphi + k_\xi\sin\varphi,$$

where $\mathbf{U}(k_\xi, k_\eta)$ is the Fourier transform of the velocity $\mathbf{u}(\xi, \eta)$ of the source.

Coordinate systems of the problem.

The solution to Eqs. (5) can be presented in the matrix form

$$\begin{pmatrix} A \\ B \\ C \end{pmatrix} = \frac{1}{\Delta}\begin{pmatrix} D_{11} & D_{12} & D_{31} \\ D_{21} & D_{22} & D_{32} \\ D_{31} & D_{32} & D_{33} \end{pmatrix} \cdot \begin{pmatrix} U_\xi \\ U_\eta \\ U_\zeta \end{pmatrix}, \qquad (6)$$

where the coefficients $D_{ij}$ are given by the expressions

$$D_{11} = -ik_\eta^2\left[k_\xi + \frac{1}{2}(k_2 - k_3)\sin2\varphi\right] - ik_\xi\beta_2\beta_3,$$

$$D_{12} = -ik_\eta(k_\eta^2 + \beta_2^2),$$

$$D_{13} = -ik_\eta^2[(k_2 - k_3)\cos^2\varphi + k_3] - ik_2\beta_2\beta_3,$$

$$D_{21} = -ik_\eta^2\left[k_\xi + \frac{1}{2}(k - k_3)\sin2\varphi\right] - ik_\xi\beta_1\beta_3,$$

$$D_{22} = -ik_\eta(k_\eta^2 + \beta_1^2),$$

$$D_{23} = -ik_\eta^2[(k_1 - k_3)\cos^2\varphi + k_3] + ik_1\beta_1\beta_3,$$

$$D_{31} = (k_\eta^2\cos^2\varphi + k_\xi^2)(k_1 - k_2)k_\eta,$$

$$D_{32} = (k_1 - k_2)\left[-k_\xi\beta_1\beta_2 + k_\eta^2\left(\frac{1}{2}(k_1 + k_2)\sin2\varphi\right.\right.$$

$$\left.\left. + k_\xi\cos2\varphi\right)\right], \quad D_{33} = (k_1 - k_2)k_\eta\sin\varphi$$

$$\times [-k_\eta^2 \cos\varphi + k_\eta(k_1\gamma_2 + k_\xi\beta_2)],$$

$$\Delta = (k_1 - k_2)\{-k_\xi\beta_1\beta_2\beta_3 + ik_\eta^4\cos\varphi$$

$$+ ik_\eta^2[\beta_3(\gamma_1\sin\varphi + \beta_2\cos\varphi) + \gamma_1\beta_1^2 - \gamma_2\beta_2^2]\}.$$

Solution (6) describes internal waves determined by the spectral coefficient $A(k_\xi, k_\eta)$ and periodic boundary layers of two types.

The internal boundary layer determined by the coefficient $B(k_\xi, k_\eta)$ is specific for stratified media.

The viscous boundary layer (spectral coefficient $C(k_\xi, k_\eta)$) is isopycnic and has an analogue in the case of homogeneous fluid, namely, the periodic Stokes flow [9].

The characteristic linear scale $\delta_N = \sqrt{\dfrac{\nu}{N}}$ entering into the expressions for the thicknesses of the two boundary layers is determined by both the kinematic viscosity and the buoyancy frequency. The thicknesses of the viscous boundary layer and of the internal boundary layer depend on the wave slope angle $\delta_v = \delta_N\sqrt{\dfrac{2}{\sin\theta}}$ of the wave, with the latter also depending on the slope angle of the radiating surface:

$$\delta_\varphi = \delta_N\sqrt{\frac{2\sin\theta}{|\mu|}}, \quad \mu = \sin^2\varphi - \sin^2\theta.$$

We have performed asymptotic estimations of integrals (3)–(5) for several wave sources having regular shapes, namely, an ellipse, circle, rectangle, and two touching rectangles moving in antiphase. The case of a frictional wave source corresponds to oscillations in the source plane (a similar two-dimensional problem was considered in [3, 9]). If displacements are orthogonal to the radiating surface, then piston or bipiston sources are realized that generate waves in perfect fluid.

For simplicity, we present the velocity vector as a sum of a wave component and a boundary-layer component, which are referred to the comoving and local coordinate systems, respectively: $\mathbf{v} = \mathbf{v}^w + \mathbf{v}^b$.

In the case of a small disk oscillating in its plane along the $\xi$ axis ($R \ll L_v = \left(\dfrac{\nu\Lambda}{N}\right)^{1/3}$, $r \gg R$), the wave component inside the cone of radiated waves is given by the expression

$$(v_x^w, v_y^w, v_z^w)$$

$$\approx A_1^w(-\sin 2\theta\cos\alpha, 2\cos^2\theta\cos\alpha, 2\sin^2\theta)F_1(p, q).$$

Here,

$$A_1^w = \frac{iu_0 R^2\delta_N}{4\sqrt{2\pi}|\mu|},$$

$$F_1(p, q) = \left(\cos\varphi\sin\theta - \sin\left(\frac{\pi}{4} - \alpha\right)\sin\varphi\cos\theta\right)$$

$$\times G\left(\frac{3}{2}, p, q\right), \quad G(n, p, q) = \frac{1}{\sqrt{p\sin\theta + q\cos\theta}}$$

$$\times \int\limits_0^{+\infty} dk_p k_p^n \exp\left(ik_p p - \frac{k_p^3\delta_N^2 q}{2\cos\theta}\right);$$

and the exponent $n$ is related to the type of wave source being used.

In this case, the boundary layers on the oscillating disk are completely separated. For the viscous boundary layer of the thickness $\delta_v$, the velocity is given by the relationships

$$v_y^b \approx -\frac{i-1}{\sqrt{2}}\frac{u_0 R\delta_N \sin^{3/2}\theta}{|\mu|\sin\varphi}\exp\left(\frac{i\zeta}{\delta_v} - \frac{\zeta}{\delta_v}\right)W_1,$$

where

$$W_1 = \int\limits_{-\infty}^{+\infty} \frac{k_\eta(k_\eta^2\cos\varphi + k_\xi^2)}{\sqrt{k_\xi^2 + k_\eta^2}}J_1(R\sqrt{k_\xi^2 + k_\eta^2})$$

$$\times W_v(k_\xi, k_\eta)dk_\xi dk_\eta,$$

$$W_v(k_\xi, k_\eta) = \frac{\sin\dfrac{k_\xi R}{2}\sin\dfrac{k_\eta R}{2}}{k_\eta^2\cos\varphi - k_\xi\sigma}\exp(ik_\xi\xi + ik_\eta\eta),$$

$$\sigma = \frac{1}{\mu}(k_\xi\cos\varphi\sin^2\theta + \cos\theta\sin\varphi\sqrt{k_\xi^2\sin^2\theta - k_\eta^2\mu}).$$

Similarly, for the internal boundary layer of the thickness $\delta_\varphi$, which depends on all the angular parameters of the problem,

$$v_x^b \approx \sqrt{2}u_0 R\cos\varphi\exp\left(\frac{i\zeta}{\delta_\varphi} - \frac{\zeta}{\delta_\varphi}\right)$$

$$\times \begin{cases} \dfrac{1}{R}, & \sqrt{\xi^2 + \eta^2} \leq R \\ 0, & \sqrt{\xi^2 + \eta^2} > R. \end{cases}$$

$$v_z^b \approx \sqrt{2}u_0 R\sin\varphi\exp\left(\frac{i\zeta}{\delta_\varphi} - \frac{\zeta}{\delta_\varphi}\right)$$

$$\times \begin{cases} \dfrac{1}{R}, & \sqrt{\xi^2 + \eta^2} \le R \\[2mm] 0, & \sqrt{\xi^2 + \eta^2} > R. \end{cases}$$

In the case of a disk oscillating in the transverse direction (piston source), the wave component takes the form

$$(v_x^{\mathrm{w}}, v_y^{\mathrm{w}}, v_z^{\mathrm{w}})$$

$$\approx A_2^{\mathrm{w}}(-\sin 2\theta \cos\alpha, \, 2\cos^2\theta\cos\alpha, \, 2\sin^2\theta) G\!\left(\frac{1}{2}, p, q\right),$$

where

$$A_2^{\mathrm{w}} = \frac{1 - i}{4\sqrt{\pi}} \frac{u_0 R^2}{\sqrt{\sin\theta}}.$$

For the viscous boundary layer,

$$v_y^{\mathrm{b}} \approx -\frac{i u_0 R}{\sqrt{2\pi}} \frac{\sin\varphi \sin^2\theta}{|\mu|} \exp\!\left(\frac{i-1}{\delta_v}\zeta\right) W_2$$

and for the internal boundary layer,

$$v_x^{\mathrm{b}} \approx -\frac{u_0 R}{\sqrt{2\pi}} \cos\varphi \exp\!\left(\frac{i\zeta}{\delta_\varphi} - \frac{\zeta}{\delta_\varphi}\right) W_3,$$

$$v_z^{\mathrm{b}} \approx -\frac{u_0 R}{\sqrt{2\pi}} \sin\varphi \exp\!\left(\frac{i\zeta}{\delta_\varphi} - \frac{\zeta}{\delta_\varphi}\right) W_3.$$

Here,

$$W_2 = \int_{-\infty}^{+\infty} \frac{k_\eta(k_{1,0}\sin\varphi + k_\xi\cos\varphi)}{\sqrt{k_\xi^2 + k_\eta^2}} J_1(R\sqrt{k_\xi^2 + k_\eta^2})$$

$$\times \, W_v(k_\xi, k_\eta)\, dk_\xi dk_\eta,$$

$$W_3 = \int_{-\infty}^{+\infty} \frac{k_\eta^2\cos\varphi + k_{1,0}\sigma}{\sqrt{k_\xi^2 + k_\eta^2}} J_1(R\sqrt{k_\xi^2 + k_\eta^2})$$

$$\times \, W_\delta(k_\xi, k_\eta)\, dk_\xi dk_\eta,$$

$$W_\delta(k_\xi, k_\eta) = \frac{\sin\dfrac{k_\xi R}{2}\sin\dfrac{k_\eta R}{2}}{k_\eta^2\cos\varphi - k_\xi\sigma} \exp\Bigg\{ ik_\xi$$

$$\times\left(\xi - \frac{\sin\varphi\cos\varphi}{\mu}\zeta\right) + ik_\eta\eta \Bigg\},$$

$$k_{1,0} = \frac{k_\xi\sin 2\varphi + 2\kappa\cos\theta}{2\mu},$$

$$\kappa = \sqrt{k_\xi^2\sin^2\theta - \mu k_\eta^2}.$$

Displacements $h(0, q)$ at the beam axis for two- [6] and three-dimensional sources ($a, b \ll L_v$, $q \gg a, b$)

| Source type | Strip of the thickness $a$ | Rectangle of size $a \times b$ | Disk of radius $R$ |
|---|---|---|---|
| Frictional | $\dfrac{\lambda_0 a}{\delta_N^{1/3}}\dfrac{1}{q^{2/3}}$ | $\dfrac{\lambda_0 ab}{\delta_N^{2/3}}\dfrac{1}{q^{4/3}}$ | $\dfrac{\lambda_0 R^2}{\delta_N^{2/3}}\dfrac{1}{q^{4/3}}$ |
| Piston | $\dfrac{\lambda_0 a}{\delta_N^{2/3}}\dfrac{1}{q^{1/3}}$ | $\dfrac{\lambda_0 ab}{\delta_N}\dfrac{1}{q}$ | $\dfrac{\lambda_0 R^2}{\delta_N}\dfrac{1}{q}$ |
| Bipiston | $\dfrac{\lambda_0 a}{\delta_N^{4/3}}\dfrac{a}{q^{2/3}}$ | $\dfrac{\lambda_0 ab}{\delta_N^{5/3}}\dfrac{b}{q^{4/3}}$ | – |

The conditions of validity of the linear approximation, namely, $\left(\dfrac{R^2}{q\delta_u} \ll 1\right)$ for the wave components and $\left(\dfrac{\delta_N}{\delta_u} \ll 1\right)$ for the boundary-layer components, coincide with the smallness condition for the relative thickness of the boundary layers (the quantity $\delta_u = \dfrac{v}{u_0}$ is the characteristic scale of the Prandtl boundary layer on the frictional wave source). In the case of a piston wave source, this condition takes the form $\dfrac{R^2}{q^{2/3}\delta_N^{1/3}\delta_u} \ll 1$ for the wave components and $\dfrac{\delta_N}{\delta_u} \ll 1$ for the boundary-layer components.

The $q$ dependences calculated for the displacement amplitude at the axis of a single-mode wave beam are listed in the table. The transversal scales $a$ and $b$ of the sources are assumed to be less than the viscous wave scale $L_v = \left(\dfrac{v\Lambda}{N}\right)^{1/3}$ related to the viscosity.

In all cases, the internal-wave amplitude in the far-field region depends on the dynamic scale $\lambda_0 = \dfrac{u_0}{N}$ and on the characteristic scale of the wave source boundary layers. The piston wave source is the most efficient among the wave sources under consideration. In order to take into account the nonlinearity of the problem, we should allow for the interaction between the boundary layers and the wave field. In this case, the generation of internal waves becomes possible even if the oscillation frequency of the source is higher than the buoyancy frequency [10].

## ACKNOWLEDGMENTS

## REFERENCES

1. J. Lighthill, *Waves in Fluids* (Cambridge Univ. Press, Cambridge, 1978; Mir, Moscow, 1981).
2. B. R. Sutherland and P. F. Linden, Phys. Fluids **14**, 721 (2002).
3. Yu. D. Chashechkin and Yu. V. Kistovich, Dokl. Akad. Nauk **355**, 54 (1997) [Phys.–Dokl. **42**, 377 (1997)].
4. D. G. Hurley and G. J. Keady, J. Fluid Mech. **351**, 119 (1997).
5. Yu. S. Il'inykh, Yu. V. Kistovich, and Yu. D. Chashechkin, Izv. Akad. Nauk, Fiz. Atmos. Okeana **35**, 649 (1999).
6. Yu. V. Kistovich and Yu. D. Chashechkin, Prikl. Mekh. Tekh. Fiz. **42** (1), 52 (2001).
7. D. D. Holm and Y. Kimura, Phys. Fluids A **3**, 1333 (1991).
8. A. Nayfeh, *Introduction to Perturbation Techniques* (Wiley, New York, 1981; Mir, Moscow, 1984).
9. G. G. Stokes, Trans. Cambridge Philos. Soc. **9**, Part 2, 8 (1851); *Mathematics and Physics Papers* (Cambridge, 1901), Vol. 3, pp. 1–141.
10. Yu. V. Kistovich and Yu. D. Chashechkin, Dokl. Akad. Nauk **382**, 772 (2002) [Dokl. Phys. **47**, 163 (2002)].

*Translated by V. Chechin*

=========== **MECHANICS** ===========

# Analytical Solutions of Navier–Stokes Equations for Axisymmetric and Plane Flows of a Viscous Incompressible Fluid

## A. V. Shcheprov

Presented by Academician A.A. Petrov September 4, 2003

Received September 8, 2003

Solving the Navier–Stokes equations with Cauchy data on a certain line, one can obtain, as in a particular case [1], systems of vortex structures in a fluid that are unknown to date. These equations for axisymmetric flows have singularities on the axis. The Kovalevskaya theorem for analytic data on the axis is generalized. In addition, the size of the domain where the solution is analytic is estimated, and an example is given. Similar analysis is also made for the plane case, when the Kovalevskaya theorem is valid in its original form, and the size of the domain where the solution is analytic is estimated.

First, we consider axisymmetric flows. The current function $\varphi(x, r)$ of the cylindrical coordinates $(x, r)$ is introduced as

$$d\varphi = r v_x dr - r v_r dx,$$

where $v_x$ and $v_r$ are axial and radial velocity components multiplied by the Reynolds number, respectively. In this work, flow curl around the symmetry axis is limited by the potential dependence, when the azimuthal velocity component has the form $V = \dfrac{W}{r}$, where $W$ is an arbitrary constant. In terms of the differential operator

$$L = \frac{\partial^2}{\partial x^2} + \frac{\partial^2}{\partial r^2} - \frac{1}{r}\frac{\partial}{\partial r}$$

and auxiliary function $\sigma(x, r)$, the Navier–Stokes equation is represented in the form

$$L\varphi = \sigma, \quad L\sigma = \frac{1}{r}\left(\frac{\partial\varphi}{\partial r}\frac{\partial\sigma}{\partial x} - \frac{\partial\varphi}{\partial x}\frac{\partial\sigma}{\partial r}\right) + \frac{2\sigma}{r^2}\frac{\partial\varphi}{\partial x}. \quad (1)$$

*Computer Center, Russian Academy of Sciences,*
*ul. Vavilova 40, Moscow, 117333 Russia*

A solution to system (1) is sought in the form of the series

$$\varphi(x, r) = \sum_{m=0}^{\infty} f_m(x) r^m, \quad \sigma(x, r) = \sum_{m=0}^{\infty} \omega_m(x) r^m. \quad (2)$$

The substitution of expansions (2) into Eqs. (1) gives

$$\sum_{m=0}^{\infty} [f_m'' r^m + m(m-2) f_m r^{m-2}] = \sum_{m=0}^{\infty} \omega_m r^m,$$

$$\sum_{m=0}^{\infty} [\omega_m'' r^m + m(m-2)\omega_m r^{m-2}] \quad (3)$$

$$= \sum_{k,l=0}^{\infty} [(2-l)f_k'\omega_l + k f_k \omega_l'] r^{k+l-2},$$

where prime means the derivative of a function with respect to its argument.

For analytic solutions, $\varphi = \dfrac{\partial\varphi}{\partial r} = 0$ on the symmetry axis, and it is necessary that $f_0 = f_1 \equiv 0$. Equating the sums of coefficients of the same $r$ powers in Eqs. (3), we arrive at the relations $\omega_0 = 0$ and $f_l = \omega_l \equiv 0$ for $l = 2n - 1$, $n = 1, 2, \ldots$. According to Eqs. (3), the coefficients $f_{2n}$ and $\omega_{2n}$ of even $r$ powers in series (2) for $n \geq 2$ satisfy the chain of equations

$$f_{2n} = \frac{1}{4n(n-1)}(\omega_{2n-2} - f_{2n-2}''), \quad (4)$$

$$\omega_{2n} = \frac{1}{2n(n-1)}\sum_{k=1}^{n-1} [(k+1-n)f_{2k}'\omega_{2n-2k}$$

$$+ k f_{2k}\omega_{2n-2k}'] - \frac{1}{4n(n-1)}\omega_{2n-2}''.$$

In this case, the functions $f_2(x)$ and $\omega_2(x)$ can be chosen arbitrarily. System (4) for given $f_2$ and $\omega_2$ functions,

which are a part of the Cauchy data for $r = 0$, enables one to construct the unique series

$$\varphi = \sum_{n=1}^{\infty} f_{2n}(x) r^{2n}, \quad \sigma = \sum_{n=1}^{\infty} \omega_{2n}(x) r^{2n}, \quad (5)$$

which, as will be shown below, under certain conditions imposed on $f_2$ and $\omega_2$, provide analytic solutions to Eq. (1) in a certain region of $(x, r)$.

The functions $f_2(x)$ and $\omega_2(x)$ are assumed to be defined for $x \in X$, infinitely differentiable, and satisfy the inequalities

$$\left| f_2^{(s)}(x) \right| \leq \frac{1}{\beta a} \quad \text{and} \quad \left| \omega_2^{(s)}(x) \right| \leq \frac{1}{\beta a},$$

where $s$ is the order of derivatives and $0 < a \leq 2$ and $\beta \geq 2$ are constants. We will show that the estimates

$$\left| f_{2n}^{(s)}(x) \right| \leq \frac{n^{s-1}}{\beta a^n}, \quad \left| \omega_{2n}^{(s)}(x) \right| \leq \frac{n^{s-1}}{\beta a^n}, \quad s = 0, 1, \ldots \quad (6)$$

are valid for any $n \geq 2$.

First, infinite differentiability of the functions $f_{2n}(x)$ and $\omega_{2n}(x)$ follow from Eqs. (4). Relations (6) will be proved by induction. For $n = 2$, we have

$$\left| f_4^{(s)} \right| \leq \frac{1}{8} \left( \left| f_2^{(s+2)} \right| + \left| \omega_2^{(s)} \right| \right) \leq \frac{1}{8} \left( \frac{1}{\beta a} + \frac{1}{\beta a} \right)$$

$$\leq \frac{2^s}{2} \frac{1}{\beta a^2} \frac{a}{2} \leq \frac{2^{s-1}}{\beta a^2}.$$

Using the equality $\displaystyle\sum_{p=0}^{s} C_s^p = 2^s$ for the binomial coefficients $C_s^p = \dfrac{s!}{p!(s-p)!}$, we obtain

$$\left| \omega_4^{(s)} \right| \leq \frac{1}{8} \left| \omega_2^{(s+2)} \right| + \frac{1}{4} \left| (f_2 \omega_2')^{(s)} \right| \leq \frac{1}{8} \left| \omega_2^{(s+2)} \right|$$

$$+ \frac{1}{4} \sum_{p=0}^{s} C_s^p \left| f_2^{(p)} \right| \left| \omega_2^{(s-p+1)} \right| \leq \frac{1}{8\beta a} + \frac{2^s}{4\beta^2 a^2}$$

$$= \frac{2^{s-1}}{\beta a^2} \left( \frac{a}{8 \cdot 2^{s-1}} + \frac{1}{2\beta} \right) < \frac{2^{s-1}}{\beta a^2}.$$

Assuming that these estimates are valid for $f_{2l}^{(s)}$ and $\omega_{2l}^{(s)}$, $l \leq n - 1$, and using the equality

$\displaystyle\sum_{p=0}^{s} C_s^p k^p (n-k)^{s-p} = n^s$, we arrive at the following estimates for $l = 2n$:

$$\left| f_{2n}^{(s)} \right| \leq \frac{1}{4n(n-1)} \left( \left| f_{2n-2}^{(s+2)} \right| + \left| \omega_{2n-2}^{(s)} \right| \right) \leq \frac{1}{4n(n-1)}$$

$$\times \left( \frac{(n-1)^{s+1}}{\beta a^{n-1}} + \frac{(n-1)^{s-1}}{\beta a^{n-1}} \right) \leq \frac{n^{s-1}}{\beta a^n} \left( \frac{a}{4} + \frac{a}{4n^2} \right) < \frac{n^{s-1}}{\beta a^n},$$

$$\left| \omega_{2n}^{(s)} \right| \leq \frac{1}{4n(n-1)} \left| \omega_{2n-2}^{(s+2)} \right| + \frac{1}{2n(n-1)}$$

$$\times \left| \sum_{k=1}^{n-1} \left\{ (1+k-n) \sum_{p=0}^{s} C_s^p f_{2k}^{(p+1)} \omega_{2n-2k}^{(s-p)} \right. \right.$$

$$\left. \left. + k \sum_{p=0}^{s} C_s^p f_{2k}^{(p)} \omega_{2n-2k}^{(s-p+1)} \right\} \right| \leq \frac{(n-1)^{s+1}}{4n(n-1)\beta a^{n-1}}$$

$$+ \frac{1}{2n(n-1)} \sum_{k=1}^{n-1} \left\{ (n-k-1) \sum_{p=0}^{s} C_s^p \frac{k^p}{\beta a^k} \frac{(n-k)^{s-p}}{(n-k)\beta a^{n-k}} \right.$$

$$\left. + k \sum_{p=0}^{s} C_s^p \frac{k^p}{k\beta a^k} \frac{(n-k)^{s-p}}{\beta a^{n-k}} \right\} \leq \frac{n^{s-1}}{4\beta a^{n-1}}$$

$$+ \frac{2n^s(n-1)}{2n(n-1)\beta^2 a^n} = \frac{n^{s-1}}{\beta a^n} \left( \frac{a}{4} + \frac{1}{\beta} \right) \leq \frac{n^{s-1}}{\beta a^n},$$

$$\sum_{p=0}^{s} C_s^p k^p (n-k)^{s-p} = n^s.$$

Thus, estimates (6) have been proved.

Under the above assumptions for the functions $f_2(x)$ and $\omega_2(x)$, series (5) converge uniformly in the domain $\{x \in X, 0 \leq r < \sqrt{a}\}$. To prove this statement, we first consider the series for $\varphi$. According to estimates (6),

$$\left| \sum_{n=1}^{\infty} f_{2n} r^{2n} \right| \leq \sum_{n=1}^{\infty} \left| f_{2n} \right| r^{2n} \leq \sum_{n=1}^{\infty} \frac{r^{2n}}{\beta n a^n}.$$

The limit of the ratio of two sequential terms of the last series for $n \to \infty$ is equal to $\dfrac{r^2}{a}$. Therefore, according to the D'Alembert ratio test, this series converges if $\dfrac{r^2}{a} < 1$. Thus, the original series for $\varphi$ converges absolutely and uniformly for $0 \leq r < \sqrt{a}$. The uniform convergence

of the series for $\sigma$ in the range $0 \le r < \sqrt{a}$ is proved similarly.

In the domain $\{x \in X, 0 \le r < \sqrt{a}\}$, series (5) are infinitely differentiable with respect to both variables. This statement is proved by considering the series with the terms

$$2n(2n-1) \cdot \ldots \cdot (2n-s+1) f_{2n}^{(m)} r^{2n-s},$$

which is obtained from the series for $\varphi$ by its differentiation with respect to $x$ and $r$ by $m$ and $s$ times, respectively. According to estimates (6),

$$\left| \sum_{2n-s \ge 0} 2n(2n-1) \cdot \ldots \cdot (2n-s+1) f_{2n}^{(m)} r^{2n-s} \right|$$

$$\le \sum_{2n-s \ge 0} 2n(2n-1) \cdot \ldots \cdot (2n-s+1) \frac{n^{m-1}}{\beta a^n} r^{2n-s}.$$

The limit of the ratio of two sequential terms of the last series for $n \to \infty$ is equal to $\dfrac{r^2}{a}$. Thus, according to the D'Alembert ratio test, this series converges if $\dfrac{r^2}{a} < 1$. Thus, the original series converges uniformly for $0 \le r < \sqrt{a}$. Therefore, the series for $\varphi$ is differentiable. A similar statement is valid for $\sigma$.

Thus, it is proved that series (5) provide the unique analytic solution to Navier–Stokes equations (1) in the range $0 \le r < \sqrt{a}$.

The above procedure of constructing analytic solutions can be used to theoretically analyze viscous flows, which attract the constant attention of specialists in hydrodynamics. Hill-type vortex structures are among these flows and are considered in numerous works. In particular, infinite chains of Hill vortex structures satisfying Navier–Stokes equations and Euler and Stokes equations were analytically described in [2]. Axisymmetric structures in the form of a pair of separated vortices, pair of merged vortices, vortex chain, etc., were exemplified in [1]. These results were obtained on the basis of the Navier–Stokes equations with the potential curl of flows around the symmetry axis when $\sigma(x, r) = cr^2$, where $c$ is an arbitrary constant. This class of flows is a particular case of analytic solutions to Eqs. (1), which are studied in this work. Indeed, the second of Eqs. (4) for $\omega_2 = c$ shows that $\omega_{2n}(x) \equiv 0$ for $n \ge 2$, and the functions $f_{2n}(x)$ are expressed in terms of the $(2n-2)$-order derivatives of the function $f_2(x)$. In this case, the function $f_4(x)$ also depends on $c$. According to analysis made in [1], the series for $\varphi$ converges uniformly over the entire $r$ region. The solutions found above sat-
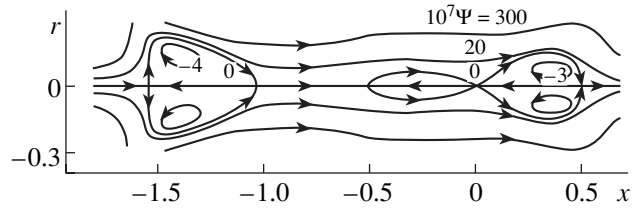


**Figure.**

isfy not only the Navier–Stokes equations but also the Stokes equations (as well as the equations for an ideal fluid). Pairs of separated Hill-type vortex structures were also obtained experimentally [3, 4].

The results of this work enable one to continue studying vortex structures satisfying only the Navier–Stokes equations. We analyze an example with the functions

$$f_2 = \frac{1}{300} x^2 \left( x - \frac{1}{2} \right) \left( x + \frac{1}{2} \right) (x + 1) \left( x + \frac{3}{2} \right),$$

$$\omega_2 = \frac{1}{70} (-5x^4 - 5x^3 + 3x^2 - x + 5)$$

in the domain $-1.75 \le x \le 0.75$ and $0 \le r \le 0.3$. Convergent series (5) with coefficients obtained from the chain of Eqs. (4) are replaced by the partial sums, whose convergence rate to the solution is estimated in terms of the parameter

$$\delta_m = \frac{\max |s_m - s_{m-1}|}{\max |s_m|},$$

where $s_m$ is the $m$-term partial sum of expansion for $\varphi(x, r)$ or $\sigma(x, r)$. Maxima are determined over the entire flow range. Partial sums of the series for $\varphi$ are equal to $\delta_3 = 9.43 \times 10^{-2}$, $\delta_4 = 7.06 \times 10^{-4}$, and $\delta_5 = 6.75 \times 10^{-6}$. The figure shows the current contours for this flow that correspond to $s_5$. The first two of the three vortices touch each other on the $r = 0$ axis for $x = 0$, and the left vortex is isolated.

Then, we analyze plane flows of a viscous incompressible fluid, which are described by the equations

$$\Delta \psi = \omega, \quad \Delta \omega = \frac{\partial \psi}{\partial y} \frac{\partial \omega}{\partial x} - \frac{\partial \psi}{\partial x} \frac{\partial \omega}{\partial y} \qquad (7)$$

in the Cartesian coordinates $x$ and $y$. Here, $\psi$ is the current function introduced as $d\psi = u_x d_y - u_y d_x$, where $u_x$ and $u_y$ are the velocity components multiplied by the Reynolds number, $\omega$ is the vortex function, and $\Delta$ is the Laplacian.

A solution is sought in the form

$$\psi = \sum_{n=0}^{\infty} \psi_n(x) y^n, \quad \omega = \sum_{n=0}^{\infty} \gamma_n(x) y^n. \qquad (8)$$

Substituting Eq. (8) into Eq. (7) and equating coefficients of the same $y$ powers, we arrive at the chain of equations for $n \geq 2$:

$$\psi_n = \frac{1}{n(n-1)}(\gamma_{n-2} - \psi''_{n-2}), \qquad (9)$$

$$\gamma_n = -\frac{1}{n(n-1)}\gamma''_{n-2} + \frac{1}{n(n-1)}$$

$$\times \sum_{k=0}^{n-1}[k\psi_k\gamma'_{n-k-1} - (n-k-1)\psi'_k\gamma_{n-k-1}].$$

Functions $\psi_0$, $\psi_1$, $\gamma_0$, and $\gamma_1$ are arbitrary. Their specification on the $x$ axis is equivalent to the specification of the functions $\psi$, $\frac{\partial\psi}{\partial y}$, $\omega$, and $\frac{\partial\omega}{\partial y}$ for $y = 0$. Therefore, the above equalities can be treated as a description of the Cauchy problem with data on the $y = 0$ line. According to the Cauchy–Kovalevskaya theorem, this problem has the unique analytic solution near $y = 0$. The concept of solving Navier–Stokes equations (7) by solving the Cauchy problem was developed, e.g., in [5, 6]. In [5], Cauchy data were taken from the solutions of Stokes equations. Only the first few terms are retained in expansions (8) for the functions $\psi$ and $\omega$. From these partial sums, boundary conditions at the boundary of the testing domain are obtained. Under these conditions, the Navier–Stokes equations are numerically solved, and the results are compared with those provided by partial sums over the entire domain. This procedure makes it possible to estimate the convergence of series in the taken region and the accuracy of both solutions.

The Kovalevskaya theorem does not provide information about the convergence radius of series representing analytic solutions to the Navier–Stokes equations. Therefore, for practical use of chains of equalities (9) to construct expansions (8), it is necessary to estimate the convergence domains.

Let the functions $\psi_0$, $\psi_1$, $\gamma_0$, and $\gamma_1$ be infinitely differentiable, so that

$$\left|\psi_0^{(s)}(x)\right| \leq \frac{1}{\beta a}, \quad \left|\psi_1^{(s)}(x)\right| \leq \frac{1}{\beta a},$$

$$\left|\gamma_0^{(s)}(x)\right| \leq \frac{1}{\beta a}, \text{ and } \left|\gamma_1^{(s)}(x)\right| \leq \frac{1}{\beta a},$$

where $s$ is the order of derivatives and $0 < a \leq 1/2$ and $\beta \geq 4$ are constants. Then, for $n \geq 2$, we have the inequalities

$$\left|\psi_n^{(s)}(x)\right| \leq \frac{n^{s-1}}{\beta a^n}, \quad \left|\gamma_n^{(s)}(x)\right| \leq \frac{n^{s-1}}{\beta a^n}, \qquad (10)$$

$$s = 0, 1, \dots.$$

Estimates (10) are proved by induction, and this proof is similar to that for estimates (6) in the axisymmetric case. For $n = 2$,

$$\left|\psi_2^{(s)}\right| \leq \frac{1}{2}(\left|\psi_0^{(s+2)}\right| + \left|\gamma_0^{(s)}\right|) \leq \frac{1}{2}\left(\frac{1}{\beta a} + \frac{1}{\beta a}\right) \leq \frac{2^{s-1}}{\beta a^2},$$

$$\left|\gamma_2^{(s)}\right| \leq \frac{1}{2}\left|\gamma_0^{(s+2)}\right| + \frac{1}{2}\sum_{p=0}^{s}C_s^p(\left|\psi_1^{(p)}\gamma_0^{(s-p+1)}\right|$$

$$+ \left|\psi_0^{(p+1)}\gamma_1^{(s-p)}\right|) \leq \frac{1}{2\beta a} + \frac{2^s}{\beta^2 a^2} \leq \frac{2^{s-1}}{\beta a^2}.$$

Under the assumption that inequality (10) is valid to the index $n - 1$, we obtained the estimates

$$\left|\psi_n^{(s)}\right| \leq \frac{1}{n(n-1)}(\left|\psi_{n-2}^{(s+2)}\right| + \left|\gamma_{n-2}^{(s)}\right|) \leq \frac{1}{n(n-1)}$$

$$\times\left(\frac{(n-2)^{s+1}}{\beta a^{n-2}} + \frac{(n-2)^{s-1}}{\beta a^{n-2}}\right) \leq \frac{n^{s-1}}{\beta a^n}\left(a^2 + \frac{a^2}{n^2}\right) < \frac{n^{s-1}}{\beta a^n},$$

$$\left|\gamma_n^{(s)}\right| \leq \frac{1}{n(n-1)}\left|\gamma_{n-2}^{(s+2)}\right| + \frac{1}{n(n-1)}\left\{\sum_{k=1}^{n-2}k\sum_{p=0}^{s}C_s^p\right.$$

$$\times\left|\psi_k^{(p)}\gamma_{n-k-1}^{(s-p+1)}\right| + (n-1)\sum_{p=0}^{s}C_s^p\left|\psi_{n-1}^{(p)}\gamma_0^{(s-p+1)}\right|$$

$$+ \sum_{k=1}^{n-2}(n-k-1)\sum_{p=0}^{s}C_s^p\left|\psi_k^{(p+1)}\gamma_{n-k-1}^{(s-p)}\right|$$

$$+ (n-1)\sum_{p=0}^{s}C_s^p\left|\psi_0^{(p+1)}\gamma_{n-1}^{(s-p)}\right|\right\} \leq \frac{(n-2)^{s+1}}{n(n-1)\beta a^{n-2}}$$

$$+ \frac{1}{n(n-1)}\left\{\sum_{k=1}^{n-2}k\sum_{p=0}^{s}C_s^p\frac{k^p}{k\beta a^k}\frac{(n-k-1)^{s-p}}{\beta a^{n-k-1}}\right.$$

$$+ (n-1)\sum_{p=0}^{s}C_s^p\frac{(n-1)^p}{(n-1)\beta a^{n-1}}\frac{1}{\beta a}$$

$$+ \sum_{k=1}^{n-2}(n-k-1)\sum_{p=0}^{s}C_s^p\frac{k^p}{\beta a^k}\frac{(n-k-1)^{s-p}}{(n-k-1)\beta a^{n-k-1}}$$

$$+ (n-1)\sum_{p=0}^{s}C_s^p\frac{1}{\beta a}\frac{(n-1)^{s-p}}{(n-1)\beta a^{n-1}}\right\}$$

$$\leq \frac{n^{s-1}}{\beta a^{n-2}} + \frac{2n^{s-1}}{\beta^2 a^{n-1}} + \frac{2n^{s-1}}{\beta^2 a^n(n-1)}$$

$$= \frac{n^{s-1}}{\beta a^n}\left(a^2 + \frac{2a}{\beta} + \frac{2}{\beta(n-1)}\right) \leq \frac{n^{s-1}}{\beta a^n}.$$

Using the above estimates, one can easily show that series (8) converge uniformly in the domain $\{x \in X, 0 \leq r < \sqrt{a}\}$. To this end, it is sufficient to reproduce the corresponding proof for the axisymmetric case. In this domain, series (8) are infinitely differentiable in terms of both variables.

Expansions (8) are carried out with respect to the variable $y$. Similar results are obtained for expansion with respect to $x$.

## ACKNOWLEDGMENTS

## REFERENCES

1. Yu. D. Shmyglevskiĭ and A. V. Shcheprov, Dokl. Akad. Nauk **393**, 489 (2003) [Dokl. Phys. **48**, 685 (2003)].

2. Yu. D. Shmyglevskiĭ, *Analytical Study of the Gas and Liquid Dynamics* (Editorial, Moscow, 1999).

3. S. Leibovich, Annu. Rev. Fluid Mech. **10**, 221 (1978).

4. M. Escudier, Prog. Aerosp. Sci. **25**, 189 (1988).

5. Yu. D. Shmyglevskiĭ and A. V. Shcheprov, Izv. Akad. Nauk, Ser. Mekh. Zhidk. Gaza, No. 5, 12 (2002).

6. B. V. Pal'tsev and Yu. D. Shmyglevskiĭ, Izv. Akad. Nauk, Ser. Mekh. Zhidk. Gaza, No. 2, 76 (2002).

*Translated by R. Tyapaev*

===== **MECHANICS** =====

# An Exact Solution to the Problem of Combustion Wave Propagation

## A. E. Dubinov, I. D. Dubinova, and S. K. Saĭkov

Presented by Academician G.G. Chernyĭ, October 17, 2003

In [1], a one-dimensional model for the propagation of a steady-state combustion wave in an infinite medium was considered in the continuum approximation. The model is based on the boundary value problem for a stationary temperature distribution in the presence of a source. Within the framework of this model, the following equation for the dimensionless mass rate $\mu$ of combustion was derived:

$$k\tau = \frac{1}{2}\left(1 - \frac{1}{\sqrt{1 + \frac{4k}{\mu^2}}}\right)\left\{1 - \exp\left[-\frac{\mu^2}{2}\left(1 + \sqrt{1 + \frac{4k}{\mu^2}}\right)\right]\right\}. \tag{1}$$

Here, $\tau$ is the dimensionless reduced ignition temperature and $k$ is the heat-loss factor. Below, Eq. (1) was analyzed numerically.

In this study, we have managed to derive an exact explicit solution to Eq. (1). This solution has two branches corresponding to the hysteresis loop of the mass rate of combustion:

$$\mu_{1,2} = \begin{cases} \dfrac{\left\{2k\tau - 1 - \tau W_0\left[-\frac{1}{\tau}\exp\frac{2k\tau - 1}{\tau}\right]\right\}\sqrt{\tau - k\tau^2 + W_0\left[-\frac{1}{\tau}\exp\frac{2k\tau - 1}{\tau}\right]}}{k\tau^2 - \tau - \tau^2 W_0\left[-\frac{1}{\tau}\exp\frac{2k\tau - 1}{\tau}\right]} \\[2em] \dfrac{\left\{2k\tau - 1 - \tau W_{-1}\left[-\frac{1}{\tau}\exp\frac{2k\tau - 1}{\tau}\right]\right\}\sqrt{\tau - k\tau^2 + W_{-1}\left[-\frac{1}{\tau}\exp\frac{2k\tau - 1}{\tau}\right]}}{k\tau^2 - \tau - \tau^2 W_{-1}\left[-\frac{1}{\tau}\exp\frac{2k\tau - 1}{\tau}\right]}. \end{cases} \tag{2}$$

Here, the subscripts 1 and 2 correspond to the high and low mass rates of combustion, respectively, and $W_0(x)$ and $W_{-1}(x)$ are the positive and negative branches of the Lambert $W$ function [2]. This function is inverse to the function $y = x\exp x$.

The critical combustion regime parameters, i.e., the extremum of the function $\tau(\mu)$, can be found from the equation $\frac{d\tau}{d\mu} = 0$:

*All-Russia Research Institute of Experimental Physics,*
*Russian Federal Nuclear Center, Sarov,*
*Nizhni Novgorod oblast, 607200 Russia*
*e-mail: dubinov@ntc.vniief.ru*

$$\frac{8\left\{1 - \exp\left[-\frac{\mu^2}{2}\left(1 + \sqrt{1 + \frac{4k}{\mu^2}}\right)\right]\right\}}{\mu^3\left(1 + \frac{4k}{\mu^2}\right)^{3/2}}$$

$$+ \frac{2}{k}\left(1 - \frac{1}{\sqrt{1 + \frac{4k}{\mu^2}}}\right)\left[\frac{2k}{\mu\sqrt{1 + \frac{4k}{\mu^2}}} - \mu\left(1 + \sqrt{1 + \frac{4k}{\mu^2}}\right)\right] \tag{3}$$

$$\times \exp\left[-\frac{\mu^2}{2}\left(1 + \sqrt{1 + \frac{4k}{\mu^2}}\right)\right] = 0.$$

In [1], this equation was analyzed only qualitatively. However, it can be solved exactly, and the solution is

$$\mu_{cr} = \frac{W_{-1}[-\exp(-2k - 1)] + 2k + 1}{W_{-1}[-\exp(-2k - 1)] + k + 1}$$

$$\times \sqrt{-W_{-1}[-\exp(-2k - 1)] - k - 1}. \tag{4}$$

Substituting solution (4) into Eq. (1), we find $\tau_{cr}$:

$$\tau_{cr} = \frac{1 - S(k)}{2kS(k)}$$

$$\times \left\{\exp\frac{[W_{-1}(-\exp(-2k - 1)) + 2k + 1][1 + S(k)]}{2S^2(k)} - 1\right\}, \tag{5}$$

where

$$S(k) = \frac{W_{-1}[-\exp(-2k - 1)] + 1}{W_{-1}[-\exp(-2k - 1)] + 2k + 1}. \tag{6}$$

Relationships (4) and (5) yield the equation for the extremal in the parametric form. The extremal is shown in the figure. Since $\frac{d\mu}{d\tau} > 0$, the lower branch of the dependence $\mu(\tau)$ is unstable and, therefore, the extremal determines the lower bound of stationary-combustion regimes. It follows from the solution found that the extremal dependence is nonmonotone. Indeed, the quantity $\mu_{cr}$ decreases not only with decreasing heat
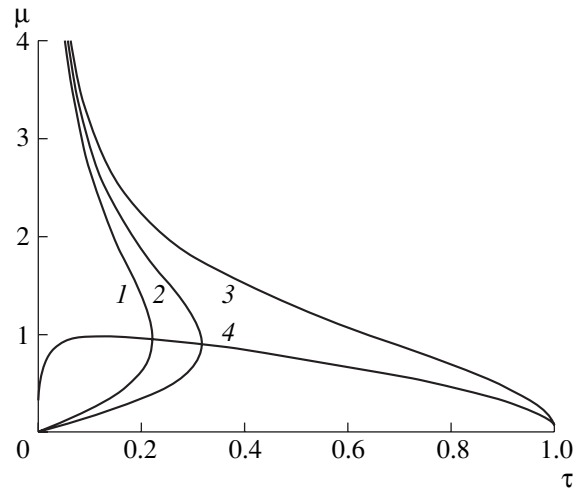


Dimensionless mass rate of combustion as a function of the dimensionless reduced temperature for various heat-loss factors: $k =$ (*1*) 1; (*2*) 0.5; (*3*) 0. Curve *4* is the extremal.

losses ($k \to 0$) but also as heat losses tend to infinity ($k \to \infty$). (Such a behavior of the extremal was not revealed in [1] under the qualitative analysis.) This feature suggests that, in the case of large heat losses, the mass rate of stationary combustion can be rather low.

Thus, the use of the Lambert $W$ function allows us, using the continuum approximation, to perform a complete and exact analysis of the problem on the propagation of a stationary combustion wave in an infinite medium.

## REFERENCES

1. F. A. Williams, *Combustion Theory* (Addison-Wesley, Reading, 1965; Nauka, Moscow, 1971).
2. R. M. Corless, G. H. Gonnet, D. E. J. Hare, *et al.*, Adv. Comput. Math. **5**, 329 (1996).

*Translated by V. Chechin*

===== **MECHANICS** =====

# Evolution of the Back Flow in the Case of Pulsed Evaporation into Vacuum

## A. A. Morozov

Presented by Academician A.K. Rebrov September 19, 2003

Received October 3, 2003

Studies of pulsed evaporation are of interest for various applications such as ablation of a substance under the action of a pulse of laser radiation [1, 2] and of ion [3] or electron [4] beams; pulsed plasma thrusters [5]; and pulsed thermal sources [6]. When evaporated particles fly apart, as a result of collisions in the created vapor cloud, the particles can come back to the evaporation surface, thereby forming a back flow of the mass, momentum, and energy. The intensity of the back flow depends on the amount of an evaporated substance. This intensity can vary from zero for the collisionless expansion in the case of desorption (when the amount of the evaporated substance is much less than one monolayer) to a value corresponding to the back flow in the case of the stationary evaporation into vacuum (16.3% according to the results of numerical calculation of [7]). In this case, the energy of backscattering particles can be noticeably lower than that of evaporated particles.

Molecules continue to return to the surface for a long time upon completion of the pulse, which results in a significant increase in the back flow. It was demonstrated in [8] that, in the case of intense evaporation, from 10 to 43% of particles (depending on the number of internal degrees of freedom of molecules) can return to the surface already after pulse termination.

Thus, the intensity of the back flow during the presence of a pulse and after it has ended can be significant. In other words, for adequately modeling the evaporation process, it is necessary to allow for the back flow. We should note that, at the present time, data on the intensity of the back flow in the entire range of the evaporation rates are virtually absent.

The problem of determining the back-flow intensity can be solved by the method of direct Monte Carlo simulation. This method was widely employed in simulating both stationary [7, 9] and pulsed [10–14] evaporation into vacuum. However, in these papers, the dependence of the back flow on the evaporation intensity was not determined.

In the present study, we report the results obtained by the method of the direct Monte Carlo simulation [15] of back flows as a function of the Knudsen number in the course of evaporation and upon its completion within a wide range of the evaporation intensity when the flow being formed changes from the collisionless to the continual one.

We solve the one-dimensional problem on the evaporation of particles from a plane surface with the subsequent expansion into vacuum. The evaporation occurs in accordance with the diffusion law at an energy corresponding to the temperature $T_0$ of the surface. For the pulse duration time $\tau$, the constant particle flux is given.

This flux is equal to $\Psi = \dfrac{n_0 u_T}{4}$, where $n_0$ is the saturated-vapor density at the temperature $T_0$, $u_T = \sqrt{\dfrac{8kT_0}{\pi m}}$, $m$ is the molecular mass, and $k$ is the Boltzmann constant. All particles that have returned to the evaporation surface are condensed. A monatomic gas is considered. For describing atomic interactions, the hard sphere model [15] is used. The Knudsen number $\mathrm{Kn} = \dfrac{\lambda_0}{u_T \tau}$ [12] is convenient to employ as a criterion uniquely determining the flow being formed. (Here, $\lambda_0 = \dfrac{1}{n_0 \sigma \sqrt{2}}$ is the molecule mean free path in the saturated vapor and $\sigma$ is the collision cross section for molecules.) This number, in fact, determines the degree of the vapor cloud rarefaction to the moment of the pulse end.

Particular attention is paid to the determination of the back-flow intensity at times much exceeding the pulse action time. The calculation time for which we traced the cloud expansion dynamics was set equal to $10^7 \tau$. The expansion of the cloud in such a long time interval is characterized by both a large density drop in the cloud core and significant gradients of parameters at the cloud front. Therefore, we used an adaptive grid for

*Kutateladze Institute of Thermophysics, Siberian Division,*
*Russian Academy of Sciences,*
*pr. Akademika Lavrent'eva 1, Novosibirsk, 630090 Russia*
*e-mail: morozov@itp.nsc.ru*

the calculations. For constructing this grid, we have performed a preliminary calculation with a small number of particles and a large time step. Based on the results of this preliminary calculation, we evaluated spatial density profiles at different moments of time, which were used furthermore for constructing the adaptive grid. It was constructed in such a manner that the cell size would not exceed 0.25 of the local mean free path. The time step was chosen according to the condition that it not exceed the mean local time between collisions. Since the density of the cloud drops by several orders of magnitude during its expansion, the cell size and the time step permanently increased by the same orders of magnitude. The size of the domain being modeled permanently increased in the process of the calculation, so that particles could leave the domain only upon returning to the evaporation surface and upon being absorbed by it. The number of particles in the calculation reached $5 \times 10^6$.

For testing the program package, calculations of the stationary and pulsed evaporation into vacuum were performed for the conditions presented in [7, 12]. The calculated results are consistent with those obtained in [7, 12].

The calculations were carried out for Knudsen numbers $Kn = 10^{-4}$–$10^2$. The time evolution of the back flow $\beta$ for different values of $Kn$ is shown in Fig. 1. At each moment of time, the back flow $\beta$ was determined as the ratio of the total number of particles returned to and absorbed on the wall to the total number of evaporated particles. The number of returned particles is directly proportional to the number of collisions in the cloud and, correspondingly, to the mass of the evaporated substance. As the Knudsen number unambiguously determines the amount of the evaporated substance, we expected that a single value of the back-flow intensity exists for each Knudsen number. However, in contrast to our suggestions, for an arbitrary $Kn < 0.1$, the value of $\beta$ tends to the common limiting value close to ~27.5%.

The maximum value of the back-flow intensity during the time of the pulse action corresponds to that of the back flow for the stationary evaporation and equals 16.3% [7]. After the evaporation has finished, a strong rise of the back-flow intensity, which is associated with ceasing evaporation of particles, is observed. We assume that the stationary evaporation under study with a constant evaporation rate, which is not typical for actual conditions, does not affect the intensity of the back flow at long times. This can be explained by the fact that, owing to collisions in the vapor cloud, particles "forget" their initial distribution characteristic of evaporation [13].

The dependence of the quantity $\beta$ on the Knudsen number makes it possible to note certain not evident results (Fig. 2). This dependence has a weakly pronounced maximum in the vicinity of $Kn = 0.02$, which
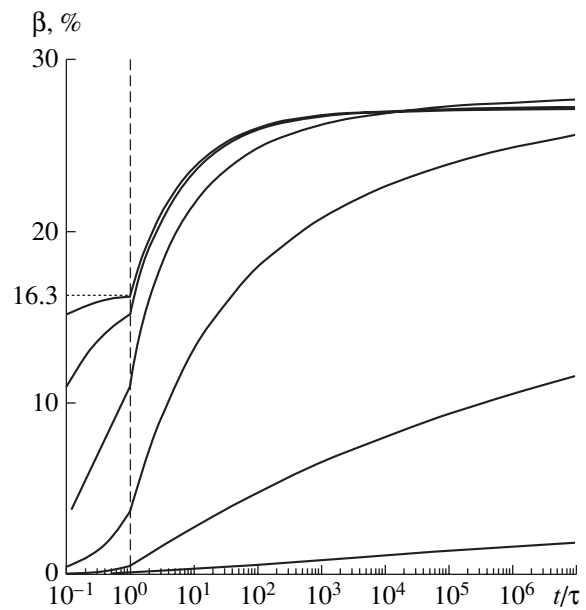


**Fig. 1.** Time evolution of the back flow $\beta$ for the Knudsen numbers (from top to bottom) $Kn = 0.0001, 0.001, 0.01, 0.1, 1,$ and $10$.
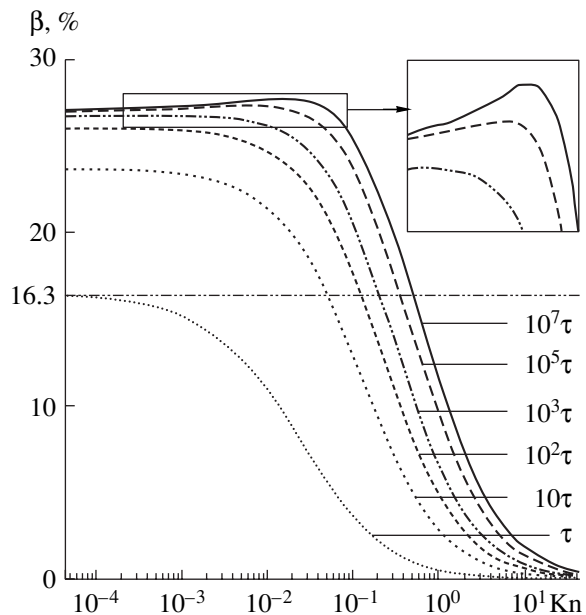


**Fig. 2.** Back flow intensity $\beta$ as a function of the Knudsen number $Kn$ at the moments of time $t = \tau, 10\tau, 10^2\tau, 10^3\tau, 10^5\tau,$ and $10^7\tau$.

is different for different moments of time (see insert in Fig. 2).

In order to explain the results obtained, we consider basic reasons responsible for the back-flow intensity. A rise of the evaporation rate results in an increase in the number of collisions inside the vapor cloud and, correspondingly, to an increase in the number of particles returning to the surface. In this case, for $Kn > 0.1$, a
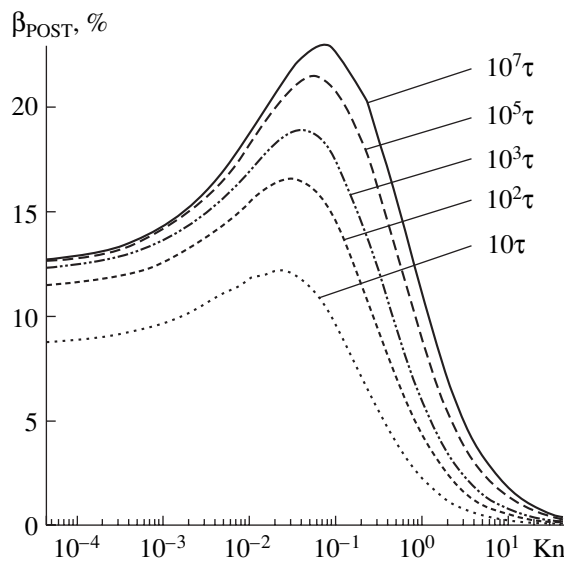
$\beta_{POST}$, %



**Fig. 3.** Back flow intensity $\beta_{POST}$ upon completion of the pulse as a function of the Knudsen number Kn at the moments of time $t = 10\tau$, $10^2\tau$, $10^3\tau$, $10^5\tau$, and $10^7\tau$.
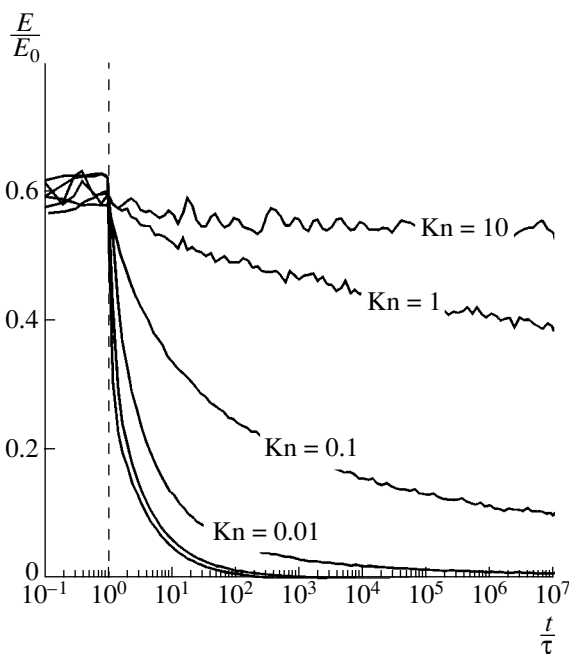
$\dfrac{E}{E_0}$



**Fig. 4.** Time evolution of the energy $E$ of returning particles. The energy is normalized to the energy $E_0$ of evaporated particles for the Knudsen numbers Kn = 0.0001, 0.001, 0.01, 0.1, 1, and 10.

returning particle can pass through the cloud without collisions, so that the rise in the collision frequency leads to an increase in the back flow. However, for Kn < 0.1, the cloud prevents a particle from passing through it; therefore, the back flow ceases to increase further. Collisions transform the thermal energy of particle chaotic motion into the energy of directed motion,

which results in a temperature drop in the cloud. This drop, first, leads to a decrease in the collision frequency and, second, reduces the probability of the particle turning towards the target after a collision. Thus, in the case of a decrease in the Knudsen number, the increase in the density results in the rise of the quantity $\beta$, whereas the corresponding temperature drop leads to a decrease in $\beta$. The maximum obtained of the back flow intensity is apparently caused by these two opposite tendencies.

Particular attention was paid to the back-flow intensity upon the completion of the pulse. The fraction of particles that returned to the surface after pulse termination was determined as

$$\beta_{POST}(t) = \frac{\beta(t) - \beta(\tau)}{1 - \beta(\tau)}.$$

The dependence of $\beta_{POST}$ on the Knudsen number is nonmonotonic and has a maximum in the vicinity of Kn = 0.1 (Fig. 3). This maximum is apparently associated with a low intensity of the back flow at the evaporation stage ($\beta = 3.6\%$) and a high back flow once the pulse has ended ($\beta = 25.6\%$, Fig. 1).

Similar results were obtained in [8] on the basis of the approximate analytical solution within the framework of the continual description of the cloud decay, i.e., for Kn = 0. For example, in [8], $\beta_{POST}(20\tau) = 8.9 \pm 1.66\%$ and $\beta_{POST}(\infty) = 10.4 \pm 1.95\%$. In the present paper, for Kn = $10^{-4}$, the values $\beta_{POST}(20\tau) = 10.1\%$ and $\beta_{POST}(10^7\tau) = 12.9\%$ were obtained.

Account for the back-flow intensity after pulse termination is especially important for correct comparison of experimental and calculated data related to the mass of the evaporated substance, because we can measure the mass only after the decay of the cloud has completed. As is seen from Fig. 3, the difference in the mass of the removed substance, which is caused by the back flow upon completion of the pulse, can exceed 20%.

The time evolution of the energy of returning particles is presented in Fig. 4. Independently of the amount of the evaporated substance, the average energy of returning particles during the pulse remains the same and attains about 60% of the energy of the particles at the moment of their evaporation. These data are consistent with those of [7], in which it is shown that, at the stationary evaporation, the temperature near the cloud surface reaches approximately $0.7T_0$. Thus, due to the low-energy back particle flow, an additional cooling of the evaporating surface and the associated energy increase in the expanding cloud occur. For example, in the case of Kn = $10^{-4}$ and for the entire calculation time, the back flows of the mass and energy to the surface reach 27.1 and 11.4%, respectively. As a result, the energy of particles presented in the cloud increases for the expansion time by 21.5%.

The data obtained on the intensity of the back flow of the mass and energy in the case of pulsed evapora-

tion into vacuum can be useful for the more correct setting of boundary conditions when modeling the evaporation process.

## REFERENCES

1. S. I. Anisimov, Ya. A. Imas, G. S. Romanov, and Yu. V. Khodyko, *Effects of High-Power Radiation on Metals* (Nauka, Moscow, 1970).
2. P. R. Willmott and J. R. Huber, Rev. Mod. Phys. **72**, 315 (2000).
3. W. Jiang, K. Ide, S. Kitayama, *et al.*, Jpn. J. Appl. Phys., Part 1 **40**, 1026 (2001).
4. S. D. Kovaleski, R. M. Gilgenbach, L. K. Ang, and Y. Y. Lau, J. Appl. Phys. **86**, 7129 (1999).
5. R. Burton and P. Turchi, J. Propul. Power **14**, 716 (1998).
6. P. Taborek, Phys. Rev. Lett. **48**, 1737 (1982).
7. D. Sibold and H. M. Urbassek, Phys. Fluids A **5**, 243 (1993).
8. R. Kelly and A. Miotello, Nucl. Instrum. Methods Phys. Res. B **91**, 682 (1994).
9. M. Keidar, J. Fan, I. D. Boyd, and I. I. Beilis, J. Appl. Phys. **89**, 3095 (2001).
10. I. NoorBatcha, R. R. Lucchese, and Y. Zeiri, J. Chem. Phys. **86**, 5816 (1987).
11. D. Sibold and H. M. Urbassek, Phys. Rev. A **43**, 6722 (1991).
12. N. M. Bulgakova, M. Yu. Plotnikov, and A. K. Rebrov, Teplofiz. Aéromekh. **5**, 421 (1998) [Thermophys. Aeromech. **5**, 385 (1998)].
13. O. Ellegaard, J. Schou, and H. M. Urbassek, Appl. Phys. A **69**, S577 (1999).
14. N. Yu. Bykov and G. A. Lukianov, Teplofiz. Aéromekh. **9**, 247 (2002) [Thermophys. Aeromech. **9**, 235 (2002)].
15. G. A. Bird, *Molecular Gas Dynamics and the Direct Simulation of Gas Flows* (Clarendon, Oxford, 1994).

*Translated by G. Merzon*

===== **PHYSICS** =====

# Computer Simulation of Nucleation
# in a Liquid under Tension

## V. G. Baĭdakov and S. P. Protsenko

Presented by Academician V.P. Skripov June 30, 2003

Recently, the numerical simulation technique (Monte Carlo and molecular dynamics methods) has been widely used for studying processes of nucleation and growth of an incipient phase in liquids, gases, and crystals [1–6]. This approach makes it possible to rigorously solve a problem because it is based on fundamental principles of molecular theory. Here, basic approximations are related to a model interparticle potential and to the finiteness of the particle number used in the model. Since the probability of origination of an incipient-phase nucleus in a metastable system within a fixed time interval is proportional to the volume of the system, the fact that the particle number in the model is small becomes a certain advantage of numerical simulations when compared to natural experiments. In particular, this advantage permits both large supersaturations and nucleation rates currently unattainable in natural experiments to be realized in molecular models.

This paper is devoted to a molecular dynamics model of nucleation in a Lennard-Jones liquid under negative pressures and tensile stresses close to spinodal ones. The fact of phase decay under these conditions has been observed in our studies [7, 8] in which the equation of state of a metastable Lennard-Jones fluid was considered. In this paper, we present results of our analysis of spontaneous-nucleation kinetics and phase transformations in the framework of a molecular model of a simple liquid.

The system under investigation contained $N = 2048$ particles placed in a cube-shaped cell, periodic conditions being imposed at its boundaries. The interparticle interaction was described by the Lennard-Jones potential

$$\phi(r) = \begin{cases} 4\varepsilon\left[\left(\dfrac{\sigma}{r}\right)^{12} - \left(\dfrac{\sigma}{r}\right)^{6}\right], & r < r_{\mathrm{c}} \\ 0, & r > r_{\mathrm{c}}. \end{cases}$$

_____

*Institute of Thermal Physics, Ural Division,*
*Russian Academy of Sciences,*
*ul. Amundsena 106, Yekaterinburg, 620016 Russia*

Here, $\varepsilon$ and $\sigma$ are parameters of the potential and $r_{\mathrm{c}}$ is the cutoff radius taken as $6.57\sigma$. In what follows, all quantities will be presented in a reduced form and marked with asterisks. The Boltzmann constant $k_{\mathrm{B}}$, the variables $\varepsilon$ and $\sigma$, and particle mass $m$ are taken as scale parameters.

In the calculations, we took the energy $E$, volume $V$ and particle number $N$ as constant quantities. The states under investigation at isotherm $T^* = \dfrac{Tk_{\mathrm{B}}}{\varepsilon} = 0.7$ are shown in Fig. 1. We found the density $\rho_{\mathrm{s}}^*$ and pressure $p_{\mathrm{s}}^*$ in the phase equilibrium state using a special model of a liquid film surrounded by vapor [7], which turned out to be $\rho_{\mathrm{s}}^* = \rho_{\mathrm{s}}\sigma^3 = 0.8375$ and $p_{\mathrm{s}}^* = \dfrac{p\sigma^3}{\varepsilon} = 0.0013$. The spinodal was determined by the extrapolation of the data obtained to the region of states, where the metastable-liquid lifetime was less than the thermodynamic equilibrium time of the system. The extrapolation was performed with the use of the equation of state [9]: $\rho_{\mathrm{sp}}^* = 0.695$, $p_{\mathrm{sp}}^* = -0.9635$.

In an isolated finite many-particle system, the work of nucleation of the incipient phase is determined by the entropy increment $\Delta S$:

$$W = -(S_{\mathrm{het}} - S_{\mathrm{hom}})T = -\Delta S T. \tag{1}$$

We write out the thermodynamic equations for two states, namely, for an initial homogeneous liquid and for a final heterogeneous state involving an incipient-phase ($\alpha$) nucleus and a metastable phase ($\beta$). In this case, the entropy decrement is given by the equation

$$\begin{aligned} \Delta S &= S_\alpha + S_\beta - S_{\mathrm{hom}} \\ &= \frac{1}{T_\alpha}(E_\alpha + p_\alpha V_\alpha - \mu_\alpha N_\alpha - \gamma A) \\ &+ \frac{1}{T_\beta}(E_\beta + p_\beta V_\beta - \mu_\beta N_\beta) - \frac{1}{T}(E + pV - \mu N). \end{aligned} \tag{2}$$
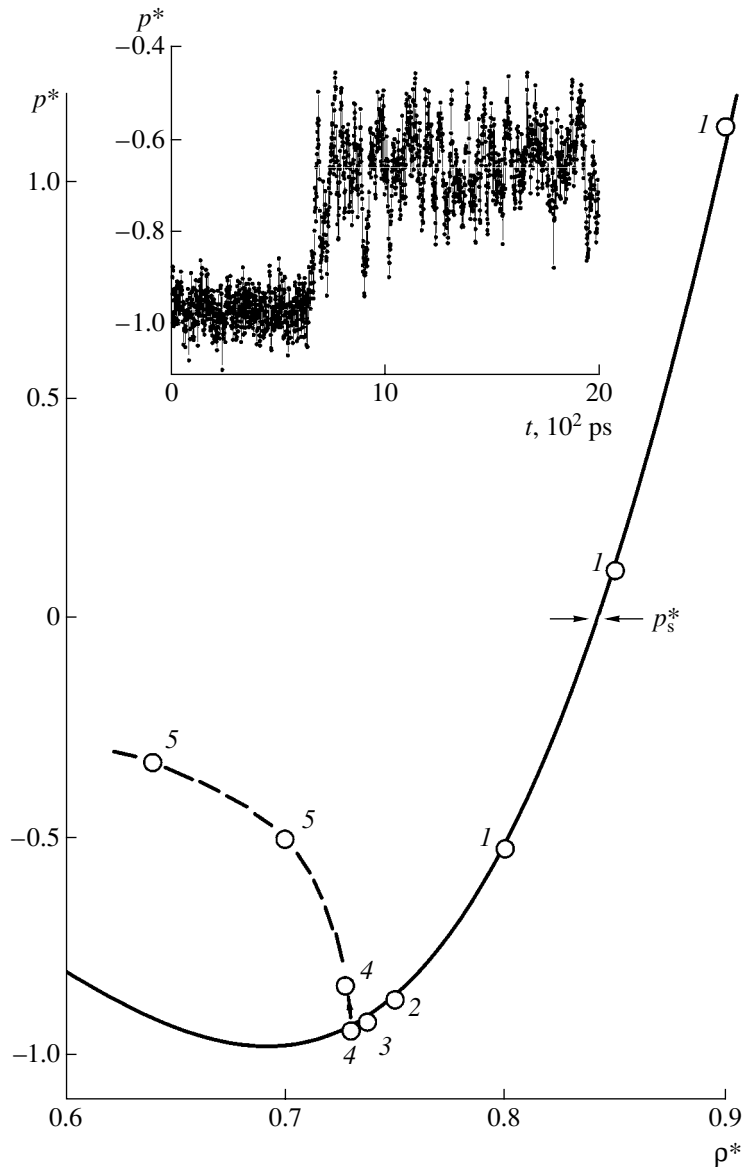
**Fig. 1.** Isotherm $T^* = 0.7$ for the liquid–gas phase transition.

Here, $\mu$ is the chemical potential, $\gamma$ is the surface tension, $A$ is the area of the discontinuity surface, $V = V_\alpha + V_\beta$, $N = N_\alpha + N_\beta$, and $E = E_\alpha + E_\beta$.

Substituting the equilibrium conditions (namely, the equalities $T_\alpha = T_\beta = T_e$, $\mu_\alpha = \mu_\beta$, and $p_\alpha - p_\beta = \dfrac{2\gamma}{r_\alpha}$) into Eqs. (1) and (2), we find the extreme value of $W$ corresponding to an equilibrium nucleus originating in the medium:

$$W_0 = \frac{1}{3}\frac{T}{T_e}\gamma A - \left(\frac{T}{T_e} - 1\right)E - \left(\frac{T}{T_e}p_\beta - p\right)V$$

$$+ \left(\frac{T}{T_e}\mu_\beta - \mu\right)N. \tag{3}$$

The three last terms in Eq. (3) and the factor $\dfrac{T}{T_e}$ ahead of the first term describe changes in thermal, mechanical, and material states of the medium in the course of the nucleation. For an infinite system, the last terms vanish, $\dfrac{T}{T_e} = 1$, and Eq. (3) reduces to the Gibbs formula [10]. If the growth of a nucleus is accompanied by significant changes in the state of the surrounding phase then, in addition to the maximum corresponding to the unstable equilibrium, the function $W(r_\alpha)$ could have a minimum for which the stable equilibrium of the nucleus in the medium occurs (Fig. 2).

Case *1* (see Figs. 1 and 2) corresponds to a stable, saturated, and weakly metastable liquid. In this case,

the equilibrium of the liquid and a gas bubble in a finite system is impossible. For a metastable liquid, the tension under which such an equilibrium is impossible depends on sizes of the system. The statistical analysis of particle configurations in the states mentioned above testifies to a uniform particle distribution in the cell.

If states corresponding to the labile region are chosen as initial states, the nucleation occurs without any activation and at a high rate. Since the initial density is small, a cavity whose shape significantly differs from a sphere originates in the liquid. The lower the initial density of the liquid, the greater the characteristic size of the cavity and the higher the pressure is in the two-phase system (case *5*).

Case *4* corresponds to small values of both the activation barrier and the metastable-liquid lifetime, the latter being less than the simulation time scale in the numerical experiment. In this case, we fixed the process of nucleation, i.e., the transition of the system into the equilibrium two-phase state via the formation and growth of a critical nucleus.

If the density of liquid is greater than or equal to $\rho^* = 0.73$, the liquid remains uniform during the usual simulation time of the numerical experiment (cases *2* and *3*). The density change from $\rho^* = 0.73$ to $0.7275$, i.e., by only 0.34%, results in the origination of cavitation events. One of the pressure time scans is shown in the inset of Fig. 1. The time reference point corresponds to the moment when the density of the system is equal to $\rho^* = 0.7275$.

We carried out 72 simulations ($n_0 = 72$) of the bubble cavitation. Each of the numerical experiments started from a new microstate with $\rho^* = 0.73$, which had a time lag not less than 100 ps with respect to the previous simulation. This allowed us to consider the simulations as independent experiments.

In Fig. 3, we present the histogram of the expectation times for the appearance of a critical nucleus in the system. This plot verifies the random character of metastable-state decays. For the parameters given above, the mean lifetime of the liquid under tension in the volume

$$V = 1.1 \times 10^{-19} \text{ cm}^3 \text{ is equal to } \bar{\tau} = \frac{\sum\limits_{i=1} \tau_i}{n_0} = 586 \text{ ps. In}$$

this case, the nucleation rate is

$$J = \frac{1}{\bar{\tau}V} = 1.5 \times 10^{28} \text{ s}^{-1} \text{ cm}^{-3}. \tag{4}$$

According to the Poisson distribution,

$$n = n_0 \bar{\tau}^{-1} \exp\left(-\frac{\tau}{\bar{\tau}}\right) \Delta\tau. \tag{5}$$

The experimental histogram is in close agreement with distribution (5). This result is consistent with the direct experimental data of [11].
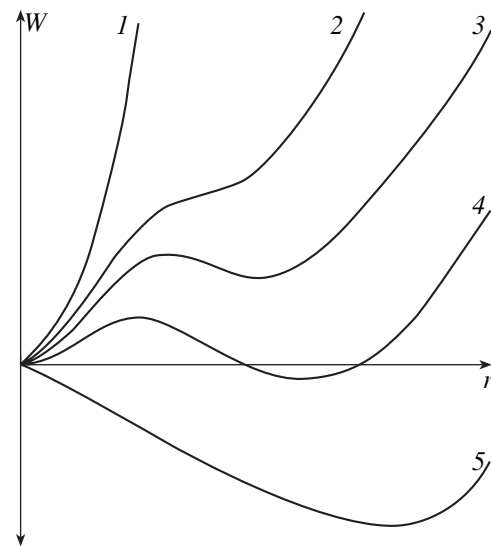


**Fig. 2.** Nucleation work $W$ as a function of the incipient-phase size for various initial supersaturations in an isolated system. (The volume of the system and particle number in it are constant.)
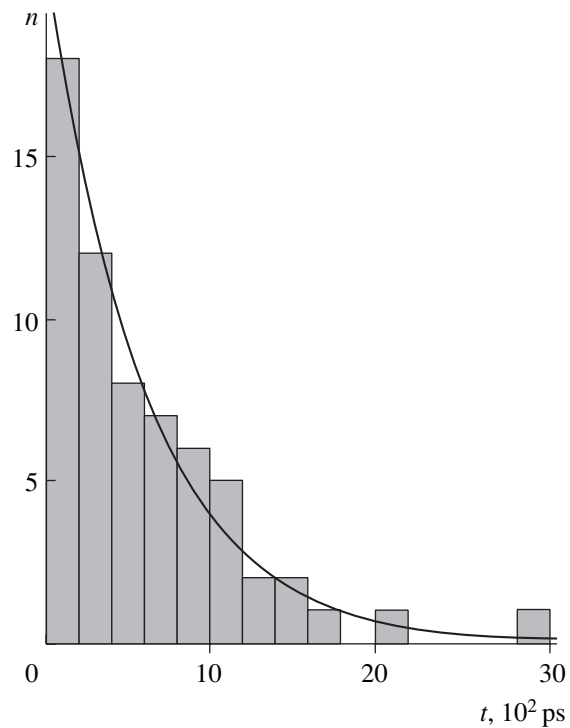


**Fig. 3.** Histogram of the expectation time for the appearance of the critical nucleus in a system. The curve is calculated according to Eq. (5).

In order to confirm that the metastable-state decays occurred via nucleation and to determine the characteristic sizes of incipient-phase nuclei, we developed a program package capable of looking for and displaying on the monitor cavities that originated in the system at various moments of time. The data on coordinates of all
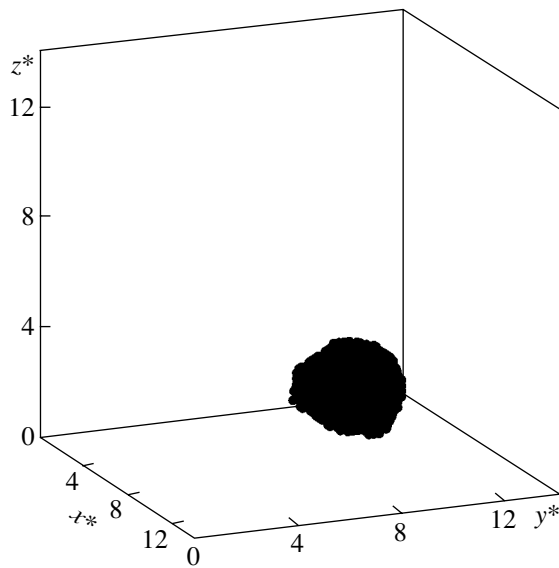
**Fig. 4.** Equilibrium nucleus in a cell.

the particles at each moment of time allowed us to display the model system as a set of balls and to localize bubble positions by scanning in layers. However, this method provides only qualitative data on the position and shape of incipient-phase fragments. A more consistent approach is based on scanning a cell by a tentative particle [6]. This particle interacts with actual particles via the potential

$$u(r) = \begin{cases} \phi(r), & r > 2^{1/6} \\ -\varepsilon, & r < 2^{1/6}. \end{cases}$$

The interparticle spacing $r = 2^{1/6}$ corresponds to the minimum of the Lennard-Jones potential.

When performing the scanning with a step $\Delta r^* = 0.01$, we determined the energy of the tentative-particle interaction with particles of the system within the cutoff radius $r_c^*$ of the interaction potential. For the liquid phase, the interaction energy ranges from $\Delta u^* = -16$ to $\Delta u^* = -6$. In the vicinity of the cavity center, the energy $\Delta u^*$ of the tentative particle is close to zero. At the boundaries of an incipient-phase fragment, the reduced energy varies within the range $-2.9$ to $-2.1$. Using the values found, we constructed the outside surface limiting a fragment of the new phase.

In order to determine positions of vapor-phase particles inside a fragment, we used another method. We introduced a virtual cube-shaped object into a cell such that only one particle could be placed into this object. Then, when displacing the cube in the cell, we registered the absence or presence of particles in the cube. After the scanning, we integrated the empty cubes into clusters.

The shape, position, and size of a fragment that were found using the first and second algorithms were almost coincident, although the latter gave less exact results.

Using these algorithms, we established that in all numerical experiments decays of the metastable states were caused by the formation of local cavities, with their shapes being significantly varied in the course of growth. After passing to a local minimum (Fig. 2, curve *4*), a cavity takes a shape close to that of a sphere (Fig. 4). In this case, the characteristic radius of the equilibrium nucleus is $r_0 \simeq 0.6$ nm.

In addition to the direct transitions caused by the origination of a critical nucleus and its growth to the equilibrium size $r_0$, we observed random inverse fluctuation passages through the potential barrier $W_*$, which led to decays of nuclei.

Thus, using numerical simulation, we are the first to have studied stochastic mechanisms of cavitation in conditions of strong metastability. We have determined the nucleation rate and have proposed algorithms based on molecular-dynamics methods for localizing positions of incipient-phase nuclei. This makes it possible to perform a detailed verification of the conventional theory of homogeneous nucleation, namely, the direct experimental determination of both the nucleation work and the rate of passage through the critical size.

## REFERENCES

1. P. R. Wolde and D. Frenkel, J. Chem. Phys. **109**, 9901 (1998); **109**, 9919 (1998).

2. K. Laaksonen and A. Laaksonen, J. Chem. Phys. **113**, 9741 (2000).

3. P. Schaaf, B. Senger, J.-C. Voegel, *et al.*, J. Chem. Phys. **114**, 8091 (2001).

4. S. Toxvaerd, J. Chem. Phys. **115**, 8913 (2001).

5. S. Toxvaerd, J. Chem. Phys. **117**, 10303 (2002).

6. T. Kinjo and M. Matsumoto, Fluid Phase Equilibria **144**, 343 (1998).

7. V. G. Baĭdakov, S. P. Protsenko, G. G. Chernykh, and G. Sh. Boltachev, Phys. Rev. E: Stat. Phys., Plasmas, Fluids, Relat. Interdiscip. Top. **65**, 041601 (2002).

8. V. G. Baĭdakov and S. P. Protsenko, Teplofiz. Vys. Temp. **41**, 231 (2003).

9. G. Sh. Boltachev and V. G. Baĭdakov, Teplofiz. Vys. Temp. **41**, 314 (2003).

10. J. W. Gibbs, *Thermodynamics. Statistical Mechanics*, in *The Collected Papers of J. Willard Gibbs* (Yale Univ. Press, New Haven, 1948; Nauka, Moscow, 1982).

11. V. P. Skripov, *Metastable Liquid* (Nauka, Moscow, 1972).

*Translated by V. Chechin*

═══════════ **PHYSICS** ═══════════

# Phenomenological Model of the Critical Behavior of Real Systems

**D. Yu. Ivanov**

Presented by Academician V.P. Skripov September 8, 2003

Received October 10, 2003

In [1, 2], on the basis of experimental investigation of the critical indices of the coexistence curve $\beta$, isothermal compressibility in the one-phase domain $\gamma$, critical isotherm $\delta$, and correlation radius $\nu$, it was shown that the near-critical-point behavior of real, nonideal, systems whose universality class coincides with that of the Ising model is more complex than it was usually thought. In addition to the well-known crossover—transition from the mean-field behavior to the Ising behavior—whose position is specified by the Ginzburg criterion [3], one more crossover, which proceeds in the opposite direction, i.e., from the fluctuation behavior to the classical one, appeared to be possible near the critical point of such systems. Thus, the nearest neighborhood of the critical point of real systems, in contrast to idealized systems, is of the mean-field type.

In this work, a simple physical model based in principle only on the first principles of the current theory of critical phenomena is proposed to explain such a nontrivial behavior of real systems.

It is well known that the features of the critical behavior of various systems are determined by fluctuations increasing when approaching a critical point. We consider a real physical system approaching the critical point from temperature region I (Fig. 1). Let fluctuations of the order parameter in the system increase noticeably at temperature $T_1$ and be so developed at temperature $T_1'$ that their radius (correlation length) becomes, according to Kadanoff's idea [4], the only determining scale characterizing the properties of the system. As a result, the system falls into fluctuation region II (Fig. 1), completing the transition from the mean-field behavior to the Ising-type behavior. This well-known transition will be called the first crossover [1, 2].

As is known, an increase in compressibility (susceptibility) of the system is directly associated with the

development of fluctuations (see, e.g., [5]). This means that an increase in fluctuations is accompanied by the unlimited increase in the susceptibility of the system, including susceptibility to various external and internal perturbations, or "fields," such as gravitational and electric fields, surface forces and shear stresses, turbulence, the presence of boundaries, etc. Moreover, the critical point is a point of decreased stability [6]; i.e., fluctuations determining, according to Kadanoff [4] and Wilson and Kogut [7], the critical behavior are very unstable formations very sensitive to perturbations of various physical origins. In view of these circumstances, it is natural to assume that, when moving into the critical region, the system inevitably reaches a point where fluctuations are first deformed (at temperature $T_2'$, e.g., Fig. 1) and are then completely suppressed (at temperature $T_2$) by a certain applied field.[1] As a result, the system finally falling to region III (Fig. 1) undergoes a new transition in the opposite direction, i.e., from the fluctuation behavior to the mean-field behavior. By analogy, this transition will be called the second crossover [1, 2].

It is possible to determine which of the above transitions (I ⟷ II or II ⟷ III) occurs in a certain case by using, in particular, the combination of the critical indices that is well known for each of these regions (for a given universality class of the system). When the fluctuations of the order parameter in the system are only under development (Fig. 1, $T_1 T_1'$ section in region II) or are already deformed (anisotropic) but are not yet completely suppressed ($T_2' T_2$ section), the behavior must be transitional with intermediate critical indices. In this case, the universality of critical phenomena seems to be also manifested in the absence of the limiting critical indices other than fluctuation or classical values.

Indeed, the current theory of critical phenomena in idealized systems (see, e.g., [7]) provides mean-field, classical, indices for space dimensions $d \geq 4$ and fluctuation, Ising, indices for $d < 4$ (see, e.g., [5]). The renormalization-group approach applied to a particular case

---

*St. Petersburg State University of Low-Temperature and Food Technologies,*
*ul. Lomonosova 9, St. Petersburg, 191002 Russia*
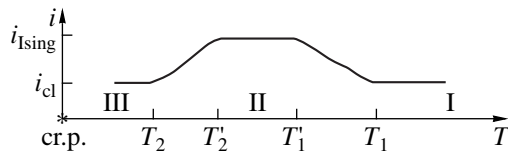*e-mail: dmitri.ivanov@pobox.spbu.ru*

[1] In the absence of any field, the boundary of the sample can play role of this field.

**Fig. 1.** Curve approximating the behavior of the critical indices $i$ of real systems near the critical temperature (density) point (cr.p.).
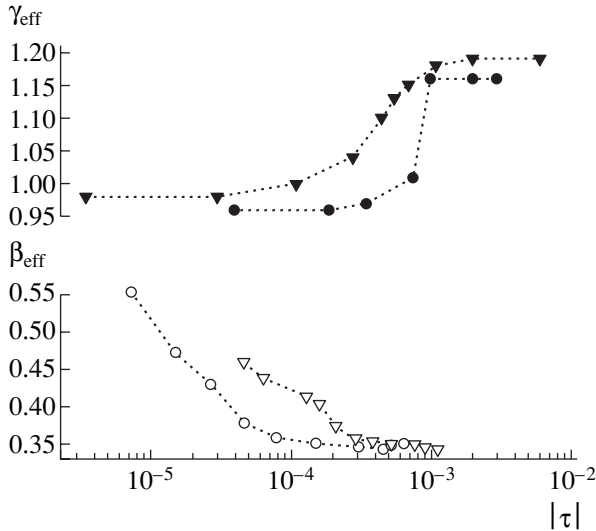


**Fig. 2.** Effective critical indices of the coexistence curve $\beta_{eff}$ and isothermal compressibility $\gamma_{eff}$ for pure ($\bigcirc$ [9], $\nabla$ [12], $\bullet$ [10, 11]) $SF_6$ and ($\blacktriangledown$ [13]) $CO_2$ in the second crossover region. Data for $\beta$ and $\gamma$ refer to the ranges $\tau < 0$ and $\tau > 0$, respectively. The piezometer height was equal to 8 [9–11] and 30 [12, 13] mm. For convenience, experimental points are connected by straight lines.

of the critical behavior of real systems, namely, to the behavior of a fluid in a flow in the presence of shear stresses, provided the same two sets in the limiting case [6]. It is of interest that the experiment carried out in [8] with the aniline–cyclohexane binary mixture, where it was easy to vary this type of perturbation (shear stresses), revealed the entire spectrum of intermediate values of the critical susceptibility index $\gamma$, which actually lied between the limiting values, Ising (1.24) and classical (1.0), known for it.

In the framework of the general pattern in the proposed model (Fig. 1), different nonideal systems differ from each other by different positions of the boundaries of region II between the crossovers. For some cases, this region can completely disappear. Although this model is simple, it allows a detailed elaboration concerning the position of these boundaries. First, if perturbing fields ensure the suppression of fluctuations over the entire temperature range, region II can be absent. This is the case for systems with long-range forces (superconductors, ferroelectric materials, etc.), whose behavior is always classical mean-field [5]. Sec-

ond, the position of the boundaries of the fluctuation region must be different not only for different nonideal systems but also for different physical properties of the same system that behave differently near the critical point. In other words, curves similar to those shown in Fig. 1, which present various physical properties, must have individual positions of regions I, II, and III with respect to the critical point. In particular, these curves can be shifted with respect to each other along the horizontal axis (in temperature or density), can have different slopes near the first and second crossovers, etc. This refinement seems to be physically justified, because different properties that have a common cause of the anomalous behavior near the critical point are described by different critical indices, which testifies to different dependences of these properties on the level of fluctuations. Indeed, the anomaly of the coexistence curve of a certain fluid in the presence of, e.g., gravity needs not to be at the same distance from the critical point as the anomaly of, e.g., isothermal compressibility or specific heat of the same fluid under the same conditions. We note that the Ginzburg criterion, which is based on the comparison of contributions from the volume and correlation energies in the application to the anomaly of the specific heat at constant volume, does not *a priori* suppose such a possibility [3].

Thus, simple physical reasons lead us to a new, more complex and detailed pattern of physical phenomena under real conditions. Any action, even infinitely weak far from the critical point, becomes predominant near the critical point, where it determines the growth and form of critical fluctuations in the system and, therefore, changes the type of its critical behavior.

The behavior near the second crossover is of special interest for experimental corroboration of the above concepts [1]. For simple fluids, this is the nearest neighborhood of the critical point, where highly sensitive, stable, and accurate instruments must be used. A few such experiments are available (see, e.g., [9–13]).[2]

Analyzing data of the $p\rho T$ experiments for two samples of $SF_6$ (purity of 99.9995% [2, 9–11] and 99.9994% [12, 13]) and $CO_2$ (purity of 99.9999% [13]), which are likely the purest samples that have ever been studied, we obtain the temperature dependences of the critical indices $\beta$ and $\gamma$ shown in Fig. 2. These curves clearly demonstrate the similarity between the critical behavior of real systems (simple pure fluids) near the second crossover and predictions of the above model (Fig. 1) for both $i_{Ising} > i_{cl}$ (critical index $\gamma$) and $i_{Ising} < i_{cl}$ (critical index $\beta$).

In addition, Fig. 2 directly illustrates one of the discussed features of the critical behavior of real systems near the critical point: the second crossover for different physical properties of the same system under simi-

---

[2] In these experiments, the errors of measurements of pressure and density did not exceed 0.001 and 0.02%, respectively, and temperature was kept with an accuracy of no worse than 200 [9–11] and 20 [12, 13] μK.

lar conditions is observed at different distances from the critical point. As is seen in Fig. 2, the second crossover for "strong" critical index of isothermal compressibility $\gamma$ is by almost two orders of magnitude farther from the temperature critical point $\left( \tau = \dfrac{T}{T_{cr}} - 1, \text{ where} \right.$

$T_{cr}$ is the critical temperature$\Big)$ than the similar transition for the "weak" index of the coexistence curve $\beta$. It is very important to consider this circumstance when testing the validity of the universal relations between critical indices. It is now clear that the effective values of all critical indices for such a test in real systems must be extracted from the corresponding region of the curve (Fig. 1) for each individual index rather than from the same temperature (density) range as was usually done. All desired critical indices (no less than three) must be determined for the same sample at the same experimental setup. In particular, according to our data for $SF_6$ (Fig. 2 [1, 2, 10]), an important relation $\gamma = \beta(\delta - 1)$ for the static critical indices is satisfied almost exactly for both the fluctuation region ($|\tau| \geq 3 \times 10^{-5}$ and $10^{-3}$ for $\beta$ and $\gamma$, respectively), where $\beta = 0.3508 \pm 0.0013$, $\gamma = 1.16 \pm 0.03$, and $\delta = 4.30 \pm 0.01$ [2, 10], and the region where fluctuations are suppressed, where $\beta \approx 0.5$, $\gamma \approx 1$ (Fig. 2 [1, 2, 10]), and $\delta \approx 3$ [1, 2, 10]. At the same time, it is seen that the use of the critical indices from the same intermediate temperature range, e.g., $3 \times 10^{-5} < |\tau| < 3 \times 10^{-4}$ (Fig. 2), would be unfounded.

Among other features, we note that the curves for two critical indices have different slopes near the second crossover. In this region, the narrower temperature range (sharper dependence) is also observed for the $\gamma$ index, which is physically natural. We note that the critical density for $\tau < 0$ falls into the range of labile states, which reduces maximum fluctuations as compared to $\tau > 0$ with the same $|\tau|$ [14]. The slope of the curve near the second crossover indicates that the perturbing field continuously deforms critical fluctuations and, then, completely suppresses them.

In the opinion of the authors of [1, 2, 9, 10, 12, 13], the gravitational field of the Earth played the role of such a field in the experiments described in [9–13]. This is corroborated by Fig. 2. It is seen that the index $\beta$ for the same substance ($SF_6$) in the higher vessel begins to vary near the second crossover at larger distances from the critical point. According to the analysis made in [13] for the behavior of the critical index $\gamma$ near the critical points in $SF_6$ and $CO_2$, the relative temperature distance ($\tau$) of the transition is proportional to the density of the substance. Both the above conclusions can inevitably be considered as substantial evidence that, as

was first pointed out in 1974 [9, 10], gravity is the principal cause of changes in the critical indices to its classical values near the critical point. We emphasize that the key effect of gravity on the appearance of the second crossover in simple pure fluid is not reduced to trivial redistribution of the substance density over the vessel height. It is the internal gravitational effect, which, according to [15], "changes the local properties of a fluid modifying thereby the origin of the phase transition" (for more details, see [1, 2, 9, 10, 12, 13]).

## ACKNOWLEDGMENTS

## REFERENCES

1. D. Yu. Ivanov, Dokl. Akad. Nauk **383**, 478 (2002) [Dokl. Phys. **47**, 267 (2002)].
2. D. Yu. Ivanov, *Critical Behavior of Nonideal Systems* (Fizmatlit, Moscow, 2003).
3. V. L. Ginzburg, Fiz. Tverd. Tela (Leningrad) **2**, 2031 (1960) [Sov. Phys. Solid State **2**, 1824 (1960)].
4. L. P. Kadanoff, Physics **2**, 263 (1966).
5. R. Balesku, *Equilibrium and Nonequilibrium Statistical Mechanics* (Wiley, New York, 1975; Mir, Moscow, 1978).
6. A. Onuki and K. Kawasaki, Ann. Phys. **121**, 456 (1979).
7. K. Wilson and J. Kogut, *The Renormalization Group and the ε-Expansion* (Wiley, New York, 1974; Mir, Moscow, 1975); Phys. Rep. **12C** (2), 75 (1974).
8. D. Beysens, M. Gbadamassi, and L. Boyer, Phys. Rev. Lett. **43**, 1253 (1979).
9. D. Yu. Ivanov, L. A. Makarevich, and O. N. Sokolova, Pis'ma Zh. Éksp. Teor. Fiz. **20**, 272 (1974) [JETP Lett. **20**, 121 (1974)].
10. D. Yu. Ivanov and V. K. Fedyanin, Preprint No. R4-8430, OIYaI (Joint Institute for Nuclear Research, Dubna, 1974).
11. L. A. Makarevich, O. N. Sokolova, and A. M. Rozen, Zh. Éksp. Teor. Fiz. **67**, 615 (1974) [Sov. Phys. JETP **40**, 305 (1975)].
12. W. Wagner, N. Kurzeja, and B. Pieperbeck, Fluid Phase Equilibria **79**, 151 (1992).
13. N. Kurzeja, Th. Tielkes, and W. Wagner, Int. J. Thermophys. **20**, 531 (1999).
14. V. P. Skripov, *Metastable Liquid* (Nauka, Moscow, 1972; Halsted, New York, 1974).
15. J. V. Sengers and J. M. J. van Leeuwen, Int. J. Thermophys. **6**, 545 (1985).

*Translated by R. Tyapaev*

---

**PHYSICS**

---

# γ-UMo₂O₈ as a New Polymorph
# of Uranium Dimolybdate Containing Tetravalent Uranium

## S. V. Krivovichev* and P. C. Burns**

Presented by Academician V.S. Urusov September 29, 2003

Received October 1, 2003

In the last few years, uranium-containing minerals and inorganic compounds have attracted increasing interest in connection both with their important role in the processes of the transmutation of spent nuclear fuel [1] and with their possible use as host materials for the immobilization of transuranium elements (first of all, weapons-grade plutonium) and radionuclides [2, 3]. Since molybdenum is one of the products of $^{239}$U decay, the study of uranium molybdates is of special interest [4, 5]. Two polymorphs—trigonal $\alpha$-UMo₂O₈ [6] and orthorhombic $\beta$-UMo₂O₈ [7–9]—of uranium dimolybdate containing tetravalent uranium are known at present. In addition, the UMo₂O₈ formula was revealed for sedovite, a mineral found in the oxidation zone of uranium–molybdenum ores [10]. In the present paper, we report the results concerning the synthesis and crystal structure of a new UMo₂O₈ polymorph, which can be referred to as $\gamma$-UMo₂O₈.

Crystals of $\gamma$-UMo₂O₈ were grown by the hydrothermal method. We took 0.078 g of $UO_2(CH_3COO)_2 \cdot 2H_2O$ and 0.072 g of $MoO_3$ and mixed them with 0.15 g of glycerin, 0.032 g of 40% HCl, and 5 ml of distilled water. A Teflon capsule with the mixture was placed in an autoclave and kept for 65 h at 220°C. After cooling, we found a coaly amorphous (according to the X-ray analysis) substance at the bottom of the autoclave. Its black flakes contained dark goldish yellow $\gamma$-UMo₂O₈ plates.

For the X-ray analysis, we selected a $0.12 \times 0.04 \times 0.008$-mm single crystal. The intensities of diffraction peaks were measured at the University of Notre Dame (Indiana, USA) on a Bruker SMART diffractometer equipped with a CCD (charge-coupled device) detector. The unit-cell parameters were calculated by the least squares fitting based on 1195 intense reflections. The

---

*\* Department of Geology, St. Petersburg State University,*
*Universitetskaya nab. 7/9,*
*St. Petersburg, 199034 Russia*
*e-mail: skrivov@mail.ru*

*\*\* University of Notre Dame, 156 Fitzpatrick Hall,*
*Notre Dame, Indiana, 46556-0767 USA*

unit cell is orthorhombic with lattice constants $a = 10.1909(7)$ Å, $b = 9.5857(7)$ Å, and $c = 14.2741(11)$ Å and volume $V = 1394.4(2)$ Å$^3$. The extinction characteristics and the statistics in the distributions of reflections suggested the space group *Pbca*. The set of structure factors was obtained by the SAINT program after introducing the corresponding corrections. The structure was determined by direct methods and was refined up to $R_1 = 0.034$ ($wR_2 = 0.049$) for 1663 reflections with $|F_{hkl}| \geq 4\sigma|F_{hkl}|$. The final model included the positions and isotropic thermal parameters for all atoms (see Table 1). The interatomic distances are presented in Table 2.

The $\gamma$-UMo₂O₈ compound has the same structure as UW₂O₈ [11], $\beta$-Th(WO₄)₂ [12], and PuMo₂O₈ [13] (note, however, that the structure was determined only for UW₂O₈). In the $\gamma$-UMo₂O₈ crystal structure, uranium atoms have an eightfold coordination with oxygen atoms (the Archimedean antiprism or the Thompson cube), whereas molybdenum atoms are in tetrahedral coordination with oxygen. The calculation of local valence balance with the parameters taken from [14]

**Table 1.** Positions and isotropic thermal parameters (in Å$^2$) of atoms in the crystal structure of γ-UMo₂O₈

| Atom | $x$ | $y$ | $z$ | $U_{iso}$ |
|------|------|------|------|------|
| U | 0.96619(3) | 0.22463(3) | 0.39029(2) | 0.00876(7) |
| Mo(1) | 0.77565(6) | 0.50369(8) | 0.56063(5) | 0.00937(14) |
| Mo(2) | 0.10523(6) | 0.31525(8) | 0.15083(5) | 0.0103(2) |
| O(1) | 0.9958(5) | 0.2309(6) | 0.2300(4) | 0.0166(13) |
| O(2) | 0.6744(5) | 0.3896(6) | 0.6245(5) | 0.0209(15) |
| O(3) | 0.8911(5) | 0.5905(5) | 0.6345(4) | 0.0136(13) |
| O(4) | 0.2677(5) | 0.2681(6) | 0.1808(4) | 0.0165(13) |
| O(5) | 0.0742(5) | 0.2568(7) | 0.0362(4) | 0.021(2) |
| O(6) | 0.6679(5) | 0.6237(6) | 0.5078(4) | 0.0188(14) |
| O(7) | 0.8586(5) | 0.4131(6) | 0.4724(4) | 0.0176(14) |
| O(8) | 0.0815(5) | 0.4961(6) | 0.1527(5) | 0.0215(14) |
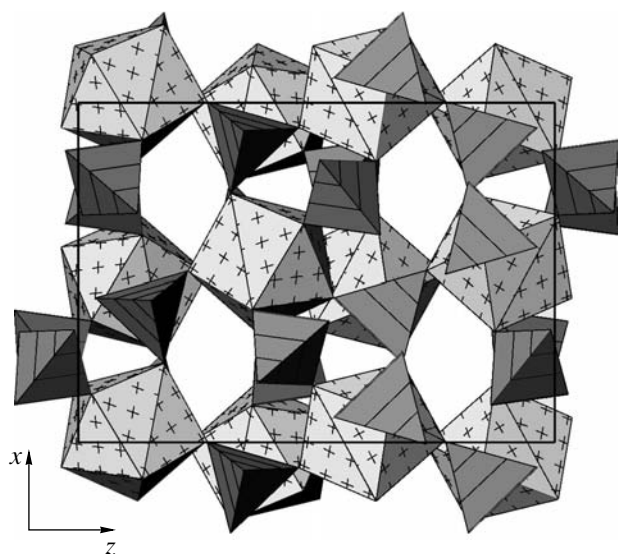
Crystal structure of γ-UMo$_2$O$_8$ in the (010) projection. Eight-vertex UO$_8$ polyhedra are marked by crosses and MoO$_6$ tetrahedra are lined.

The structure of γ-UMo$_2$O$_8$ is less dense than that of β-UMo$_2$O$_8$. The densities of β-UMo$_2$O$_8$ and γ-UMo$_2$O$_8$ are equal to 6.12 and 5.32 g/cm$^3$, respectively. This difference stems from the structural features of the β-UMo$_2$O$_8$ phase, where the molybdenum atoms have octahedral coordination and uranium atoms have sevenfold coordination in the form of a pentagonal bipyramid. Higher coordination numbers, as well as the characteristic joining of the coordination polyhedra by common edges, determine the higher density of the β-polymorph. The high-temperature α-UMo$_2$O$_8$ phase is less dense (5.24 g/cm$^3$), but it is also less stable under normal conditions.

The behavior of plutonium during UMo$_2$O$_8$ crystallization from high-temperature (900°C) melts was discussed in [15]. It turned out that plutonium does not enter into the β-UMo$_2$O$_8$ structure. It remains in the melt or forms mechanical inclusions in the form of Pu-containing phases. Since the new polymorph γ-UMo$_2$O$_8$ is isostructural with PuMo$_2$O$_8$, it is quite probable that this phase could be formed in low-temperature oxidation processes of spent nuclear fuel and serve as an accumulator of plutonium.

demonstrated that the formal valence of U, Mo(1), and Mo(2) is equal to 4.23, 5.91, and 5.87 valence units, respectively. The coordination polyhedra UO$_8$ and MoO$_4$ connected through common vertices form a three-dimensional frame (see figure). It is interesting that each oxygen atom forms a chemical bond with only one uranium atom and one molybdenum atom. Formally, the average U$^{4+}$–O bond valence in U$^{4+}$O$_8$ polyhedron equals about 0.5 valence units, whereas the average Mo$^{6+}$–O bond valence in Mo$^{6+}$O$_4$ polyhedron equals 1.5 valence units. Therefore, the sum of valences corresponding to the bonds coming to oxygen atoms is on average equal to 2; i.e., all valences of oxygen are totally saturated.

**Table 2.** Interatomic distances (in Å) in γ-UMo$_2$O$_8$

| U–O(4) | 2.301(5) | Mo(1)–O(7) | 1.748(6) |
|---|---|---|---|
| U–O(1) | 2.308(6) | Mo(1)–O(2) | 1.758(6) |
| U–O(3) | 2.319(5) | Mo(1)–O(6) | 1.760(6) |
| U–O(8) | 2.326(6) | Mo(1)–O(3) | 1.786(5) |
| U–O(5) | 2.362(6) | ⟨Mo(1)–O⟩ | 1.763 |
| U–O(6) | 2.370(6) | | |
| U–O(2) | 2.397(5) | Mo(2)–O(8) | 1.751(6) |
| U–O(7) | 2.416(5) | Mo(2)–O(5) | 1.759(6) |
| ⟨U–O⟩ | 2.35 | Mo(2)–O(4) | 1.768(5) |
| | | Mo(2)–O(1) | 1.782(5) |
| | | ⟨Mo(2)–O⟩ | 1.765 |

REFERENCES

1. Rev. Mineral.: *Uranium: Mineralogy, Geochemistry and the Environment*, Ed. by P. C. Burns and R. Finch (Miner. Soc. Amer., Washington, 1999), Vol. 38.
2. N. P. Laverov, I. A. Sobolev, S. V. Stefanovskiĭ, *et al.*, Dokl. Akad. Nauk **362**, 670 (1998).
3. N. P. Laverov, A. I. Gorshkov, and S. V. Yudintsev, Dokl. Akad. Nauk **363**, 540 (1998).
4. D. Wronkiewicz and E. Buck, Rev. Miner. **38**, 475 (1999).
5. E. C. Buck, D. J. Wronkiewicz, P. A. Finn, and J. K. Bates, J. Nucl. Mater. **249**, 70 (1997).
6. V. N. Serezhkin, L. M. Kovba, and V. K. Trunov, Radiokhimiya **16**, 231 (1974).
7. P. Pailleret, C. R. Seances Acad. Sci., Ser. C **265**, 85 (1967).
8. L. M. Kovba, Radiokhimiya **13**, 909 (1971).
9. T. L. Cremers, P. G. Eller, R. A. Penneman, and C. C. Herrick, Acta Crystallogr. C **39**, 1163 (1983).
10. K. V. Skvortsova and G. A. Sidorenko, Zap. VMO **94**, 548 (1965).
11. O. N. Rozanova, Z. Ya. Pol'shchikova, and L. M. Kovba, Radiokhimiya **20**, 125 (1978).
12. J. Thoret, Rev. Chim. Miner. **11**, 237 (1974).
13. Powder Diffraction File (PDF-2) #27-1333, 43-1220.
14. P. C. Burns, F. C. Hawthorne, and R. C. Ewing, Can. Mineral. **35**, 1551 (1997).
15. O. A. Ustinov, G. P. Novoselov, N. T. Chebotarev, *et al.*, Radiokhimiya **18**, 115 (1976).

*Translated by K. Kugel*

# Phased Array Antennas
# Based on Distributed Optical Antenna Modules

**Corresponding Member of the RAS L. D. Bakhrakh\* and D. F. Zaĭtsev\*\***

Due to a number of advantages compared to other kinds of antennas, phased array antennas (PAAs) and especially active phased array antennas (APAAs) have gained wide acceptance in modern communication systems, radars, radio astronomy, and the latest cellular communication systems [1]. The APAAs are based on transceiver antenna modules (Fig. 1).

Nevertheless, even modern APAAs are not capable of efficiently solving new problems that have appeared in recent years. The most important of them are the necessity of reliably detecting objects supplied with radio-absorbing coatings, underground radio vision associated with the use of miniature antennas, and providing adaptation to broadband noise and stability with respect to the action of electromagnetic pulses.

Rather recently, a new promising direction has appeared in radar engineering, namely, radiolocation by ultrashort pulses with a duration of less than 1 ns, i.e., pulses lying within a superwide frequency band (from several octaves and higher). Theoretically, the application of ultrashort pulses makes it possible to detect various inconspicuous objects, including those supplied with radio-absorbing coatings since these coatings are efficient only in a narrow frequency band. This method also allows the resolution and spatial measurement accuracy to be qualitatively improved and the underground radiolocation to be realized [2]. Intense efforts aimed at the research and development of corresponding antennas and ultrashort-pulse generators are now being undertaken.

However, for constructing an efficient radar based on an APAA, it is necessary to ensure high-precision phasing (time shift) of antenna radiators and rapid scanning of the beam (beams) in a wide angular range, as well as to provide super-broadband transmission channels between an antenna array and signal processing equipment and the formation in the real-time scale of the directivity pattern adapted in a superwide frequency band. Due to the high dispersity of conventional components employed for constructing an APAA, they in principle do not allow operations with ultrashort pulses to be to ensured. This is explained by the fact that usual radio-frequency transmission lines, delay lines, and other components of a radio-frequency channel having a high dispersion strongly limit the operation frequency bandwidth. In addition, in the case of development of an APAA, specific problems arise when it is employed onboard radar stations on aircrafts, spacecrafts, and other mobile carriers. To provide the required output power of an APAA at the existing efficiency of its modules, it is necessary to remove the thermal power exceeding 50 kW from antenna planes. This results in the need to apply liquid cooling systems associated with extended pipelines in which a volatile coolant circulates. In this case, the mass and size parameters of the system increase, whereas the reliability and viability considerably decrease and the cost elevates. Thus, the problem of efficient and reliable cooling has not been solved to date, since even modern fighter planes are equipped with liquid-cooled APAA systems having a number of disadvantages [3].

An increase in the longitudinal size of antenna modules, which is associated with liquid cooling, results in
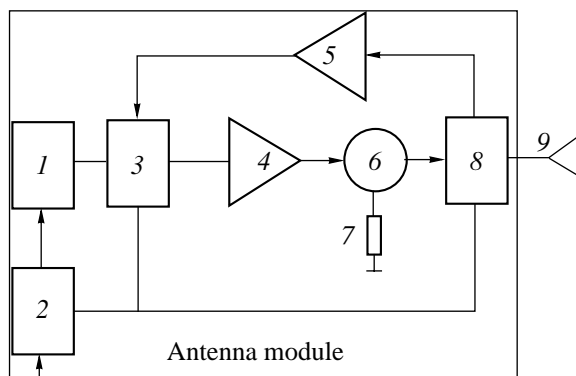
\* *OAO Vega Radio Building Concern,*
  *Moscow, Russia*

\*\* *Moscow State Institute of Radioengineering, Electronics,*
   *and Automation (Technical University),*
   *pr. Vernadskogo 78, Moscow, 117454 Russia*

**Fig. 1.** Typical functional diagram of an antenna module in an APAA: (*1*) stepped phase shifter; (*2*) generator with a digital control system; (*3*) and (*8*) switches of the reception/transmission regimes; (*4*) power amplifier; (*5*) low-noise amplifier of a detected signal; (*6*) circulator; (*7*) load; (*9*) radiating element of an antenna array.
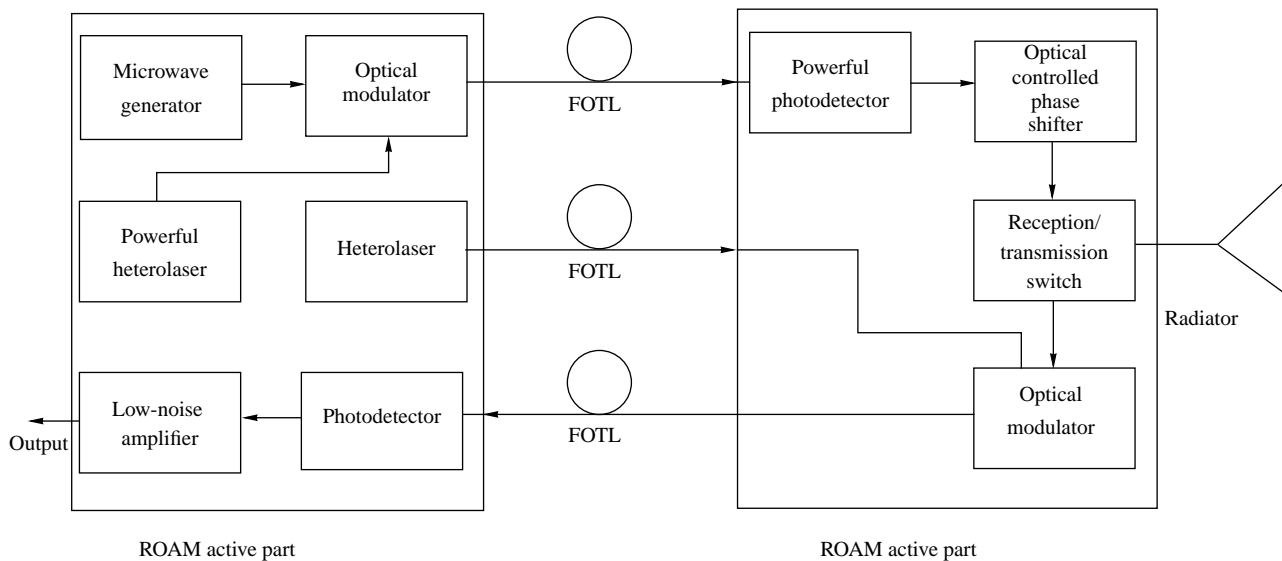
**Fig. 2.** General structure diagram of an ROAM (FOTL is fiber-optic transmission line).

the impossibility of installation onboard antenna systems with a desired aperture and invalidity of the requirements of both the long-range detection and sidelobe level.

Due to the small size of APAA modules and their large number, the use of conventional microwave lines and connectors becomes difficult. At the same time, the number of control and signal channels with their corresponding cables becomes much larger than in the case of a PAA.

There is also the problem of phasing accuracy, which is caused by the insufficient phase thermal stability of waveguides and aging of a dielectric in coaxial cables.

The necessity of providing the internal and external electromagnetic compatibility and stability of the antenna system with respect to electromagnetic pulses is complicated by the highly dense mounting of its components and saturation of the entire volume of a modern aircraft or spacecraft by radio electronic equipment, as well as by the significant total length of the onboard cable network.

It is possible to solve this and other problems and to transform the characteristics of radar stations to a qualitatively modern level using analog-photonics methods[1] [4]. At present, powerful heterolasers with an output power (in the permanent regime) of more than several watts, distributed photodiodes capable of detecting

a large optical power with a high quantum efficiency, modulators providing a noise factor smaller than 0.5 dB up to frequencies exceeding 20 GHz [4], and special optic fibers for transmitting a large optical power are being developed. Because of this, a novel approach to the development of APAA antenna modules of a new type became possible.

Application of analog photonics to PAAs can yield the most noticeable effect in the case of employing distributed radio-optical antenna modules (ROAMs). The principal difference between ROAM and usual APAA modules consists in the spatial separation (based on fiber-optic transmission lines) of the heat-releasing (active) part of an antenna module from the other (passive) part, in which the heat release is negligible.[2] As a result, a ratio of 10 : 1 or higher for the thermal power released in the active and antenna parts of a ROAM can be attained. New achievements in the field of constructing antenna radiators make it possible to extend the operation frequency bands of antenna arrays up to several octaves. This makes it possible to realize in practice the high potentialities of optical methods [5].

Photonics-based methods of controlling antenna directivity patterns allow us to construct antenna arrays of a new type. A possible structural diagram of an ROAM without a control unit is presented in Fig. 2. Here, the active and antenna parts of the ROAM are connected by three analog optical channels. The first fiber-optic line serves for transmitting an intense radio-frequency signal via the antenna radiator. The second optical channel transmits the optical radiation from a

---

[1] Analog (radio-frequency, microwave) photonics is a set of optical, radiophysical, and radio-engineering methods for the transformation, processing, transmission, automated regulation, and synthesis of analog signals, optics playing the principal role. A symbiosis of analog (nondigital) optoelectron devices and optical integrated circuits, analog optical processors with a holographic memory, which are connected by analog fiber-optic transmission lines, are used as component types in analog photonics.

[2] Realization of these modules, which is based on conventional transmission lines has no practical sense due to a high microwave-energy loss in them and unacceptable size, mass and stiffness intrinsic to the structure.
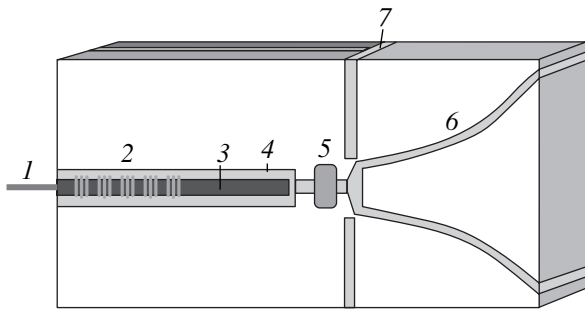
**Fig. 3.** Possible external view from the side of the antenna part for a distributed optical module. (*1*) Optic fiber; (*2*) powerful distributed photodiodes; (*3*) optical waveguide; (*4*) metallization; (*5*) circulator; (*6*) integrated radiator; (*7*) separating screen installed between the transmitting and receiving parts of the module and the receiving part of the module.

A diagram illustrating the view of the exterior part of an ROAM is presented in Fig. 3. The thickness of this part of the module that, as well as the entire module, can be constructed on the basis of integrated-optic technology reaches approximately 1 mm, and the length (without a radiator) and mass are several tens of millimeters and several grams, respectively.

Antenna arrays based on such distributed antenna modules can be called radio-optical phased array antennas (ROPAAs).

Due to the considerably lower mass and smaller size of an ROAM, the entire mass of an antenna array decreases, and the possible number of modules being installed increases. This fact positively affects the basic parameters of antennas and extends the possible field of their application. The main difference of an ROPAA from a usual passive PAA consists in the fact that an array can be constructed in accordance with the parallelism principle (i.e., each vibrator has its own module, as in an APAA). In addition, the part of the antenna module is presented that performs a substantial bulk of APAA module functions in the immediate vicinity of the radiator (Fig. 4). It should be noted that an ROAM is slightly (by approximately several times) inferior modern APAA modules with respect to the calculated output power. However, this disadvantage can be compensated by the installation of a greater number of ROAMs on the antenna plane because of their considerably lesser thickness. Therefore, the total calculated energy potentialities of RAPAAs and modern APAAs can be approximately equal. Owing to the possible application of new highly efficient modulators, the calculated noise factor of ROAM receiving channels (less
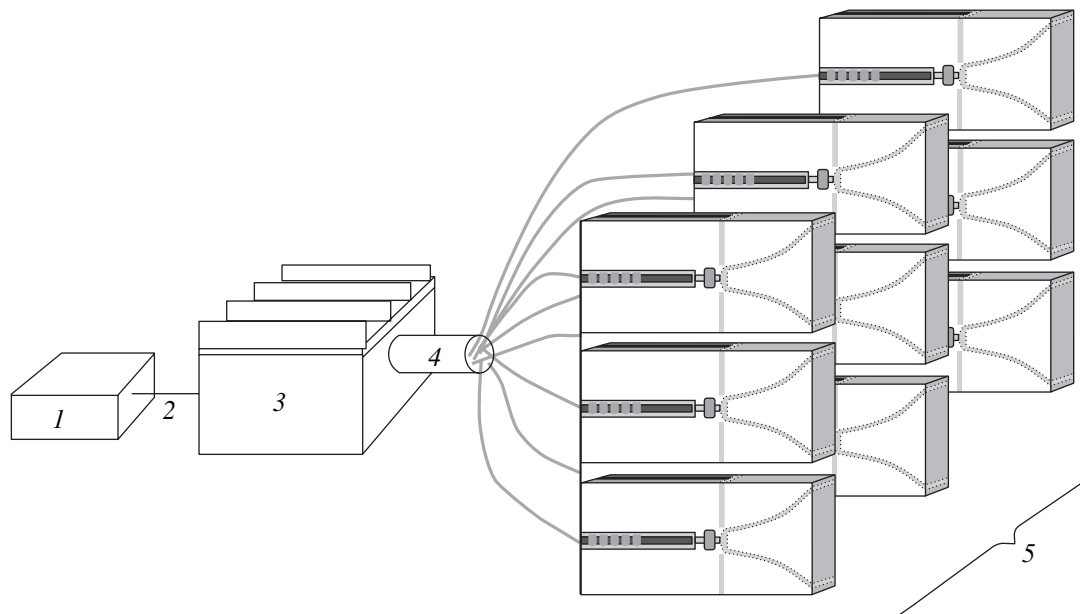
low-noise single-mode heterolaser placed in the active part to a highly sensitive optical modulator. This signal received by the antenna radiator operating in the reception mode modulates the optical radiation. It is further transmitted by the third low-signal optical channel with the single-mode optical fiber to the active part of the ROAM. In this part, the radiation is transformed into a radio-frequency signal or is transmitted for subsequent processing by optical methods.

The control of the ROAM operation can also be performed via analog or digital fiber-optic communication lines using optically switched attenuators, phase shifters, etc.



**Fig. 4.** Fragment of an RAPAA: (*1*) RAPAA control unit; (*2*) optical cable; (*3*) ROAM active-part unit; (*4*) multi-fiber mixed (single-mode and multimode) optical cable; (*5*) antenna array composed of ROAM antenna parts.

than 1 dB) can be considerably lower than that of the corresponding APAA channels (several dB). The rapidly increasing power of heterolasers allows us to assume that the superiority of ROAMs (RAPAAs) with respect the output power will be also attained in several years. RAPAAs can possess a number of advantages compared to conventional PAAs or APAAs. Below, we compare some advantages of APAA cooling systems in modern aircrafts with the proposed RAPAA cooling system.

The advantages of an RAPAA system with respect to conventional PAA and APAA systems are:

the small size of passive parts of distributed RAPAA modules, i.e., a decrease in the total mass and volume of the antenna array;

a decrease in the mass and size of the cooling system at the expense of combining active heat-releasing parts of RAPAA modules with the cooling system;

improvement of reliability and viability of the cooling system and in the RAPAA itself owing to the exclusion of pipelines with volatile freon;

a decrease in spreading distances of composing masses with respect to the system's center of mass, i.e., the elevation in maneuverability;

a decrease in the mass of the power network at the expense of its shortening.

Owing to the advantages listed above, RAPAAs can find wide application in both civil and military fields, including aircrafts and spacecrafts, ground-based mobile carriers, and smart antennas of stationary base stations. There are a number of other fields of applications in which antenna arrays based on RAPAAs can exhibit significant advantages compared to conventional ones.

Thus, we can conclude that the proposed application of ROAMs constructed on the basis of analog photonics and ROAM-based antenna arrays (RAPAAs) can solve a number of problems arising while designing and employing conventional APAAs. In other words, we can attain a new quality of radar stations (owing to the operation of equipment in a superwide frequency band with ultrashort pulses). In this case, we are able to considerably improve a number of other characteristics (e.g., formation of an improved directivity pattern and efficient adaptation in the real-time scale). Most methods necessary for the calculation and optimization of analog optical-fiber transmission lines as applied to APAAs have even been constructed [6, 7]. The industrial development of these systems must lead to multiple reduction of the cost and construction cycle for both antenna modules and antenna arrays in themselves.

## REFERENCES

1. E. Brookner, Microwave J. **40** (5), 288 (1997); **40** (6), 84 (1997).
2. *Advanced Radar Problems*, Ed. by A. V. Sokolov (Radiotekhnika, Moscow, 2003).
3. A. I. Kanashchenkov, V. I. Merkulov, and O. F. Samarin, *Intrinsic Features of Promising Aboard Radar Systems* (Radiotekhnika, Moscow, 2002).
4. D. F. Zaĭtsev, Antenny, No. 5, 34 (2003).
5. L. D. Bakhrakh, N. F. Zhuk, V. F. Los', and A. N. Shimanov, Antenny, No. 2, 21 (2001).
6. D. F. Zaitsev, IEE Proc.-J: Optoelectron. **140**, 227 (1993).
7. D. F. Zaĭtsev, Radiotekh. Élektron. (Moscow) **33**, 612 (1988).

*Translated by G. Merzon*

# Model Description of Crystal Growth in Inhomogeneous Media

## S. O. Gladkov

Presented by Academician N.P. Lyakishev July 23, 2003

Studies of nonequilibrium crystallization in gels with inhomogeneous chemical composition are important not only from the cognitive and pure theoretical viewpoints. This physicochemical process, which is associated with the addition of elementary chemical "building blocks" to a certain stochastically nucleated center of the future solid phase, is clearly irreversible. Indeed, the entropy of a growing crystal (further called "stalactite") increases and is maximal at the termination of the process. At the same time, the energy of adhesion of each elementary chemical block to the stalactite corresponds to an exothermal process, which is accompanied by taking heat from the bulk of the gel. As a result of crystal growth, the gel is cooled. Such cooling was actually observed in experiments.

To obtain a system of dynamic equations describing the growth of the crystal and its shape, we choose the dissipative function $Q$ as a generating functional (some close considerations concerning this choice were given in [1, 2]). It is necessary to take into account that crystal growth in a certain substance is clearly irreversible. In addition, viscosity depends here on the position and changes within the range $\delta x$ about equal to or larger than the size $b$ of an elementary crystallite, which is a building block for the crystal bulk. This behavior is typical for any non-Newtonian liquid (in the temperature range close to the crystallization point). In other words, as a working model, we assume that these crystallites adhere, due to diffusion, to a fluctuation-nucleated domain that has a higher density and lower temperature and where the future crystal nucleus is formed at nonzero viscosity gradient $\nabla \eta$. To take into account the vector nature of adhesion, we assume that each crystallite is characterized by velocity $\mathbf{v}(\mathbf{x}, t)$ varying at distances of about or larger than its linear size $b$. Let this motion be characterized by the angular momentum $\mathbf{M}(\mathbf{x}, t)$. The description of crystallization dynamics in terms of vector $\mathbf{M}$ is also supported by strong deviation

from the spatial isotropy in the glasslike bulk and the anisotropy characterizing the development of crystals.

The inclusion of parameters $\mathbf{v}$, $\mathbf{M}$, and $\nabla \eta$ in the dissipative function constructed implying that it is not invariant under time reversal leads to the functional

$$Q\{\mathbf{M}\} = \frac{1}{2\tau\eta_0} \int B^*_{iknm} M_i M_k v_n \nabla_m \eta \, dt d^3 x + \dots, \quad (1)$$

where $\eta_0$ is the constant of viscosity dimension, $\tau$ is the constant of time dimension, and $B^*_{iknm}$ is the fourth-rank tensor. Note that Eq. (1) involves only the first term, which turns out to be sufficient to solve the formulated problem.

Varying this expression with respect to the components of the angular momentum and using the phenomenological equation $\dfrac{d\mathbf{M}}{dt} = \dfrac{\gamma \delta Q}{\delta \mathbf{M}}$, where $\gamma$ is the constant providing the appropriate dimension, we obtain

$$\dot{M}_i = B_{iknm} M_k v_n \nabla_m \frac{\eta}{\eta_0}, \quad (2)$$

where $B_{iknm} = \gamma B^*_{iknm}$.

Let us analyze Eq. (2) in the very important particular case where it can be represented in the form

$$\dot{\mathbf{M}} = \frac{1}{\eta_0} [\mathbf{M}[\mathbf{v}\nabla\eta]], \quad (3)$$

where $\eta_0$ is the constant of viscosity dimension (g/(cm s)), which is inversely proportional to the square of the interaction energy between the nucleus (playing the role of the attracting set) and the elementary building chemical compound of mass $m$, $\mathbf{M}$ is their angular momentum, and $\eta$ is the absolute viscosity of the gel obeying the Vogel–Fulcher law

$$\eta = \eta^* \exp \frac{\Delta}{|T - T_{cr}|}.$$

Here, $\Delta$ is the energy barrier and $\eta^*$ is the dynamical viscosity of the crystalline compound, which is equal

*Moscow State Regional University,*
*ul. Radio 10a, Moscow, 105005 Russia*
*e-mail: sglad@newmail.ru*

by the order of magnitude to $\dfrac{J_{ex}a^2\rho}{\hbar}$, where $a$ is the interatomic distance, $\hbar$ is Planck's constant, $J_{ex}$ is the energy of the exchange interaction between atoms, $\rho$ is the crystal density measured in g/cm³, and $T_{cr}$ is the crystallization temperature. The addition of elementary building chemical compounds to the main nucleus is responsible for its dynamic growth through the diffuse-adhesion mechanism. In connection with this, we emphasize that the diffusion mechanism has a significant drawback (namely, a limited applicability range), which is absent in the synergetic theory of crystal growth discussed here. Indeed, in contrast to the diffusion approximation, Eq. (3) has no limitations to the linear sizes of stalactites and, hence, describes the most general case of crystal development.

According to Eq. (3), the scalar product $\mathbf{M}\dfrac{d\mathbf{M}}{dt}$ is identically equal to zero; i.e., the absolute value $|\mathbf{M}|$ of the total angular momentum is conserved.

Since $\mathbf{M} = m[\mathbf{vr}]$, Eq. (3) can be written in the form

$$\frac{d\mathbf{M}}{dt} = \mathbf{v}(\mathbf{Mg}), \qquad (4)$$

where $\mathbf{g} = \dfrac{\nabla\eta}{\eta_0}$. Let us consider solutions of this equation for the case $\mathbf{g} = (0, 0, g)$. In this case, we obtain the set of equations

$$\begin{aligned}
\ddot{y}z - \ddot{z}y &= g\dot{x}(\dot{x}y - \dot{y}x), \\
\ddot{z}x - \ddot{x}z &= g\dot{y}(\dot{x}y - \dot{y}x), \\
\ddot{x}y - \ddot{y}x &= g\dot{z}(\dot{x}y - \dot{y}x).
\end{aligned} \qquad (5)$$

Using cylindrical coordinates $x = r\sin\varphi$, $y = r\cos\varphi$, $z = z$, we obtain $\dot{x}y - \dot{y}x = -r^2\dot{\varphi}$.

From the first two equations of set (5), it follows that

$$z(\ddot{x}x + \ddot{y}y) - z(\dot{x}^2 + \dot{y}^2) = g(\dot{x}y - \dot{y}x)^2$$

and, hence,

$$z(\ddot{r} - r\dot{\varphi}^2) - \ddot{z}r = r^3\dot{\varphi}^2g. \qquad (6)$$

From the last equation of set (5), we find

$$\frac{d(r^2\dot{\varphi})}{dt} = g\dot{z}r^2\dot{\varphi}. \qquad (7)$$

Hence, $r^2\dot{\varphi} = C_1\exp\{gv_0t\}$, where $C_1$ is the integration constant. Assuming that the angular velocity is constant, i.e., $\dfrac{d\varphi}{dt} = \omega = $ const, we find the solution

$$r = r_0\exp\frac{gz}{2}, \qquad (8)$$

where $r_0 = r\,(t = 0)$.

In this case, Eq. (6) is also simplified and becomes very simple under the assumption that the crystal growth rate along the $z$ axis is constant: $\dfrac{dz}{dt} = v_0 = $ const, which physically means the uniform growth of the independent $z$ component of the surface (directed along the axis of the stalactite). Therefore, $\dfrac{d^2z}{dt^2} = 0$ and Eq. (6) gives

$$\ddot{r} - r\omega^2 = r^3\omega^2\frac{g}{v_0t}. \qquad (9)$$

Hence, $\dfrac{d^2r}{dt^2} - r\omega^2 = 0$ at $t \to \infty$ and the corresponding solution reads

$$r(t) = C_1e^{-|\omega|t} + C_2e^{|\omega|t}, \qquad (10)$$

where $C_1$ and $C_2$ are the integration constants.

It is obvious that only the solution with $C_2 = 0$, i.e., $r(t) = C_1e^{-|\omega|t}$, can be physically meaningful because the amount of the substance (in our case, lead) is limited. Comparing this solution with solution (6), we arrive at the following linear relationship between the "twisting" frequency and viscosity gradient:

$$|\omega| = |g|\frac{v_0}{2}. \qquad (11)$$

Now, let us analyze the solution of Eq. (9) with the nonlinear right-hand side. By the substitution $r = At^{1/2}u$, where $A = 0.5\left(\dfrac{3v_0}{|g|}\right)^{1/2}$ and $u(t)$ is the new unknown function, we transform Eq. (9) to the equation

$$\tau^2u'' + \tau u' + 0.5\left(\tau^2 - \frac{1}{2}\right)u = 0.75\tau^2u^3, \qquad (12)$$

where $\tau = \omega t$ is the new argument.

For small $u$ ($u \ll 1$), we can transform Eq. (12) to the Bessel equation

$$x^2u'' + xu' + \left(x^2 - \frac{1}{4}\right)u = 0, \qquad (13)$$

where $x = \dfrac{\tau}{2^{1/2}}$ and prime means differentiation with respect to $x$.

A solution to Eq. (13) is $u(x) = c_1J_{1/2}(x) + c_2J_{-1/2}(x)$, or in the old notation,

$$u(\tau) = c_1J_{1/2}\left(\frac{\tau}{\sqrt{2}}\right) + c_2J_{-1/2}\left(\frac{\tau}{\sqrt{2}}\right), \qquad (14)$$

where $c_1$ and $c_2$ are the integration constants.

(a)



$X$

(b)



$X$

(c)



$X$

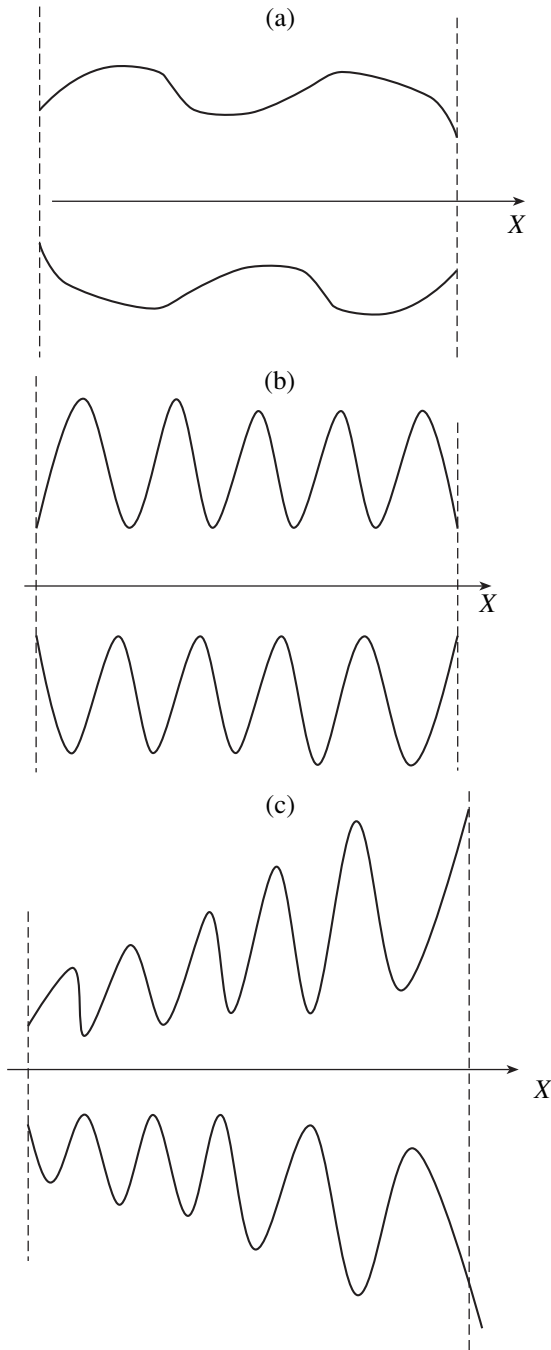**Fig. 1.** Nuclear radius $r(\varphi)$ given by Eq. (16) for (a) $\omega t < 1$ and (b) $\omega t \gg 1$ and (c) by Eq. (20) for $\omega t > 1$. These plots predict three different possibilities for twisting surfaces, and $X$ is the polar axis.

Since $J_{1/2}(\xi) = \left(\dfrac{2}{\pi\xi}\right)^{1/2} \sin\xi$ and $J_{-1/2} = \left(\dfrac{2}{\pi\xi}\right)^{1/2} \cos\xi$, we find from Eq. (14) that

$$u(\tau) = \left(2\sqrt{\frac{2}{\pi\tau}}\right)^{1/2}\left[c_1\sin\frac{\tau}{\sqrt{2}} + c_2\cos\frac{\tau}{\sqrt{2}}\right]. \quad (15)$$

Therefore, the sought time dependence of the stalactite radius can be written as

$$r(t) = At^{1/2}u = B\left(\frac{3v_0}{\pi|\omega||g|\sqrt{2}}\right)^{1/2}\sin\left(|\omega|\frac{t}{2} + \varphi_0\right), \quad (16)$$

where $B$ and $\varphi_0$ are new constants introduced in place of $c_1$ and $c_2$.

Figures 1a and 1b schematically show Eq. (16) as a function of rotation angle $\varphi = |\omega|t$.

Let us analyze now a solution to Eq. (12) in the case of large argument $\tau$ ($\tau \gg 1$). In this case, we arrive at the asymptotic equation

$$u'' + u = 1.5u^3. \quad (17)$$

We emphasize that the condition $\tau \gg 1$ can easily be met in actual physical experiment, for example, if frequency $\omega$ is high or the time intervals are long. This is possible when temperature $T$ is close to the crystallization temperature $T_{cr}$. The first integral of Eq. (17) has the form

$$u' = (0.75u^4 - u^2 + C^*)^{1/2}, \quad (18)$$

where $C^*$ is the integration constant. Setting it to zero and integrating Eq. (18), we find

$$u(\tau) = \frac{2}{\sqrt{3}\cos\left(D + \dfrac{\tau}{\sqrt{2}}\right)}, \quad (19)$$

where $D$ is the new integration constant.

Since we consider large $\tau$ ($\tau \gg 1$), a solution to Eq. (19) is a rapidly oscillating function and the time dependence of the nucleus radius $r(t)$ looks like an array of sharp needles. According to the definition, $r = At^{1/2}u$; hence,

$$r(t) = \left(\frac{v_0 t}{|g|}\right)^{1/2}\left[\cos\left(D + \frac{|\omega|t}{\sqrt{2}}\right)\right]^{-1}. \quad (20)$$

According to this solution, the radius of the nucleus is an increasing function with the envelope proportional to $t^{1/2}$. Such a development of the nucleus is possible if the amount of the crystallizing substance in the gel is sufficient. However, such growth cannot continue infinitely and must stop when the crystallizing component in the gel disappears.

The behavior of this solution is qualitatively illustrated in Fig. 1c for the case $\omega t > 1$.

The solution to Eq. (20) leads us to the conclusion that the shape of the surface is spiked and twisting. Its twisting is determined by the direction of angular velocity $\omega$ characterizing the "winding" of chemically active elementary blocks onto the arising nucleus of the solid phase.

We also emphasize that the qualitative solution discussed above supports the validity of the initial assump-

tions, but it is not exact because it was found from the asymptotic nonlinear equation (17). The exact surface shape can be determined only by numerical integration of Eq. (12). Therefore, it is a separate problem to find the surface shape analytically in the general case.

We discussed above a quite simple case where both crystal growth rate $\frac{dz}{dt}$ and angular velocity $\omega$ were assumed to be constant. Therefore, it is interesting to analyze the set of Eqs. (3) [or Eqs. (4)] with nonlinear behavior of $z(t)$ and $\omega(t)$.

When the coordinate $z$ and angle $\varphi$ are linear functions of the parameter $t$, solution (8) at $g < 0$ determines the surface of the stalactite as a needle of length $L = \frac{2}{|g|}$. Since $|g| = \frac{|\nabla \eta|}{\eta_0}$, length $L$ is physically determined by the square of the interaction between elementary chemical blocks and the attracting set $\left( \text{parameter } \frac{1}{\eta_0} \right)$, i.e., the domain of the fluctuation-induced nucleation of the crystal center.

This problem was also considered in, e.g., [2]. The mathematical description of other strongly disordered structures was also discussed in [3].

In conclusion, we note the following:

(1) a synergetic model of crystal growth in inhomogeneous gels was suggested;

(2) a set of nonlinear differential equations was analyzed and the shape of crystallizing nuclei was described;

(3) an asymptotic solution to the nonlinear equation was found and a nontrivial sharp-needle shape of the surface was predicted for the growing crystal;

(4) a physical mechanism responsible for limitation of the growth of the stalactite was revealed and the length of such a stalactite was found.

## ACKNOWLEDGMENTS

## REFERENCES

1. S. O. Gladkov, Dokl. Akad. Nauk **391**, 610 (2003) [Dokl. Phys. **48**, 405 (2003)].
2. S. O. Gladkov, *Physics of Composites: Thermodynamic and Dissipative Properties* (Nauka, Moscow, 1999).
3. S. O. Gladkov, *Dielectric Properties of Porous Media* (Springer-Verlag, Berlin, 2003).

*Translated by K. Kugel*

# Rupture and Dynamic Hardness of Ice

## V. P. Epifanov

Presented by Academician S.S. Grigoryan October 14, 2003

Received October 14, 2003

It is known that the ultimate tensile strength $\sigma_u$ is proportional to dynamic hardness [1]:

$$\sigma_u = 0.383H.$$

Correspondence of the model proposed in [1] to real fracture conditions is determined experimentally. However, the appropriate mechanical test procedures for ice are insufficiently developed.

Imperfection of the available tension procedure is associated with the appearance of the bending moment, stress concentrations at the fastening points of samples, and initial slackness of loading systems. These factors are responsible for the distortion of the tension diagram even in its initial section [2, 3].

In this work, the scheme and conditions of loading are taken so as to monitor the processes of deformation and fracture, because deformation changes in structure prepare fracture and determine the strength properties.

Dumbbell-shaped ice specimens were tested on an FM250 tensile machine. For a strain rate of $\dot{\varepsilon} = 0.005$ s$^{-1}$ and a temperature of –8°C, reproducible ultimate strengths $\sigma_u = 10.0 \pm 0.2$ MPa were determined for seven specimens of fine-crystalline congelation ice. Coaxiality of a specimen and tensile force at the initial time was ensured by self-centering clamps [4]. In addition to obligatory control of the initial structure and check of uniformity of acoustic characteristics, specimens were "annealed." Despite careful preparation, as in most experiments carried out by other authors, the loading diagram begins with a nonzero value and the fracture of a specimen occurs suddenly with the fracture surface characteristic for bending.

In the next experimental run, a dumbbell-shaped ice specimen was placed into a cylindrical vessel. The gap between the lateral surface of the ends of the specimen and inner surface of the vessel was sealed by introducing water and its freezing. The specimen was extended by supplying a viscous liquid under pressure to the nar-

row central section of the specimen. The pressure of the liquid caused tensile stress in the specimen. In order to increase accuracy, the inner surface of the vessel was made of a material with the minimum coefficient of friction. In order to avoid the Rebinder effect, the narrow section of the specimen was insulated from the liquid by an elastic shell with cuffs. To monitor deformation processes and accumulation of damage in the specimen in the process of tension, a transmitter and receiver of ultrasonic vibrations were frozen to the ends of the specimen [5].

In such a scheme, mechanical clamps are absent, preliminary loading is not necessary, and acoustic contact remains unchanged in the tension process. Owing to these circumstances, monitoring is more reliable than that for compression, particularly for small stresses [6]. However, the requirements for the geometry of the specimen and tolerances remain stringent [4].

Fracture occurs in the working part of the specimen. If the tension axis coincides with the $C$ axis of crystallites, e.g., in "column" ice, the fracture surface is perpendicular to the tension axis and the surface relief is smooth with a roughness of less than $6.2 \times 10^{-9}$ m. The fine structure of the fractogram conserves manifestations of the mechanism of the growth of the main crack. In particular, interaction of the crack front with an elastic wave arising when the specimen breaks (Fig. 1) is manifested as numerous broken straight lines with parallel sections.

Figure 2 shows the phases of the main-crack growth under a constant tensile force in real time. For shooting, specimens of transparent river ice (A4) with a standard central circle cut were used. The first frame in Fig. 2 corresponds to the stressed state in the specimen before the breakdown of continuity. First cracks shown by arrows (2) arise inside the specimen. The growth of the main crack begins $\Delta\tau \leq 0.2$ s after internal fracture. This process is quite slow and continues for almost 4.5 s in the sequence (2–8).

First, the front propagates along the circle cut (2–4). Second, it stops and its velocity turns by 90°. After the turn, the crack grows smoothly in the radial direction (5). The presence of the primary cracks is manifested only as the front approaches, when the break and confluence of cracks occur (5). The mean velocity of the crack over

*Institute for Problems in Mechanics,*
*Russian Academy of Sciences,*
*pr. Vernadskogo 101, Moscow, 117526 Russia*
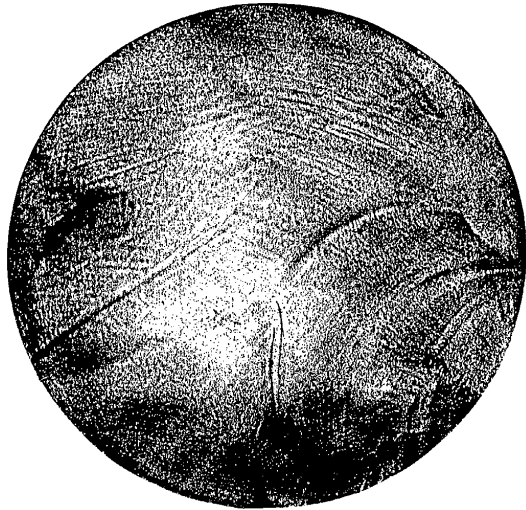*e-mail: evp@ipmnet.ru*

**Fig. 1.** Fine structure of the ice fracture surface.

Since the main-crack front first propagates along the circle cut, the end region can be treated as a peculiar structure after the formation of which the vector of the crack front changes its direction to orthogonal. The process includes two mechanisms and two characteristic energy-dissipation rates: the crack propagation rate and crack-healing rate. Further experiments in a wide range of temperatures and loading rates will probably reveal what occurs in this case, how the geometry of cracks changes, and how they compete with each other.

From the above discussion, it is obvious that the fracture of ice has specific features which have not yet been revealed for other materials. Moreover, it is noteworthy that the circle shape of the outer contour of the section changes at the stage of the intense growth of the main crack, which testifies to the pronounced nonuniformity of the stress field in the section under consideration. We note that the first sites of breaking continuity, which are likely caused by the redistribution of the stress field, are not further manifested as stress concentrators, because they are healed.

the cut contour is equal to about 7 mm/s and, after the turn, 30 mm/s.

The initial internal fracture of continuity and further nonuniform growth are nontrivial because the circle cut is quite sharp ($D \leq 0.01$ mm), and the crack growth from it could be expected.

The new procedure was first applied to test specimens of river congelation ice with density $\rho_{-11°C} = 0.89 \pm 0.01$ g/cm$^3$, crystallite size $\overline{D} = 1.5$ mm, speed of longitudinal-wave propagation $V_{-11°C} = 3784$ m/s, and absorptivity $\alpha_{-11°C} = 0.22$ cm$^{-1}$ at a frequency of 1 MHz. Stepwise loading was carried out with a step of
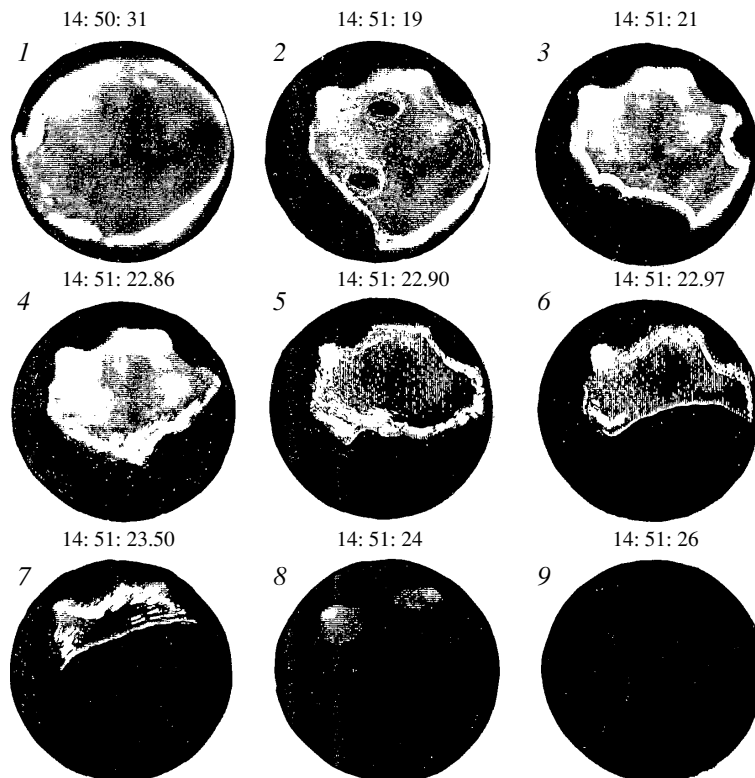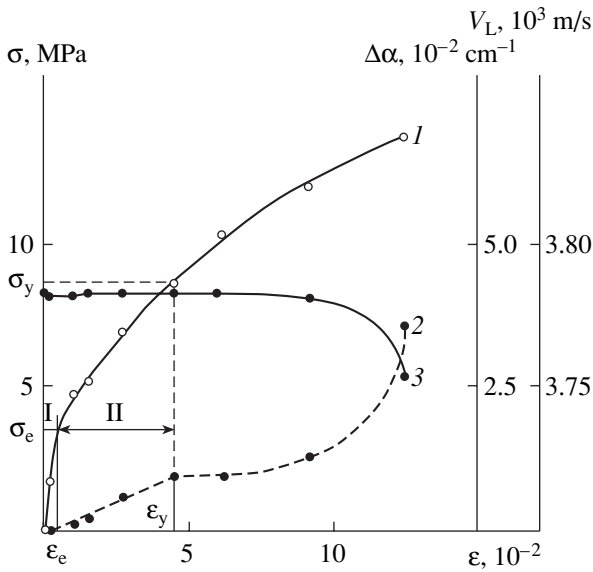


**Fig. 2.** Phases of main-crack growth.

**Fig. 3.** Tensile-strain dependence of (*1*) stress, (*2*) excessive absorption $\Delta\alpha = \alpha_{\sigma j} - \alpha_{\sigma = 0}$, and (*3*) longitudinal-wave velocity. The regions of the amplitude-dependent and amplitude-independent mechanisms of ultrasound absorption are indicated by I and II, respectively.



**Fig. 4.** Brinell hardness $H$ as a function of the bedding depth $Z$ and horizontal displacement $X$ for a transition layer of river ice (from A9 to A4) with various scales of averaging experimental data.

1.742 MPa every 10 min at a temperature of –5.3°C. Under loading, the specimen is ultrasonically tested along the tension axis.

Figure 3 shows the typical strain dependences of (*1*) stress, (*2*) excessive absorption, and (*3*) the velocity of the longitudinal wave with a frequency of 1 MHz. Line *1* differs substantially from the tension diagram obtained in [2]. First, line *1* passes through the origin, and the "input" section is free of the "pulling" characteristic for traditional loading schemes, where it usually appears likely due to slackness. Our procedure allows both the measurement of small strains in the initial loading section and investigation of ice elasticity. Second, the shape of stress–strain curve *1* is similar to ice compression diagrams. The boundaries of traditionally separated regions of deformation are determined by the bend points of line *2*, which characterize the change in the mechanisms of deformation and accumulation of deformation defects. Thus, the determined elastic limit and yield point are equal to $\sigma_e = 3 \pm 0.3$ MPa, $\varepsilon_e = 3 \times 10^{-3}$ and $\sigma_y = 8.7 \pm 0.3$ MPa, $\varepsilon_y = 4.5 \times 10^{-2}$, respectively. In addition to reversible displacements of oxygen ions in the crystalline lattice, macroelasticity includes reversible displacements of microdefects within a crystallite, i.e., local microplasticity. The yield point is considered as the spreading of microplastic deformation to the carrying section of the specimen.

The accumulation of microdamage reduces the elastic characteristic of ice (Fig. 3, line *3*). According to acoustic measurements, the transparent part of river ice originally includes $10^{-5}$-m-long dislocations with a density of $10^6$ m$^{-2}$. At the yield point, their length is at least doubled and their concentration increases by a factor of several thousand. Deformation changes in the structure, which prepare fracture, are most clearly manifested before the fracture of the specimen, when the dissipation of the elastic energy is maximal (line *2*).

The yield stress (Fig. 3) $\sigma_y = 13.9 \pm 0.6$ MPa and modulus calculated by secant $E \approx 1$ GPa are much larger than the respective values obtained in the traditional loading scheme. Therefore, the bending moment arising in our experiments is negligibly small. Small bending and constraint are necessary conditions for experiments with the tension of ice.

The above discussion shows that the value obtained for the ice strength can be compared with the dynamic hardness of ice.

Figure 4 shows the preliminary results for the river-ice hardness measured by means of a spherical indenter 1 mm in diameter at the static regime. It is seen that the effect of the microinhomogeneity of ice on its spatial variability is pronounced and the scale clearly affects the mechanical and fracture properties (breakdown viscosity) [7]. The parameters of a loading dynamic machine were chosen by experimentally varying the indenter diameter, as well as time and force of indention.
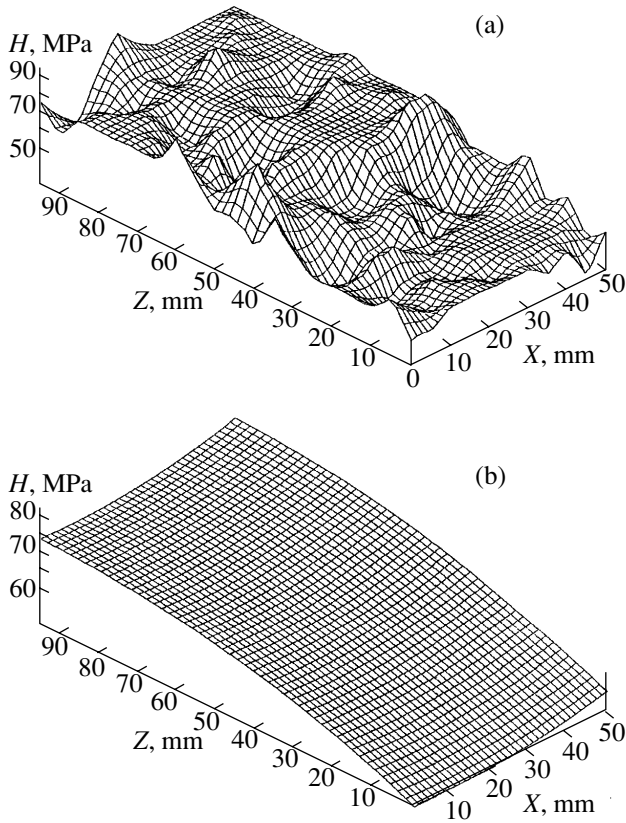
The average contact pressure was determined by means of a spherical indenter whose radius was equal to $R = 40$ mm and which was equipped with accelerometer [8]. The initial collision velocity, impact energy, and amplitude were equal to 2.3 m/s, 0.089 J, and 650 N, respectively. The spread of measurements for the homogeneous material did not exceed 0.6%. The loading time and measurement accuracy were equal to $10^{-4}$ s and 5%, respectively.

According to measurements, the dynamic hardness and ultimate tensile strength $\sigma_u$ of congelation ice at a temperature of –5°C are equal to 35.6 MPa and 13.9 ± 0.6 MPa, respectively. Therefore, the strength-to-hardness ratio is equal to 0.39 ± 0.02, which agrees well with the theoretical value.

Thus, we determine the conditions under which the theoretical model proposed in [1] adequately reproduces real processes of ice fracture. The pattern of the accumulation of deformation damage at early loading stages is supplemented by the properties of fracture under ultimate stresses. The results can be used for express estimates of the strength properties of natural ice under the conditions of its bedding.

## REFERENCES

1. A. Yu. Ishlinskiĭ, Prikl. Mat. Mekh. **8**, 201 (1944).
2. V. V. Lavrov, Dokl. Akad. Nauk SSSR **162**, 54 (1965) [Sov. Phys. Dokl. **10**, 429 (1965)].
3. D. M. Cole and L. D. Gould, Cold Reg. Sci. Tecnol. **18**, 295 (1990).
4. I. Yu. Voronina and V. P. Epifanov, Izv. Akad. Nauk SSSR, Mekh. Tverd. Tela, No. 5, 184 (1983).
5. V. P. Epifanov, USSR Inventor's Certificate No. 1518712 G01, Byull. Izobret., No. 40 (1989).
6. V. P. Epifanov, Dokl. Akad. Nauk SSSR **267**, 1364 (1982) [Sov. Phys. Dokl. **27**, 1063 (1982)].
7. J. Weiss, Surv. Geophys. **24**, 185 (2003).
8. V. P. Epifanov, Dokl. Akad. Nauk SSSR **284**, 599 (1985) [Sov. Phys. Dokl. **30**, 799 (1985)].

*Translated by R. Tyapaev*

## ASTRONOMY, ASTROPHYSICS, COSMOLOGY

# The Origin of Anomalous Disturbances in the Heliosphere and Their Geophysical Manifestations

## Academician G. A. Zherebtsov, V. A. Kovalenko, and S. I. Molodykh

Received July 17, 2003

It is established that long-term variations of both the large-scale and global magnetic fields in the solar atmosphere are nonmonotonic. The existence of periods of fast global changes on the Sun is found in each 11-year cycle of solar activity. These variations are accompanied by anomalous manifestations in both the heliosphere and the geomagnetic field. These periods are regularly repeated in each cycle of solar activity. They are characterized by elevated flaring activity that reflects fast variations of magnetic structures. The concept of universality of physical processes, which includes interactions of different-scale magnetic fields in the solar atmosphere and manifestations of these processes in the solar atmosphere, is developed. This concept is confirmed by the comprehensive analysis of helio-geophysical data.

In accordance with the model of the solar-wind formation [1–3], properties of the heliosphere such as the space-time distribution of the solar wind velocity, the particle flux, and the interplanetary magnetic field are determined by large-scale solar magnetic fields existing on and by their dynamics. The origin of the large-scale inhomogeneities in the solar wind are of particular interest. On the one hand, they are manifestations of the solar variability in interplanetary space. On the other hand, they are the principal cause for disturbances of the geomagnetic field. The basic sources of the inhomogeneities are coronal holes, solar flares, and coronal mass ejections. Studies of these ejections are important for both understanding the formation mechanisms of the unsteady solar wind and predicting the space weather conditions, because the strongest geophysical disturbances are associated with sporadic phenomena occurring on the Sun. In [1, 2], periods of fast global variations of the solar magnetic fields were discovered. These variations are characteristic of each 11-year cycle of solar activity and are accompanied by anomalous disturbances of the solar wind, interplanetary mag-

netic field, cosmic-ray intensity, and geomagnetic activity.

Analysis of variations of the solar-wind particle flux based on the data presented in Fig. 1 allows us to reveal their basic regularities stipulated by global changes in the solar corona magnetic structure [3]. Alongside the fluctuations, fast (for 1–2 solar rotations) variations of solar-wind particle flux, i.e., decreases during the rise phase of solar activity and increases during the decreasing phase, are observed. Both phenomena are caused by the global reconfiguration of the magnetic fields in the solar corona and by the corresponding redistribution of the solar-wind mass flow over heliographic latitudes. For the high-velocity solar wind, the variations are accompanied by significant increases in the interplanetary magnetic-field component ($B_z$) perpendicular to the ecliptic plane. During these increases, unsteady processes in the solar corona manifest themselves. Within the periods indicated, the global reconstruction of the corona from the minimal to the maximal type (and vice versa) takes place.

Let us consider how this reconstruction of the magnetic field occurs. Analysis based on the calculations [4, 5] of coronal magnetic fields in the potential-field approximation for the period 1976–2002 shows that, along with slow variations (for 10–12 solar rotations) of the global structure of the magnetic fields in the corona, rapid changes occurring for about two solar rotations also take place. These changes, proceeding during the rise phase of solar activity, correspond to the decay of the unified current system on the Sun and are accompanied by the abrupt decreases of the particle flux in the low-velocity solar wind in the vicinity of the Earth's orbit. They mark the onset of the active interaction of emerging magnetic fields corresponding to the new cycle with those pre-existing in the solar atmosphere.

In the decreasing phase of solar activity, the opposite process is observed. In this period, a considerable amount of both the mass and magnetic field is additionally carried away by unsteady solar-wind streams. The anomalous character of this period is caused by the interaction of large-scale magnetic fields of the Northern and Southern hemispheres and by their merging due to the reconnection process. In this case, the mecha-

*Institute of Solar–Terrestrial Physics,*
*Siberian Division, Russian Academy of Sciences,*
*ul. Lermontova 126, P.O. Box 4026,*
*Irkutsk, 664033 Russia*
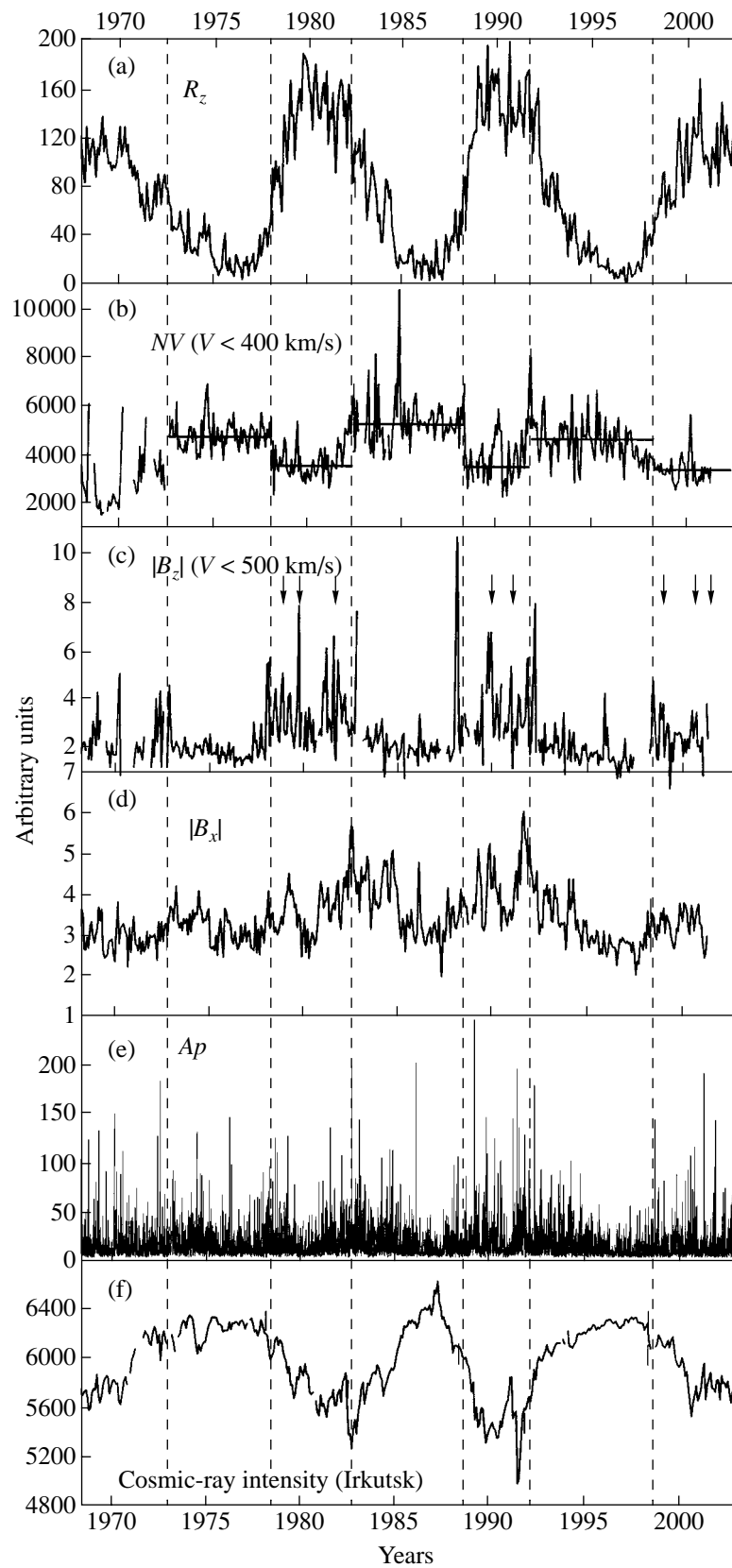*e-mail: uzel@iszf.irk.ru; vak@iszf.irk.ru; sim@iszf.irk.ru*

**Fig. 1.** (a) Monthly average values of Wolf numbers; (b) particle flux for a low-velocity solar wind; (c) modulus of the $B_z$ component of the interplanetary magnetic field for a high-velocity solar wind; (d) modulus of the $B_x$ component of the interplanetary magnetic field; (e) $Ap$ index of the geomagnetic activity (diurnal values); (f) cosmic-ray intensity. Periods of fast reconstructions of the global and large-scale magnetic fields on the Sun are marked by vertical dashed lines and by arrows, respectively.
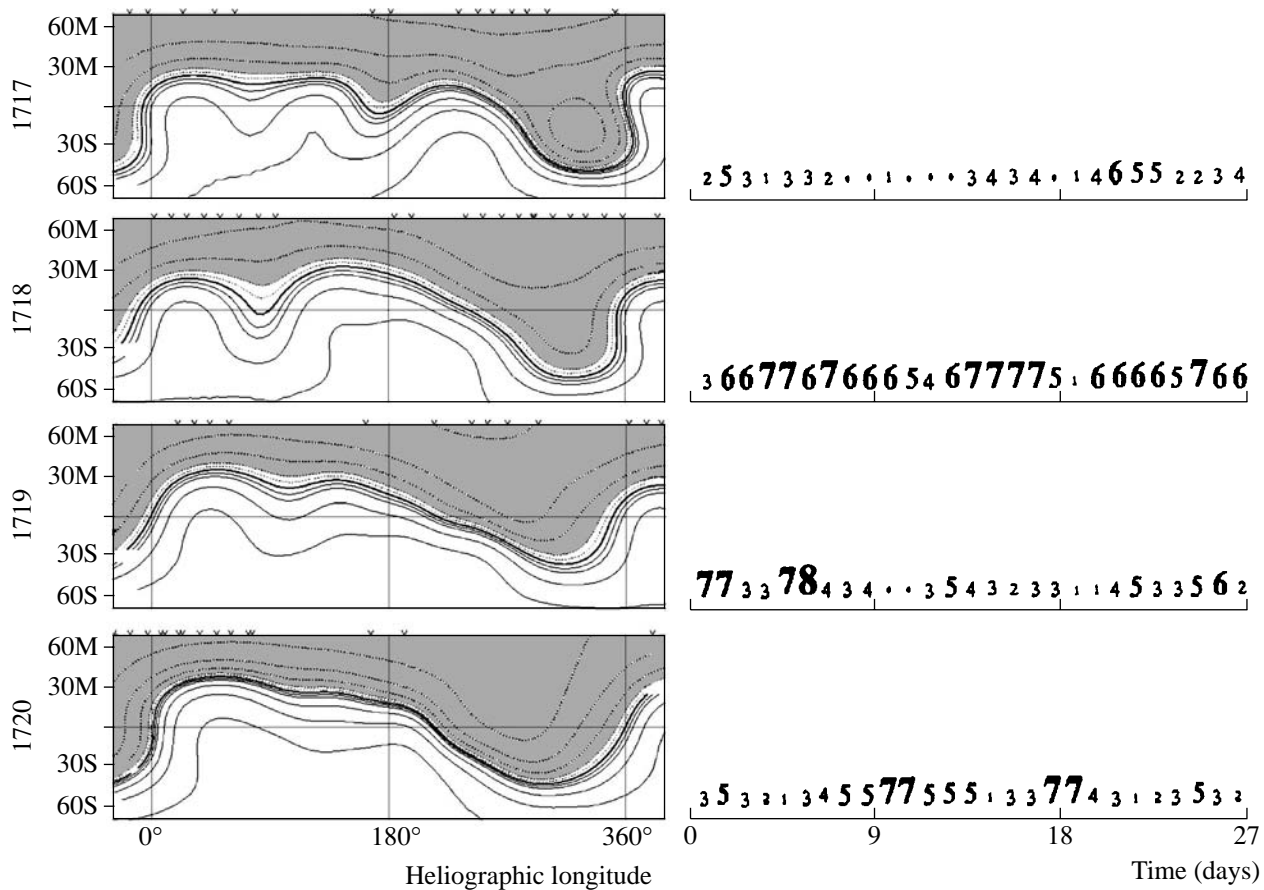
**Fig. 2.** Example of the variation of the solar-corona magnetic structure in the decreasing phase of solar activity (1717th–1720th Carrington rotations, January–April, 1982). On the right, C9 indices of the geomagnetic activity are presented (numbers and their sizes correspond to the index value).

nism of plasma acceleration is similar to that of the formation of transients and magnetic clouds [6].

The data given in Fig. 2 show that, from the 1717th to the 1719th Carrington rotations, a significant variation of the corona's magnetic structure was observed at a distance of $2.5R_\odot$ ($R_\odot$ is the solar radius). This variation is characterized by both the disappearance of small-scale inhomogeneities and the formation of the corona structure of the minimal type. The response of geomagnetic activity to these events also is quite unique. Strong geomagnetic disturbances were observed almost continuously from January 30 to March 2, 1982. According to the Wolf numbers, solar activity virtually did not change within this period.

Variations of the cosmic-ray intensity is a sensitive indicator for global changes of heliosphere properties. Among long-term variations of the cosmic-ray intensity, periods of fast global variations of magnetic fields on the Sun manifest themselves most clearly in the decreasing phase of each cycle of solar activity (1982, 1991, 2001, Fig. 1). The recovery of the cosmic-ray intensity, which started in the phase of solar-activity decay, is interrupted by an anomalously sharp decrease characterized by an unusually rigid spectrum of varia-

tions [1]. This implies that changes in global magnetic structure on the Sun and, correspondingly, in the heliosphere are responsible for anomalous cosmic-ray intensity decreases occurring within these periods.

In the period of maximal solar activity, variations of large-scale magnetic fields also are of a nonmonotone nature. In the period under consideration (1972–2002), fast variations of the global magnetic structure in the solar corona and their manifestations that occurred in 1989, 2000, and 2001 are of particular interest. In 1989, for two solar rotations, the polarity of the solar magnetic field changed practically at all latitudes and longitudes. The fast variation of the global magnetic structure in the solar corona coincides with the anomalous phenomenon in cosmic rays that occurred on September 29, 1989, for which not only a high intensity of the particle flux but also an unusually rigid spectrum and the large magnitude of the maximum particle energy (tens of GeV) were observed. According to data of ground-based observations, this increase was the largest for the last three cycles of solar activity and is comparable only with the unique outburst of solar cosmic rays on February 23, 1956. Apparently, these are fast variations of strong magnetic fields in the large-scale
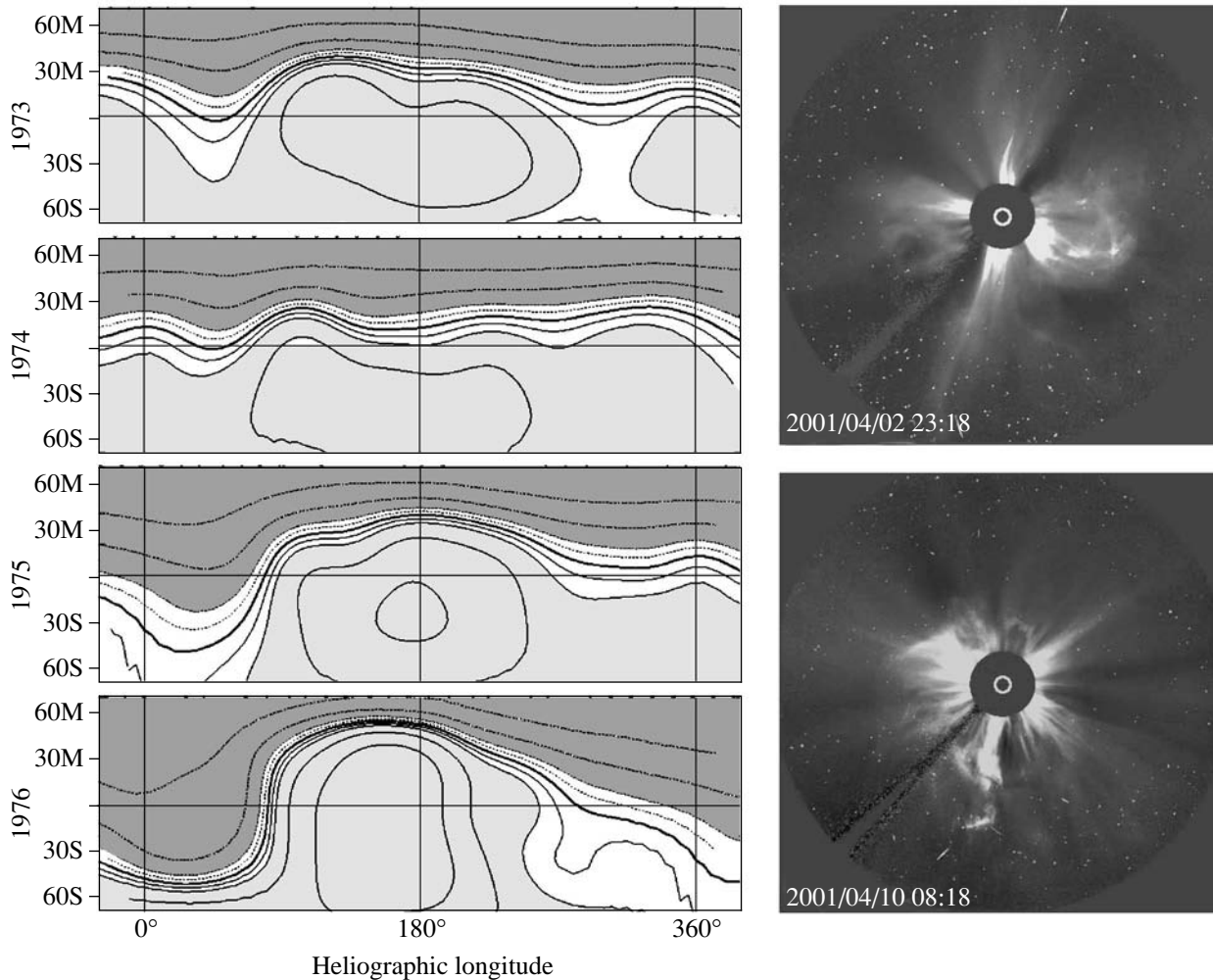
**Fig. 3.** Variation of the solar-corona magnetic structure (1973rd–1976th Carrington rotations, February–May, 2001). On the right, images of the solar corona at solar altitudes of $2.5R_\odot$ and $5R_\odot$ are shown. The images were obtained with the help of the LASCO at the SOHO observatory.

electromagnetic structure of the solar corona that form favorable conditions for the efficient acceleration of intense fluxes of high-energy solar cosmic rays. This conclusion is confirmed by the analysis of global magnetic-structure variations, which was performed using synoptic maps of the Sun in the $H_\alpha$ line within the period of solar cosmic-ray flare on February 23, 1956. Similar variations related to regions of a considerably smaller scale were also observed in both 2000 and 2001.

The data presented in Fig. 3 show that the stable global structure of magnetic fields in the solar corona considerably changed for one solar rotation. The consequence of this phenomenon is a wide range of large-scale intense ejections of coronal plasma, which were observed by the SOHO observatory (see Fig. 3, on the right). Significant ejections of the coronal mass, which involve noticeable latitudinal zones, have been registered for various latitudes and longitudes. According to the flare activity, this period was unique for the entire current cycle. From March 20 to April 17, 2001, 57 flares of importance $M$ and 8 flares of importance $X$ occurred. In addition, an increase of intensity of high-energy solar cosmic rays and a long-lasting magnetic storm were observed on April 15, 2001.

Thus, the strongest heliophysical and geophysical disturbances are caused by fast global variations of magnetic fields on the Sun. On the basis of the analysis of observational data, it is possible to formulate a unified concept, propose a scenario of fast variations, and reveal basic physical processes for interaction of magnetic fields in the solar atmosphere. By virtue of the strong conduction of solar-atmosphere plasma, a relatively slow mutual deformation of emerging and pre-existing magnetic fields takes place when the magnetic field emerges from beneath the convective zone. In other words, the formation of a new current system occurs that, on attaining certain conditions, then rapidly decays, releasing a considerable amount of energy. This is stipulated by the fact that, when a new magnetic flux

emerges, the active interaction of magnetic fields in the solar corona begins only after certain critical parameters depending on the configuration of emerging and pre-existing magnetic fields have been attained.

The rapid changes of strong magnetic fields, large-scale magnetic fields, and the global field are accompanied by a solar flare, mass ejection with the acceleration of solar cosmic rays, and the formation of a new structure with ejections of the mass and the magnetic field, respectively. In accordance with this conception, the regular manifestation of the given scenario occurs in the course of a solar activity cycle for both different-scale fields and their totality or sequence. The basic difference consists in space-time scales of the interaction process and in the intensity of a magnetic field involved in the interaction and in features of their manifestation in the solar atmosphere, heliosphere, and on the ground. The main physical mechanism resulting in fast variations of the magnetic fields in the solar atmosphere is the reconnection process.

## REFERENCES

1. G. A. Zherebtsov, V. A. Kovalenko, and S. I. Molodykh, J. Geophys. Res. **102**, 2137 (1997).
2. G. A. Zherebtsov and V. A. Kovalenko, Adv. Space Res. **17**, 335 (1996).
3. V. A. Kovalenko and S. I. Molodykh, Planet. Space Sci. **40**, 741 (1992).
4. J. T. Hoeksema, Adv. Space Res. **11**, 15 (1991).
5. J. T. Hoeksema and X. Zhao, J. Geophys. Res. **97**, 3151 (1992).
6. G. W. Pneuman, Astrophys. J. **265**, 468 (1983).

*Translated by G. Merzon*

========= **MECHANICS** =========

# Asymptotic Features of Axisymmetric Stokes Flow of Viscous Fluid with Intersecting Boundaries

## O. V. Voinov

Presented by Academician G.G. Chernyĭ August 1, 2003

Received August 21, 2003

## INTRODUCTION

Stokes flows of viscous fluids within a corner, which are caused by motion of one of the sides forming the angle, are well known. Tailor has analyzed the flow within a corner between a solid wall and a solid plate moving like a scraper along the angle wall [1]. Moffatt has solved the problem of flow within a corner when one of its sides is the solid wall and, on the other wall, instead of a solid plate, there is a plane free boundary on which the tangential stress is absent [2]. The Tailor–Moffatt problem belongs to the class of plane problems for Stokes equations.

In the present paper, the general axisymmetric problem for fluid flow is analyzed in the case of small Reynolds numbers when the boundary surfaces (the solid's surface and free surface) intersect at a certain angle in a moving line. The contours of these surfaces are curvilinear, which also distinguishes the problem under consideration from the Taylor–Moffatt problem. The goal of the present paper is to find asymptotic regularities in the behavior of both the stream function and stresses in a small vicinity of the intersection line (contact line) of boundary surfaces. It is assumed that in the contact line, there is no mass sources, and a singularity of the stream function is absent. The asymptotic analysis makes it possible to consider an arbitrary axisymmetric Stokes flow with intersecting boundaries.

This general problem has its applications in studies of slow flows while wetting solids by viscous liquids. The solution of the problem can be useful, e.g., for refined description of such flows in calculation of large-scale flows with capillary forces taken into account. As is well known, at a reasonably low velocity of the contact line, the shape of the free surface at large scales can be approximately described by the capillary-statics equation. In particular, this surface can be similar to a sphere provided that mass forces are absent [3]. In this

*Tyumen Branch, Institute of Theoretical and Applied Mechanics, Siberian Division,*
*Russian Academy of Sciences, 625000 Russia*

case, the contact angle can be determined on the basis of the hydrodynamic approach at a small scale near the contact line.

For the small scale, the flow is described by another problem containing a strong nonlinearity. The general approximate solution to this problem is well-known [3–5]. This solution links the shape of the free surface with dynamics of the liquid. It has also been known for a long time [3, 4] that in the case of wetting, flows cannot be described in the framework of traditional hydrodynamics, and while setting problems of wetting dynamics, we should allow for the molecular (i.e., microscopic) scale of the phenomenon. In this setting, an effect of motion of super-thin (precursor) film that advances a macroscopic liquid mass spreaded over the dry surface of a solid (see also the reviews by De Gennes [6] and by the author [7]) also is well known. In studies of hydrodynamics of wetting solids, asymptotic solutions are of significant importance, in particular for perfecting numerical algorithms.

Below, we analyze the problem independently of the indicated applications.

## BASIC EQUATIONS

We introduce Cartesian coordinates $x_1$ and $x_2$ in the symmetry plane with the origin lying in the contact line and with the $x_1$ axis tangent to the solid's surface (see figure). We assume that the $x_1$ axis is directed towards the dry portion of the solid's surface, and that the coordinate system is immobile with respect to the solid.

The fluid velocity is zero at the contour (generatrix) of the solid's surface $S_{\text{sol}}$:

$$v = 0. \tag{1}$$

On the free surface $S$, the normal component of the fluid velocity coincides with the normal velocity of the surface. For calculating the flow characteristics in the small vicinity of the contact line, it is sufficient to approximately assign motion of the free surface $S$. We allow for translational motion of the contour $S$ at the velocity $v_0$ of the contact line and the rotation of the contour. In this case, the kinematic boundary condition
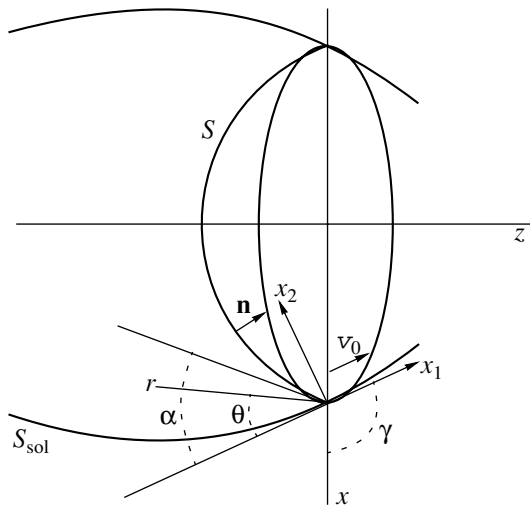
**Figure.**

on the contour $S$ in the limiting case of a small distance $r$ from the contact line can be written out in the form

$$\mathbf{v} \cdot \mathbf{n} = v_0 n_1 + \omega r + \dots. \tag{2}$$

Here, $\mathbf{n}$ is the unit vector of the outer normal to the contour $S$ and $\omega$ is the rotation angular velocity of the tangent to the contour $S$ at the point of the contact line $(r = 0)$.

The tangential stress on the contour $S$ is zero:

$$P_\tau = \boldsymbol{\tau} \cdot \mathbf{P} \cdot \mathbf{n} = 0, \tag{3}$$

where $\mathbf{P}$ is the stress tensor of the liquid and $\boldsymbol{\tau}$ is the vector of the tangent to the contour $S$. Our task is to determine the normal stress on $S$ ($P_n = \mathbf{n} \cdot \mathbf{P} \cdot \mathbf{n}$).

We now consider the cylindrical coordinate system $x, z$, where $x$ is the distance from the symmetry axis and $z$ is the coordinate along this axis. The points $x = x_0$ and $z = 0$ correspond to the contact line.

The components of the fluid flow velocity are expressed in terms of the stream function $\psi$:

$$v_x = -\frac{1}{x}\frac{\partial \psi}{\partial z}, \quad v_z = \frac{1}{x}\frac{\partial \psi}{\partial x}.$$

In the cylindrical coordinates, the equation of the stream function has the form

$$\left(\frac{\partial^2}{\partial x^2} + \frac{\partial^2}{\partial z^2} - \frac{1}{x}\frac{\partial}{\partial x}\right)^2 \psi = 0. \tag{4}$$

In the limiting case of a small distance from the contact line ($r \to 0$), the calculation can be performed on the basis of the local representation of the boundary shapes. We assume that the boundary surfaces are smooth everywhere including the contact line. In this

case, the coordinates of their points can be represented using several terms of the expansion into the Taylor series.

We denote as $\alpha$ the contact angle formed by intersection of the boundary surfaces. With allowance for the axial symmetry, we need to consider the angle $\gamma$ formed by the $x_1$ axis and the radial $x$ axis (see figure). We take $\gamma > 0$ if the outer normal to the surface of the solid is directed toward the symmetry axis, and $\gamma < 0$ if this normal is directed outward of the symmetry axis.

The values of angles $\gamma$ within the range $[-\pi, \pi]$ correspond to various axisymmetric problems. For example, the value $\gamma = \dfrac{\pi}{2}$ can correspond to the fluid flow within a circular pipe. The values $\gamma = 0$ and $\gamma = -\dfrac{\pi}{2}$ correspond to the round droplet on a plane wall and flow outside a round rod, respectively. The value $\gamma = \mp\pi$ corresponds to the case of a gas bubble contacting with a solid wall.

We now introduce the polar coordinates $r$ and $\theta$ with the origin at a point in the contact line, the line $\theta = 0$ coinciding with the negative direction of the $x_1$ axis.

We set the shape of the contours of the surfaces $S$ and $S_{\text{sol}}$ in the small vicinity of the contact line. The equation of the contour $S_{\text{sol}}$ in the case of small distances $r$ has the form

$$\theta = \frac{1}{2}k_S r + O(r^2), \tag{5}$$

where $k_S$ is the curvature of the contour of the surface $S_{\text{sol}}$ on the contact line.

The contour of the free surface $S$ for small distances $r$ is close to the tangent line $\theta = \alpha$:

$$\theta - \alpha = \frac{1}{2}k_F r + O(r^2), \tag{6}$$

where $k_F$ is the curvature of the contour $S$ at the point of the contact line (at $r = 0$).

Thus, the problem of asymptotically calculating the axisymmetric flow involves five geometric parameters, namely, the angles $\alpha$ and $\gamma$, radius $x_0$ of the contact line or its curvature $k_0 = x_0^{-1}$, and the contour curvatures $k_S$ and $k_F$. If we put curvature $k_0$ of the contact line to be zero, we arrive at the particular case of the plane problem. This case is characterized by only three geometric parameters.

The stream function must vanish in the contact line: $\psi \to 0$ as $r \to 0$.

## ASYMPTOTIC BEHAVIOR
## OF A STREAM FUNCTION

In the limit of small distances $r$, the problem is similar to that of flow within a corner when the boundaries are plane and the contact line is straight. Therefore, as $r \to 0$, the stream function $\psi$ can be described by the expansion:

$$\psi = \psi_0 + \psi_1 + \dots. \qquad (7)$$

Here, the main term $\psi_0$ corresponds to flow within a corner, whereas the second term $\psi_1$ is a small perturbation caused by bending boundary surfaces.

The terms in expansion (7) are determined from the solution to Eq. (4) with boundary conditions (1)–(3) in the following form:

$$\psi_0 = r x_0 f_0(\theta), \quad \psi_1 = r^2 f_1(\theta), \qquad (8)$$

$$f_0 = v_0 Q[\sin\theta\cos\alpha - \theta\cos(\theta - \alpha)], \qquad (9)$$

$$f_1(\theta) = \frac{1}{4} v_0 Q \{ -\cos\alpha\sin(2\theta - \gamma) - \cos\alpha\sin\gamma$$
$$+ \cos(2\theta - \alpha - \gamma) + \theta\cos(\alpha - \gamma) \}$$

$$+ x_0 \cdot \frac{1}{4} v_0 k_F Q [1 - \cos 2\theta - \cot\alpha(2\theta - \sin 2\theta)] \quad (10)$$

$$+ x_0 \theta k_S v_0 Q \sin\alpha + x_0 \frac{2\alpha k_S v_0 Q \sin\alpha + \omega}{2(2\alpha - \tan 2\alpha)} \{ -2\theta$$
$$+ \tan 2\alpha(1 - \cos 2\theta) + \sin 2\theta \},$$

where $Q = \dfrac{\sin\alpha}{\alpha - \sin\alpha\cos\alpha}$.

The rotation angular velocity of the tangent to $S$, which enters into expression (10), is linked with the variation rate of the contact angle $\alpha$ and the curvature of the solid's surface by the relationship

$$\dot{\alpha} = \omega + k_S v_0 \qquad (11)$$

(the dot corresponds to differentiating with respect to time).

In the limiting case $r \to 0$, the form of the stream function also depends on the behavior of the solutions $\tilde{\psi}$ to the uniform problem, or, to be more precise, of the solutions to the biharmonic equation $\nabla^4\psi = 0$ within an angle under the uniform conditions on the angle sides. These conditions correspond to immobile plane boundaries, $\tilde{\psi}$ tending to zero in this limiting case. Besides $\psi_0$ and $\psi_1$, asymptotic form (7) can involve an additional term $\tilde{\psi}$. As $r \to 0$ and if $\tilde{\psi} = o(r^2)$, then $\tilde{\psi}$ does not affect the form of the asymptotic behavior and can contribute only to the residual term in expansion (7). If

$\tilde{\psi}$ decreases slower than $r^2$ then it can contribute to the asymptotic solution, which is more noticeable than the function $\psi_1$ defined by relationships (8), (10). Analysis of the uniform problem shows that its arbitrary solution $\tilde{\psi}$ decreases more rapidly than $r^2$ as $r \to 0$, provided that the angle $\alpha$ is smaller than the critical angle $\alpha_* = 128.7°$. For $\alpha > \alpha_*$, there exists the solution $\tilde{\psi}$ that decreases slower than $r^2$.

Hence, it follows that solution (7)–(10) is the general asymptotic form of the stream function in the problem under consideration if the contact angle $\alpha$ is smaller than the critical angle $\alpha_*$.

## ASYMPTOTIC BEHAVIOR
## OF THE NORMAL STRESS ON $S$

There is a correspondence between expansion (7) and the expansion of the normal stress on the free surface

$$P_n = P_{n0} + P_{n1} + \dots.$$

With allowance for (8)–(10), the normal stress as $r \to 0$ is determined by the formula

$$\frac{1}{\mu} P_n \big|_S = \frac{2\sin\alpha}{\alpha - \sin\alpha\cos\alpha} \frac{v_0}{r}$$

$$+ \left\{ v_0 \frac{2k_F\cos\alpha - 2k_S - k_0\sin\alpha\cos(\alpha - \gamma)}{\alpha - \sin\alpha\cos\alpha} \right. \qquad (12)$$

$$\left. + \frac{4\dot{\alpha}}{2\alpha - \tan 2\alpha} \right\} \ln r + O(1).$$

Here, $\mu$ is the dynamic viscosity, $v_0$ is the contact-line velocity, $\alpha$ is the contact angle, $\gamma$ is the angle dependent on the axial symmetry, and $k_0$, $k_F$, and $k_S$ are curvatures of the contact line, the contour of the free surface, and of the contour of the solid's surface, respectively. The contact angle can acquire values within the range $(0, \alpha_*)$, where $\alpha_* = 128.7°$.

The first term in expression (12) corresponds to the Moffatt solution [2] for the particular case of flow within a corner. This term is not limited as $r \to 0$. However, as is seen from formula (12), this first term $P_{n0}$ is insufficient for describing features of stresses. As $r \to 0$, in the general case, for the difference $P_n - P_{n0}$, the limit is absent. The second term of the asymptotic expansion also is not bounded in the limiting case of small distances from the contact line by virtue of the logarithm of the distance, which enters into formula (12). Thus, the axial symmetry and bending contours of boundary surfaces result in the appearance of an unbounded term in the expansion of the normal stress.

Formula (12) represents the general asymptotic expansion for the normal stress on the free surface. This formula is valid for an arbitrary axisymmetric fluid flow with intersecting boundaries, which is described by the Stokes equations.

## ACKNOWLEDGMENTS

## REFERENCES

1. G. I. Taylor, in *Aeronautics and Astronautics* (Pergamon, London, 1960), pp. 21–28.

2. H. K. Moffatt, J. Fluid Mech. **18**, 1 (1964).

3. O. V. Voinov, Izv. Akad. Nauk SSSR, Mekh. Zhidk. Gaza, No. 5, 76 (1976) [Fluid Dyn. **11**, 714 (1976)].

4. O. V. Voinov, Prikl. Mekh. Tekh. Fiz., No. 2, 92 (1977).

5. O. V. Voinov, Dokl. Akad. Nauk SSSR **243**, 1422 (1978) [Sov. Phys. Dokl. **23**, 891 (1978)].

6. P. J. De Gennes, Rev. Mod. Phys. **57**, 827 (1985); Usp. Fiz. Nauk **151**, 619 (1987).

7. O. V. Voinov, in *Encyclopedia of Surface and Colloid Science* (Marcel Dekker, London, 2002), pp. 1546–1558.

*Translated by G. Merzon*

═══════════ **MECHANICS** ═══════════

# Spatial Stationary Dynamic Problem of Elasticity Theory for a Plate with a Through Hole

## Corresponding Member of the RAS É. I. Grigolyuk[1], L. A. Fil'shtinskiĭ[2],*, and Yu. D. Kovalev[2]

The methods of superposition [1] and homogeneous solutions [2, 3] are effectively used in the spatial dynamics of plates. Vorovich and Babeshko [4] considered dynamic mixed problems of elasticity theory for a plate under mixed conditions on the parts of similar sides. Features of the spectrum of natural vibrations for a transversally isotropic disk near the edge resonance were investigated in [5]. In the case of mixed conditions set on the layer surfaces (sliding fit of the ends, or the plate ends are covered by a membrane that is rigid in its plane and flexible in the perpendicular direction), the boundary value problem is much easier than the mixed problems considered in [4].

In elasticity theory, a procedure for solving mixed problems of the stationary vibrations of a plate with tunnel inhomogeneities was proposed in [6]. In that study, the representations of mechanical quantities were found for the symmetric case. In this study, the method of [6] is extended to the skew-symmetric case.

## FORMULATION OF THE PROBLEM AND THE METHOD OF ITS SOLUTION

We consider an elastic plate, $-h \leq x_3 \leq h$ and $-\infty < x_1, x_2 < \infty$, weakened by through tunnel holes directed along the $Ox_3$ axis. The cross sections of the holes are nonintersecting rather smooth contours $L_j$ ($j = 1, 2, \ldots, k$). Forces at the hole boundaries are absent, and a bending pulsating load is applied at infinity:

$$\sigma_{11}^{\infty} = \mathrm{Re}(\langle\sigma_{11}^{\infty}\rangle e^{-i\omega t}), \quad \langle\sigma_{11}^{\infty}\rangle = Px_3,$$

$$P = \mathrm{const.}$$

_____

[1] *Moscow State Technical University "MAMI,"*
  *Bol'shaya Semenovskaya ul. 38, Moscow,*
  *105839 Russia*
[2] *Sumy State University, Sumy, Ukraine*
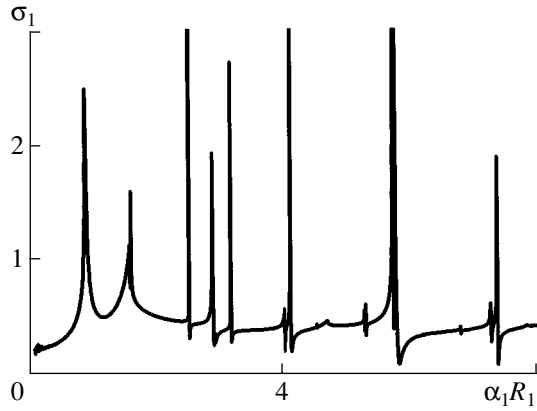* *e-mail: leonid@mphis.sumdu.edu.ua*

We assume that the mechanical parameters have the form

$$u_i = \mathrm{Re}(U_i e^{-i\omega t}), \quad \sigma_{ij} = \mathrm{Re}(\langle\sigma_{ij}\rangle e^{-i\omega t}). \quad (1)$$

We suppose that the amplitudes of the components of the applied load are expanded into Fourier series in the $Ox_3$ coordinate in the closed interval $[-h, h]$. On the surfaces of the plate, the conditions

$$u_3(x_1, x_2, \pm h, t) = \sigma_{13}(x_1, x_2, \pm h, t)$$
$$= \sigma_{23}(x_1, x_2, \pm h, t) = 0 \quad (2)$$

are valid.

Let us write the amplitude components of the displacement vector in the form

$$U_i = \sum_{k=0}^{\infty} u_{ik}(x_1, x_2)\sin\gamma_k x_3, \quad i = 1, 2,$$

$$U_3 = \sum_{k=0}^{\infty} u_{3k}(x_1, x_2)\cos\gamma_k x_3, \quad \gamma_k = (2k+1)\frac{\pi}{2}. \quad (3)$$

Expressions (3) automatically satisfy boundary conditions (2) on the plate surfaces. To describe the stationary wave process in an isotropic cylinder, we use the equations of motion

$$\sigma\,\mathrm{grad}\,\theta + \Delta\mathbf{u} = \frac{\rho}{\lambda+\mu}\frac{\partial^2\mathbf{u}}{\partial t^2},$$

$$\theta = \frac{\partial u_1}{\partial x_1} + \frac{\partial u_2}{\partial x_2} + \frac{\partial u_3}{\partial x_3}, \quad \sigma = \frac{\lambda+\mu}{\mu} = \frac{1}{1-2\nu}, \quad (4)$$

where $\lambda$ and $\mu$ are the Lamé coefficients.

Substituting Eqs. (1) and expansions (3) for the displacement amplitudes into the equations of motion, we

**Fig. 1.**

arrive at the system

$$\kappa_k^{(2)} u_{ik} + \sigma\partial_i\theta_k = 0, \quad i = 1, 2;$$

$$\kappa_k^{(2)} u_{3k} + \sigma\gamma_k\theta_k = 0;$$

$$\kappa_k^{(2)} = \nabla^2 - \beta_k^2, \quad \beta_k^2 = \gamma_k^2 - \alpha_2^2, \quad \alpha_2 = \frac{\omega}{c_2}; \qquad (5)$$

$$\nabla^2 = \partial_1^2 + \partial_2^2,$$

$$\theta_k = \partial_1 u_{1k} + \partial_2 u_{2k} - \gamma_k u_{3k}, \quad \partial_i = \frac{\partial}{\partial x_i}.$$

From Eqs. (5), we immediately find

$$\kappa_k^{(1)}\theta_k = 0, \quad \kappa_k^{(1)} = \nabla^2 - (\gamma_k^2 - \alpha_1^2), \quad \alpha_1 = \frac{\omega}{c_1}. \quad (6)$$

We introduce the function $\psi_k$ through the relation $\theta_k = \kappa_k^{(2)}\psi_k$. From (6), it follows that $\kappa_k^{(2)}\kappa_k^{(1)}\psi_k = 0$. Taking into account the relation between $\theta_k$ and $\psi_k$ and integrating system (5), we obtain

$$u_{ik} = -\sigma\partial_1\psi_k + \omega_{ik}, \quad u_{3k} = -\sigma\gamma_k\psi_k + \omega_{3k},$$
$$\kappa_k^{(2)}\omega_{ik} = 0, \quad i = 1, 2. \qquad (7)$$

If the relation $\theta_k = \kappa_k^{(2)}\psi_k$ is valid, we arrive at the expressions

$$\omega_{1k} = \sigma\partial_2\Omega_k, \quad \omega_{2k} = -\sigma\partial_1\Omega_k,$$
$$\omega_{3k} = -\frac{1}{\gamma_k}(1 + \sigma)\kappa_k^{(1)}\psi_k, \qquad (8)$$

where $\Omega_k$ is an arbitrary solution to the equation $\kappa_k^{(2)}\Omega_k = 0$.

Finally, in view of Eqs. (7) and (8), we obtain

$$u_{1k} - iu_{2k} = 2\sigma\frac{\partial}{\partial z}(i\Omega_k - \Omega_k^{(1)} - \Omega_k^{(2)}),$$

$$\theta_k = (\alpha_2^2 - \alpha_1^2)\Omega_k^{(1)}, \qquad (9)$$

$$u_{3k} = -\sigma\gamma_k\Omega_k^{(1)} - \sigma\left[\gamma_k + \frac{1+\sigma}{\sigma\gamma_k}(\alpha_1^2 - \alpha_2^2)\right]\Omega_k^{(2)}.$$

Here, $\Omega_k^{(i)}$ is an arbitrary solution to the equation $\kappa_k^{(i)}\varphi = 0$, the functions $\Omega_k$ define the rotation of the element about the $Ox_3$ axis, and $u_{ik}$ are the amplitudes of the corresponding parameters.

We take the integral representations of the functions entering into Eqs. (9) in the form

$$\Omega_k^{(1)} = \int_L p_k^{(1)} K_0(\lambda_k r)ds, \quad \Omega_k^{(2)} = \int_L p_k^{(2)} K_0(\beta_k r)ds,$$

$$\Omega_k = \int_L p_k^{(3)} K_0(\beta_k r)ds, \quad r = |\zeta - z|, \qquad (10)$$

$$\zeta = \xi_1 + i\xi_2 \in L = \cup L_j, \quad z = x_1 + ix_2,$$

where $K_0(\gamma r)$ is the zero-order modified Bessel function of the second kind; $ds$ is an arc element of the contour; and the densities $p_k^{(1)}(\zeta)$, $p_k^{(2)}(\zeta)$, and $p_k^{(3)}(\zeta)$ are yet unknown.

The integral representations of functions (10) are arbitrary enough to satisfy the boundary conditions on the hole contours. In addition, they meet the radiation conditions at infinity.

By using Hooke's law and Eqs. (9), the boundary conditions on the contour $L$ are written in the form

$$\frac{1}{\mu}(N_k - iT_k) = -[\Lambda(1 - \sigma) + \sigma\lambda_k^2]\Omega_k^{(1)} - \sigma\beta_k^2\Omega_k^{(2)}$$

$$+ 4\sigma e^{2i\psi}\partial_{zz}^2(i\Omega_k - \Omega_k^{(1)} - \Omega_k^{(2)}), \quad \frac{1}{\mu}(N_k + iT_k)$$

$$= -[\Lambda(1 - \sigma) + \sigma\lambda_k^2]\Omega_k^{(1)} - \sigma\beta_k^2\Omega_k^{(2)} + 4\sigma e^{-2i\psi}\partial_{zz}^2$$

$$\times(-i\Omega_k - \Omega_k^{(1)} - \Omega_k^{(2)}), \quad \frac{1}{\mu}Z_k = e^{i\psi}\partial_z(a_k^*\Omega_k^{(1)}$$

$$+ b_k^*\Omega_k^{(2)} + ic_k^*\Omega_k) + e^{-i\psi}\partial_z(a_k^*\Omega_k^{(2)} + b_k^*\Omega_k^{(2)}$$

$$- ic_k^*\Omega_k), \quad \Lambda = \alpha_2^2 - \alpha_1^2, \quad a_k^* = a_k - \sigma\gamma_k, \quad (11)$$

$$b_k^* = b_k - \sigma\gamma_k, \quad c_k^* = \sigma\gamma_k, \quad a_k = -\sigma\gamma_k,$$

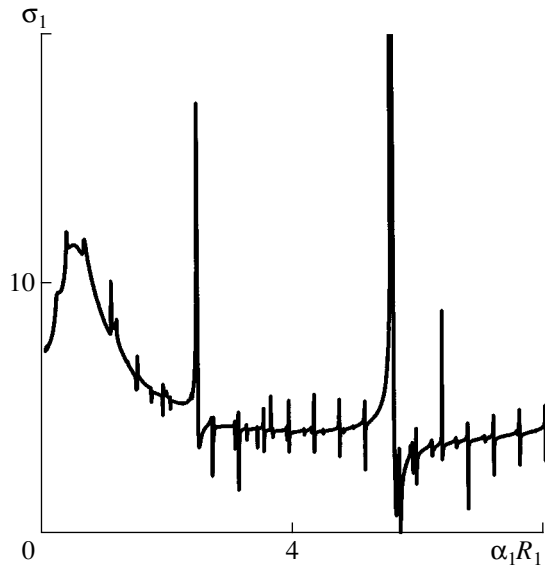$$b_k = -\sigma\left[\gamma_k + \frac{1+\sigma}{\sigma\gamma_k}(\alpha_1^2 - \alpha_2^2)\right],$$
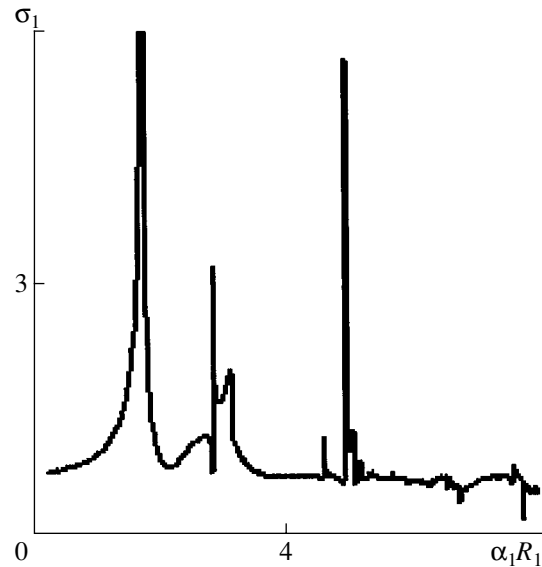
**Fig. 2.**



**Fig. 3.**

where $\psi$ is the angle between the outer normal to the contour $L$ and the $Ox_1$ axis.

Boundary value problem (11) with allowance for representations (10) is reduced by the conventional procedure to a system consisting of three singular integro-differential equations (for each fixed $k$ value). Here, this awkward system is omitted.

### CALCULATIONS AND ANALYSIS OF THE RESULTS

We consider a plate weakened by an elliptical hole:

$$\xi_1 = R_1\cos\varphi, \quad \xi_2 = R_2\sin\varphi, \quad 0 \le \varphi \le 2\pi.$$

To characterize the stress state on the hole surface, we calculate the amplitude values of the quantity

$$\sigma_{\theta\theta} = \sigma_{11}\sin^2\theta + \sigma_{22}\cos^2\theta - 2\sigma_{12}\cos\theta\sin\theta \quad (12)$$

at the contour point $\varphi = \dfrac{\pi}{2}$ and $x_3 = h$.

In a numerical algorithm, the system of integral equations is reduced by the method of mechanical quadratures [7] to a linear system of algebraic equations.

The computational procedure is the following. First, we numerically solve the system of integral equations and find the Fourier coefficients $\sigma_{ij}^{(k)}$ of the stress tensor and the stresses themselves. Next, using formula (12), we calculate the unknown quantities on the hole surface.

Let a bending pulsating load with amplitude $\langle\sigma_{11}^{\infty}\rangle = Px_3$ ($P = \text{const}$) be applied at infinity and forces on the hole surface be absent.

Figures 1 and 2 show the relative amplitude of circumferential stress $\sigma_1 = \left|\dfrac{\langle\sigma_{\theta\theta}\rangle}{P}\right|$ as a function of the dimensionless wave number $\alpha_1 R_1$ for the circular hole
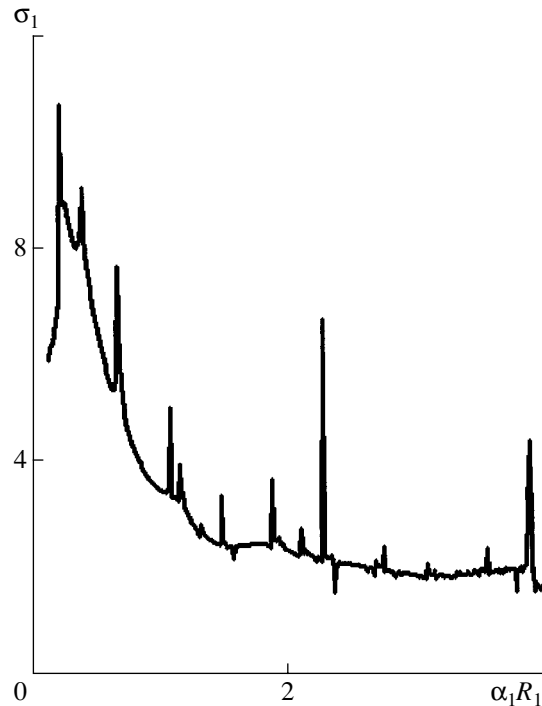


**Fig. 4.**

$(R_1 = R_2 = 1)$ at $\dfrac{h}{R_1} = 4$. For the elliptical hole $(R_1 = 1$

and $R_2 = 1.5)$ at $\dfrac{h}{R_1} = 1$ and $\dfrac{h}{R_2} = 4$, similar dependences are shown in Figs. 3 and 4, respectively.

The numerical results were obtained with Poisson's ratio $\nu = 0.28$.

Thus, the analytical and numerical procedures constructed above provide the possibility of effectively investigating dynamic stress in thick plates with holes under bending vibrations, as well as studying the spectra of natural frequencies under different excitations.

## REFERENCES

1. V. T. Grinchenko and V. V. Meleshko, *Harmonic Oscillations and Waves in Elastic Solids* (Naukova Dumka, Kiev, 1981).

2. O. K. Aksentyan and T. N. Selezneva, Prikl. Mat. Mekh. **40** (1), 112 (1976).

3. A. S. Kosmodamianskiĭ and V. A. Shaldyrvan, *Thick Multilayer Plates* (Naukova Dumka, Kiev, 1978).

4. I. I. Vorovich and V. A. Babeshko, *Dynamic Mixed Problems of Elasticity Theory for Nonclassical Domains* (Nauka, Moscow, 1979).

5. V. I. Storozhev, Yu. V. Mysovskiĭ, and O. D. Sokolova, Teor. Prikl. Mekh. **37**, 184 (2003).

6. L. A. Fil'shtinskiĭ, Teor. Prikl. Mekh. **21**, 13 (1990).

7. S. M. Belotserkovskiĭ and I. K. Lifanov, *Numerical Methods of Solving Singular Integral Equations* (Nauka, Moscow, 1985).

*Translated by Yu. Vishnyakov*